

University of Nebraska - Lincoln

DigitalCommons@University of Nebraska - Lincoln

---

Civil Engineering Theses, Dissertations, and  
Student Research

Civil Engineering

---


Summer 8-15-2014

# Turbulent Circular Culvert Flow: Implications to Fish Passage Design

Amin Mohebbi

*University of Nebraska-Lincoln*, [amohebbi@unomaha.edu](mailto:amohebbi@unomaha.edu)

Follow this and additional works at: <http://digitalcommons.unl.edu/civilengdiss>

 Part of the [Civil Engineering Commons](#), [Environmental Engineering Commons](#), and the [Hydraulic Engineering Commons](#)

---

Mohebbi, Amin, "Turbulent Circular Culvert Flow: Implications to Fish Passage Design" (2014). *Civil Engineering Theses, Dissertations, and Student Research*. 72.

<http://digitalcommons.unl.edu/civilengdiss/72>

This Article is brought to you for free and open access by the Civil Engineering at DigitalCommons@University of Nebraska - Lincoln. It has been accepted for inclusion in Civil Engineering Theses, Dissertations, and Student Research by an authorized administrator of DigitalCommons@University of Nebraska - Lincoln.

TURBULENT CIRCULAR CULVERT FLOW: IMPLICATIONS TO FISH PASSAGE DESIGN

by

Amin Mohebbi

A DISSERTATION

Presented to the Faculty of

The Graduate College at the University of Nebraska

In Partial Fulfillment of Requirements

For the Degree of Doctor of Philosophy

Major: Civil Engineering

Under the Supervision of Professor Junke Guo

Lincoln, Nebraska

August, 2014

# TURBULENT CIRCULAR CULVERT FLOW: IMPLICATIONS TO FISH PASSAGE DESIGN

Amin Mohebbi, Ph.D.

University of Nebraska, 2014

Advisor: Junke Guo

Culverts are popular conveyance structures in America and Canada to be used as a fish passage or in sewage collection and disposal systems. Fish passage design criteria is based on biological capabilities of fish whereas it should satisfy hydraulic and hydrological constraints as well. Failing to provide enough low velocity regions for aquatic organisms may result in their mass extinctions. Currently, proper road crossing design depends on either model studies or numerical simulations via Computational Fluid Dynamic (CFD) packages, both of which are expensive and time consuming. Further, although the design procedures released by FHWA recently ensures safe fish migration from downstream toward upstream, it results in an unnecessarily large cross-sections increasing the overall project cost. In addition, the extensively used Manning model is not capable of providing local velocities or modeling the maximum velocity position (dip phenomenon).

This study describes an attempt to solve Reynolds-Averaged Navier-Stokes Equations (RANS) for a steady state and uniform circular open channel flow at mild slopes, resulting in an analytical solution for a partially-filled pipe velocity distribution. Moreover, an empirical model based on the modified log-wake (MLW) law from previous knowledge of rectangular open channel flow was developed to further shed light on the topic. Both models were verified with experimental data

collected with Stereoscopic Particle Image Velocimetry (S-PIV) through the work of the writer in the Turner-Fairbank Highway Research Center of the Federal Highway Administration and various other benchmark data from the literature. These models can be used as a novel and powerful design tool resulting in an optimum cross-section along with an enough low velocity region to facilitate safe fish passage.

To  
my late grandfather, Yousef Mohebbi  
a great teacher and mentor

## ACKNOWLEDGEMENT

I would like to express my sincere thanks and gratitude to my committee chair Prof. Junke Guo for his advice, precious time and constant support throughout my career at University of Nebraska, Lincoln. Moreover, I truly appreciate the valuable input and comments made by my committee members Prof. John S. Stansbury, Prof. Tian Zhang and Prof. Terri R. Norton without which my efforts would not have been complete and fruitful. My deep appreciation to Mrs. Arlys Blackey, admin tech of department of civil engineering at University of Nebraska, Omaha for her kind and supporting behavior toward me during my stay at Nebraska.

I would like to acknowledge Prof. Jaeyong Sung of Seoul National University of Science and Technology and Prof. Shawn P. Clark of University of Manitoba for providing their valuable experimental velocity distribution data for the theoretical model verification, without which this research was not possible.

Special thanks go to Dr. Omid Kalantari and Dr. Simin Akbariyeh for their endless feedback during my graduate study. I have benefited a lot from their strong background in hydrology, GIS, water quality modeling and ground water remediation as well as their invaluable discussions.

My gratitude to my supervisors Dr. Kornel Kerenyi and Dr. Jerry Shen and colleagues Dr. Haoyin Shan, Mr. Andreas Wagner, Mr. Michael Uhrig, Mr. Matthias Poehler and Mr. Oscar Suaznabar of Federal Highway Administration (FHWA) for their patient guidance and assistance in building the physical model, assembling Stereoscopic-Particle Image Velocimetry (S-PIV) and Acoustic Doppler Velocimetry (ADV).

Finally, I would like to express the deepest appreciation to my aunt Prof. Shahla Bahavar, my uncle Dr. Ali A. Khatami and my parents for their unconditional love, financial and moral support.

## TABLE OF CONTENTS

COVER PAGE.....	i
ABSTRACT.....	ii
DEDICATION .....	iv
ACKNOWLEDGEMENT .....	v
TABLE OF CONTENTS.....	vii
LIST OF FIGURES.....	xii
LIST OF TABLES.....	xvi
LIST OF SYMBOLS .....	xvii
LIST OF ACRONYMS.....	xxiii
CHAPTER 1: INTRODUCTION.....	1
1.1 Introduction .....	1
1.2 Motivation.....	1
1.2.1 Environmental.....	1
1.2.2 Physics.....	2
1.3 Objectives .....	4
1.4 Outline of Dissertation.....	4
CHAPTER 2: LITERATURE REVIEW .....	6



2.1	Culvert.....	6
2.2	Fish Passage .....	8
2.3	Experimental Quantitative Visualization .....	10
2.3.1	Particle Image Velocimetry (PIV) .....	11
2.3.2	Stereoscopic Particle Image Velocimetry (S-PIV).....	11
2.4	Comments and Knowledge Gaps .....	17
CHAPTER 3: EXPERIMENTAL PROCEDURE .....		18
3.1	Experimental Setup.....	18
3.1.1	Flume .....	18
3.1.2	Stereoscopic Particle Image Velocimetry (S-PIV) Setup .....	19
3.1.3	Acoustic Doppler Velocimetry (ADV) Setup.....	20
3.2	Corrugated Metal Pipe (CMP) Specifications.....	21
3.2.1	CMP Sections .....	21
3.2.2	CMP Preparation.....	22
3.3	Sieve Analysis .....	24
CHAPTER 4: ANALYTICAL SOLUTION TO P-FPF .....		27
4.1	Newton’s Law.....	27
4.2	Reynolds-Averaged Navier-Stokes (RANS) Equations.....	28
4.3	Governing Equations.....	30
4.3.1	Constant Eddy Viscosity Model.....	35

4.3.2	Variable Eddy Viscosity Model .....	36
4.4	Summary .....	37
CHAPTER 5: EMPIRICAL SOLUTION TO P-FPF.....		38
5.1	Boundary Shear Flows.....	38
5.2	Prandtl's Mixing Length Theory (MLT).....	39
5.3	Modified log-wake (MLW) law for a turbulent F-FPF .....	41
5.4	Governing Equations.....	43
5.4.1	Centerline Velocity Distribution.....	43
5.4.2	Cross-Sectional Velocity Distribution Model .....	44
CHAPTER 6: MODEL VERIFICATION AND DISCUSSION.....		47
6.1	Analytical Solution of P-FPF .....	47
6.1.1	General Remarks.....	47
6.1.2	Cross-sectional Velocity Distribution .....	49
6.2	Empirical Solution of P-FPF .....	51
6.2.1	General Remarks.....	51
6.2.2	Velocity Dip Model.....	52
6.2.3	Centerline Velocity Distribution.....	54
6.2.4	Cross-sectional Velocity Distribution .....	54
6.2.5	Roughness Effect.....	60
CHAPTER 7: APPLICATONS OF P-FPF IN DESIGN .....		62

7.1	Sewer Design.....	62
7.2	Fish Passage Design .....	63
7.2.1	Simplified Method .....	63
7.2.2	Comprehensive Method .....	69
CHAPTER 8: CONCLUSIONS.....		71
8.1	Summary and Conclusions.....	71
8.2	Future Work.....	72
REFERENCES.....		74
APPENDIX A: DATA .....		84
A.1	Mohebbi et al. (2010) Data .....	84
A.1.1	Experimental Method .....	84
A.1.2	Velocity Contour Plots .....	89
A.2	Clark and Kehler (2011) Data .....	89
A.2.1	Experimental Method .....	89
A.2.2	Velocity Contour Plots .....	91
A.3	Yoon et al. (2012) Data .....	91
A.3.1	Experimental Method .....	91
A.4	Knight and Sterling (2000) Data.....	93
A.4.1	Experimental Method .....	93
A.4.1	Velocity Contour Plots .....	93

APPENDIX B: S-PIV IMAGES ..... 96

B.1 Camera Calibration Images..... 96

## LIST OF FIGURES

Figure 1.1 Laminar and Turbulent Flow (Pipingdesign, 2014) .....	3
Figure 2.1 S-PIV Translational Configuration .....	13
Figure 2.2 S-PIV Angular Configuration.....	13
Figure 3.1 Tilting Flume with the Culvert inside	
a) Modeled in Solid Works b) Real-World Picture .....	18
Figure 3.2 S-PIV Setup a) Front View b) Side View .....	19
Figure 3.3 ADV Setup a) Front View b) Side View.....	20
Figure 3.4 Annular CMP Shape (CONTECH Engineered Solutions , 2014) .....	22
Figure 3.5 CMP a) Lateral Cross-section View b) Isometric View .....	22
Figure 3.6 Bed Elevation at 0% Culvert Diameter and Symmetrical half of the Model.....	23
Figure 3.7 Bed Elevation at 15% Culvert Diameter and Symmetrical Half of the Model .....	23
Figure 3.8 Bed Elevation at 30% Culvert Diameter and Symmetrical Half of the Model .....	23
Figure 3.9 Prepared CMP Section a) Coated with Epoxy b) Placed Inside Flume.....	24
Figure 3.10 Gravel Properties Used in Roughness Test	
a) Soil Histogram b) Soil Frequency c) Soil Frequency Cumulative d) Soil Cumulative Probability.....	25

Figure 3.11 Logarithmic Cumulative Probability.....	25
Figure 4.1 Circular Open Channel Flow Longitudinal View.....	31
Figure 4.2 Circular Open Channel Flow Cross-Sectional View.....	31
Figure 5.1 Empirical Centerline Velocity Profile in F-FPF.....	39
Figure 5.2 Circular Open Channel Flow Cross-sectional View in Vector Notation.....	42
Figure 5.3 Comparison of F-FPF with P-FPF.....	43
Figure 6.1 Cross-sectional Velocity Distribution Generated with Eq. 56 a) $h/D=20\%$ b) $h/D=30\%$ c) $h/D=40\%$ d) $h/D=50\%$ .....	48
Figure 6.2 Experimental (left half of cross-section) and Predicted Analytical (right half of cross-section) Cross-sectional Velocity Distribution a) Yoon et al. (2012) Test 1 b) Test 2 c) Test 3 d) Clark and Kehler (2011) Test 4 e) Test 2 f) Test 5.....	50
Figure 6.3 Velocity Dip Position Model for Smooth and Rough Pipes.....	53
Figure 6.4 Comparison of Eq. 70 with Yoon et al. (2012) Centerline Velocity Profile a) Logarithmic b) Ordinate.....	55
Figure 6.5 Comparison of Eq. 70 with Clark and Kehler (2011) Centerline Velocity Profile a) Logarithmic b) Ordinate.....	56

Figure 6.6 Experimental (left half of cross-section) and Predicted Empirical (right half of cross-section) Cross-sectional Velocity Isovels	
a) Yoon et al. (2012) Test 1 b) Test 2 c) Test 3 d) Test 4 e) Test 5 f) Test 6 .....	58
Figure 6.7 Experimental (left half of cross-section) and Predicted Empirical (right half of cross-section) Cross-sectional Velocity Isovels	
a) Clark and Kehler (2011) Test 1 b) Test 2 c) Test 3 d) Test 4 e) Test 5 .....	59
Figure 6.8 Circular Open Channel Flow Cross-sectional View with Roughness.....	60
Figure 6.9 Experimental (left half of cross-section) and Predicted Empirical (right half of cross-section) Cross-sectional Velocity Isovels	
Knight and Sterling (2000) a) Test 1 b) Test 2.....	61
Figure 7.1 P-FPF Hydraulic Elements .....	64
Figure 7.2 Fish Passage	
a) Near Crooked Lake (photo courtesy of NRCS) b) Migrating Salmon through culvert on Meadow Creek in Matanuska-Susitna Valley (photo courtesy of U.S. Fish and Wildlife Service).....	65
Figure 7.3 Depth-Averaged Velocity for Different Flow Depths.....	67
Figure 7.4 Design Curve for Fish Passage with Different Fish Design Velocity .....	67
Figure 7.5 Fish Sizing (courtesy of Australian Government Department of the Environmental) ..	68
Figure A.1 Cross-sectional Velocity Distribution (Mohebbi, Zhai, & Kerényi, 2010)	
a) Test 1_1 b) Test 1_4 c) Test 1_2 d) Test 1_5 e) Test 1_3 f) Test 1_6.....	86

Figure A.2 Cross-sectional Velocity Distribution (Mohebbi, Zhai, & Kerenyi, 2010)

a) Test 2\_1 b) Test 2\_4 c) Test 2\_2 d) Test 2\_5 e) Test 2\_3 f) Test 2\_6..... 87

Figure A.3 Cross-sectional Velocity Distribution (Mohebbi, Zhai, & Kerenyi, 2010)

a) Test 3\_1 b) Test 3\_4 c) Test 3\_2 d) Test 3\_5 e) Test 3\_3 f) Test 3\_6..... 88

Figure A.4 Cross-sectional Velocity Distribution (Clark & Kehler, 2011)

a) Test 1 b) Test 2 c) Test 3 d) Test 4 e) Test 5..... 90

Figure A.5 Cross-sectional Velocity Distribution (Yoon, Sung, & Lee, 2012)

a) Test 1 b) Test 2 c) Test 3 d) Test 4 e) Test 5 f) Test 6..... 92

Figure A.6 Cross-sectional Velocity Distribution (Knight & Sterling, 2000; Sterling & Knight, 2000)

a) Test 1\_2 b) Test 2\_3 c) Test 2\_4 ..... 95

Figure B.7 Camera Calibration Images

Camera Calibration Left View Image a) Normal b) Masked c) Processed d) Dewarped

Camera Calibration Right View Image e) Normal f) Masked g) Processed h) Dewarped . 97



## LIST OF TABLES

Table 3.1 Handling Weights for CMP Used in the Experiment (3"x1").....	21
Table 3.2 Grain Size for the Proposed Soil.....	26
Table 3.3 Physical Characteristics of the Proposed Soil.....	26
Table 6.1 Fitted and Calculated Shear Velocity Comparison .....	51
Table 6.2 Measure of the Goodness of Empirical Centerline Velocity Model (Eq. 70).....	53
Table 6.3 Measured Experimental and Fitted Maximum Velocity Comparison .....	57
Table 7.1 State of Maryland General Design Requirements for Fish Passage (Zhai, 2012).....	64
Table 7.2 State of California General Design Requirements for Fish Passage (Bates, 2002).....	65
Table A.1 Laboratory Test Matrix (Mohebbi, Zhai, & Kerenyi, 2010) .....	85
Table A.2 Laboratory Test Matrix (Clark & Kehler, 2011) .....	89
Table A.3 Laboratory Test Matrix (Yoon, Sung, & Lee, 2012) .....	91
Table A.4 Laboratory Test Matrix (Knight & Sterling, 2000; Sterling & Knight, 2000).....	94

## LIST OF SYMBOLS

### Latin Symbols

$A$	= Constant of integration (-)
$A_w$	= Wetted area (m <sup>2</sup> )
$A_{w50}$	= Wetted area corresponding to 50% filling ratio (m <sup>2</sup> )
$ \overline{AB} $	= Length from point A to B defined according to Figure 5.2 (m)
$b$	= Free surface width (m)
$b/D$	= Width to depth ratio (-)
$C$	= Integration constant (m/s)
$C_0-C_{17}$	= Polynomial coefficients (-)
$ \overline{CB} $	= Length from point C to B defined according to Figure 5.2 (m)
$c/k$	= Cycle pitch to depth ratio (-)
$D$	= Pipe diameter (m)
$D_{50}$	= Grain mass median diameter (mm)
$dx; dy; dz$	= Real-world displacement components (m)
$dx_r; dx_l$	= Projected horizontal displacement of the particles recorded onto the right camera (px)
$dy_r; dy_l$	= Projected vertical displacement of the particles recorded onto the left camera (px)
$F_r$	= Froude number (-)

$f$	= Arbitrary function (m/s)
$\bar{f}$	= Time averaged function (m/s)
$fl$	= Lens focal length (mm)
$g$	= Gravitational acceleration (m/s <sup>2</sup> )
$g_r; g_\theta; g_z$	= Gravitational acceleration in $r, \theta, z$ direction (m/s <sup>2</sup> )
$h$	= Water elevation (m)
$h'$	= Sediment depth (m)
$h/D$	= Filling ratio (-)
$h_d$	= Fish Height (m)
$L_d$	= Fish Length (m)
$l_m$	= Mixing length (m)
$M_o$	= Nominal magnification (-)
$N$	= Number of the pair of template points(-)
$n$	= Fitting parameter to Eq. 87 (-)
$O$	= Cartesian coordinate system origin according to Figure 4.2 (-)
$O'$	= Circle center according to Figure 4.2 (-)
$ \overline{OC} $	= Length from point O to C defined according to Figure 5.2 (m)
$ \overline{OM} $	= Length from point O to M defined according to Figure 5.2 (m)
$P_w$	= Wetted perimeter (m)
$P_{w50}$	= Wetted perimeter corresponding to 50% filling ratio (m)
$P_{rr}; P_{\theta\theta}; P_{zz}$	= Normal stress components in $r, \theta$ and $z$ directions (Pa)

$P_{r\theta}; P_{zr}; P_{\theta z}$	= Shear stress components in $\theta$ , $r$ and $z$ directions acting on a surface that is oriented perpendicular to directions $r$ , $z$ and $\theta$ , respectively (Pa)
$P'_{xy}$	= Turbulent shear stress component in $y$ direction acting on a surface that is oriented perpendicular to direction $x$ (Pa)
$p$	= Pressure (Pa)
$\bar{p}$	= Time averaged pressure (Pa)
$p'$	= Pressure fluctuation (Pa)
$Q$	= Discharge ( $\text{m}^3/\text{s}$ )
$Q; P_x; P_y$	= Polynomial functions of a given order (-)
$R$	= Pipe radius (m)
$R^2$	= Determination correlation (-)
$Re$	= Reynolds number (-)
$R_h$	= Hydraulic radius (m)
$R_{h50}$	= Hydraulic radius corresponding to 50% filling ratio (m)
$r; \theta; z$	= Cylindrical coordinates (m)
$S_0$	= Channel bed slope (m/m)
$t$	= Time (s)
$\bar{U}$	= Cross-sectional average velocity (m/s)
$\bar{U}_{50}$	= Cross-sectional average velocity corresponding to 50% filling ratio (m/s)
$U_d$	= Fish design velocity (m/s)
$U_{max}$	= Maximum Cross-sectional velocity (m/s)

$u; v; w$	= Velocity components in $x, y, z$ directions (m/s)
$\bar{u}_{max}$	= Maximum centerline velocity (m/s)
$u_r; u_\theta; u_z$	= Velocity components in $r, \theta, z$ directions (m/s)
$u'_r; u'_\theta; u'_z$	= Fluctuating velocity components in $r, \theta, z$ directions (m/s)
$\bar{u}_r; \bar{u}_\theta; \bar{u}_z$	= Time averaged velocity components in $r, \theta, z$ directions (m/s)
$u^*$	= Shear velocity (m/s)
$u^+$	= Dimensionless velocity (-)
$u_{fit}^*$	= Shear velocity obtained through non-linear curve-fitting (m/s)
$X; Y; Z$	= Physical coordinates (m)
$x; y; z$	= Cartesian coordinates (m)
$x_B; y_B$	= Point B coordinates according to Figure 5.2 (m)
$x_d$	= Horizontal minimum width for fish passage (m)
$x_C; y_C$	= Point C coordinates according to Figure 5.2 (m)
$x_O; y_O$	= Point O coordinates according to Figure 5.2 (m)
$x_p; y_p; z_p$	= Coordinates of a particle P in the light sheet (m)
$x_r; y_r$	= Horizontal and vertical coordinates of the particle p recorded onto the right camera (px)
$x_l; y_l$	= Horizontal and vertical coordinates of the particle p recorded onto the left camera (px)
$y^+$	= Dimensionless length (-)
$y_0$	= Roughness height (m)

**Greek Symbols**

$\alpha$	= Angle according to Figure 2.1 (-)
$\alpha_r; \alpha_l$	= Angle between the viewing ray and the light sheet normal, from right and left camera, accordingly (xz plane) (-)
$\beta_r; \beta_l$	= Angle between the viewing ray and the light sheet normal, from right and left camera, accordingly (yz plane) (-)
$\Delta B$	= Roughness shift (-)
$\delta$	= Dip position (m)
$\epsilon/D$	= Pipe relative roughness (-)
$\theta$	= Cylindrical coordinates (-)
$\kappa$	= Von Karman coefficient (-)
$\lambda$	= Fitting parameter to Eq. 87 (-)
$\mu$	= Dynamic viscosity (Pa.s)
$\nu$	= Kinematic viscosity (m <sup>2</sup> /s)
$\nu_t$	= Eddy viscosity (m <sup>2</sup> /s)
$\xi$	= Relative depth (-)
$\Pi$	= Coles wake function fitting parameter (-)
$\pi$	= Constant equal to 3.1415 (-)
$\rho$	= Density (kg/m <sup>3</sup> )
T	= Time period (s)
$\phi$	= Optimization function (m <sup>2</sup> )

- $\varphi$  = Angle between the image plane and the lens plane (-)
- $\psi$  = Angle between the lens plane and the object plane (-)
- $\omega$  = Coles wake function (-)

## LIST OF ACRONYMS

3D	= Three Dimensional
ADV	= Acoustic Doppler Velocimetry
BC	= Boundary Condition
CCD	= Charge-coupled Device
CFD	= Computational Fluid Dynamics
CMP	= Corrugated Metal Pipe
F-FPF	= Fully-Filled Pipe Flow
FHWA	= Federal Highway Administration
GIS	= Geographic information system
HDS	= Hydraulic Design Series
HEC	= Hydraulic Engineering Circular
LDV	= Laser Doppler Anemometry
LW	= Log-Wake
MLT	= Mixing Length Theory
MLW	= Modified Log-Wake
NS	= Navier- Stokes
P-FPF	= Partially-Filled Pipe Flow
PIV	= Particle Image Velocimetry



RANS	= Reynolds-Averaged Navier-Stokes
S-PIV	= Stereoscopic Particle Image Velocimetry
TKE	= Turbulent Kinetic Energy

# CHAPTER 1: INTRODUCTION

## 1.1 Introduction

A closed conduit with a span of less than 20 feet that is used as a passage for flood, sewage and/or an aquatic organism from one side of the road to the other side is called a culvert (Schall, Thompson, Zerges, & Kilgore, 2012). Varying in shape, size and material (Gardner, 2006; Norman, Houghtalen, & Johnston, 2001), culverts are commonplace in countries like the United States and Canada. Previously, they were designed based on the condition of the inlet control depending on whether it was submerged or unsubmerged (Tuncok & Mays, 1999; Norman, Houghtalen, & Johnston, 2001). Their most recent design procedure (Kilgore, Bergendahl, & Hotchkiss, 2010; Hotchkiss & Frei, 2007; Schall, Thompson, Zerges, & Kilgore, 2012) results in unnecessarily large sizes to reduce the cross-sectional average velocity, facilitating fish and other aquatic organisms migration from downstream toward upstream. A new robust method is needed satisfying both hydraulic and environmental constraints while optimizing the design cross-section that will eventually reduce the project cost. Further, cross-sectional local velocities should be investigated more thoroughly to make sure they will not exceed fish swimming capabilities.

## 1.2 Motivation

### *1.2.1 Environmental*

Fish passage downstream design criteria are based on biological capabilities of fish whereas the upstream design criteria should satisfy hydraulic and hydrological constraints. Juvenile fish, due to their nature, tend to migrate from downstream toward upstream habitat in spawning seasons.

Restrictions (e.g., high velocity, high turbulence intensity, low water depth, debris, and sediment deposition) to their free movement impair their reproduction and diminish their population. Fish deaths are reported all over the nation because of poor fish passage performance as well as inadequate operation and maintenance. For example, in Washington State, an estimated 2400 to 4000 fish barrier structures existed in the early 20<sup>th</sup> century (Rowland, Hotchkiss, & Barber, 2002). These suggest that although culvert design is well understood and developed for hydraulic and hydrologic criteria, they continue to be fish barriers. The long term effect of such a malfunction can lead to extinction of a specific aquatic organism in the region of interest. A design model or a procedure which accounts for all the effective parameters incorporating biological characteristics of organisms is a necessary addition to the current design manuals.

### *1.2.2 Physics*

Osborne Reynolds, in his 1883 publication, introduced properties of the transition of laminar to turbulent pipe flow condition by defining a dimensionless number later named after him, in recognition (Reynolds, 1883). Careful measurements (Reynolds, 1883) show that flow particles having a Reynolds (Re) number below 2000 move in parallel layers (Figure 1.1) without any momentum and energy exchange between two layers (laminar flow) whereas flow particles having a Re number over 4000 in pipes traverse irregular trajectories (Figure 1.1) making the flow unpredictable (turbulent flow).

Pipe flow is a fundamental topic in physics which dates back to the early stages of fluid mechanics development. Early efforts were to predict a fully-filled pipe flow (F-FPF) ignoring the partially-filled pipe flow (P-FPF) due to the complications imposed by the free surface. Poiseuille (1838)

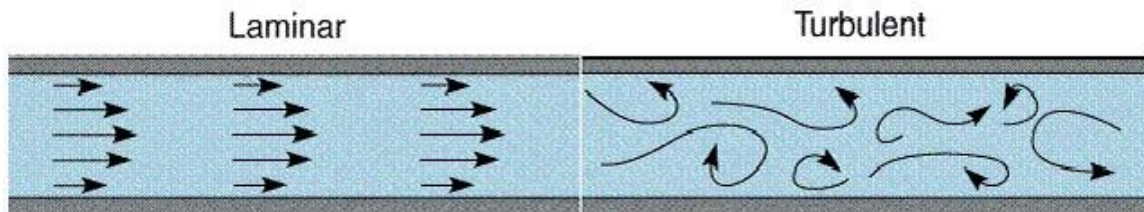


**Figure 1.1 Laminar and Turbulent Flow (Pipingdesign, 2014)**

and Hagen (1839), following experimental approaches, arrived at the same equation for a fully-filled *laminar* pipe flow (Sutera & Skalak, 1993). Their successors spent a great deal of time and energy to develop a model to predict a fully-filled *turbulent* pipe flow. However, due to the unpredictable nature of the turbulence, it was not until recent that a generally accepted model was adopted for a fully-filled *turbulent* pipe flow (Guo & Julien, 2003; Guo, Julien, & Meroney, 2005).

Still there was a huge gap in this field, and that was a model for a P-FPF which is of great importance in storm sewer, fish passage and hydro tunnels design. Recently, some attempts were made to solve the Navier-Stokes equations<sup>1</sup> for a *laminar* P-FPF to shed more light on the culvert flow problem (Guo & Meroney, 2013). Their Fourier Transform based solution can also be considered as an extreme case for the *turbulent* P-FPF. Unfortunately, most of the real-world problems are turbulent leaving the *turbulent* P-FPF flow still an unsolved problem. The non-linearity of the NS equations, existence of a free surface, not having enough information about the eddy viscosity and turbulence imposed complications are the reasons why there are not many scientists investing on the subject.

<sup>1</sup> Governing equations for Newtonian fluids. The reader is referred to Chapter 4 for more information.

### 1.3 Objectives

This dissertation aims at finding a method to design *turbulent* partially-filled circular culverts resulting in fish passage design with adjusted low velocity region according to fish swimming capabilities accounting for both hydraulic and biological constraints ii) An analytical solution of the NS equations together with an empirical model based on the modified log-wake (MLW) law will be tested with cross-sectional velocity distribution data acquired with the state-of-the-art Stereoscopic-Particle Image Velocimetry (S-PIV). The final model can benefit both industry and academia in design of new fish passages and storm sewers as well as reassessment of the existing culverts after severe weather events.

In particular, this dissertation will:

- Utilize the state-of-the-art S-PIV for the first time to acquire the whole flow field velocity distribution in a *turbulent* partially-filled circular culvert. This data can be used as benchmark data for future mathematical and CFD model calibrations.
- Solve the NS equations with simplifying assumptions as well as develop a mathematical model based on the MLW law, resulting accordingly in an analytical solution and an empirical model for partially-filled *turbulent* culvert flow.
- Offer a step-by-step fish passage design procedure.

### 1.4 Outline of Dissertation

In the following contribution, initially, the theoretical background of Stereoscopic Particle Image Velocimetry (S-PIV) is discussed. In addition, the experimental setup and facilities used are presented. Later, two mathematical models one based on the direct solution of the Reynolds-Averaged Navier-Stokes (RANS) equations (analytical solution) and the other one based on the

modified log-wake (MLW) law (empirical solution) are developed. The benchmark data from (Yoon, Sung, & Lee, 2012; Clark & Kehler, 2011; Sterling & Knight, 2000) and also the data acquired by the writer (Mohebbi, Zhai, & Kerényi, 2010) will be used to verify the proposed models. Chapter 7 is completely dedicated to the applications of the introduced models in sewer and fish passage design. Consequently, the conclusions and future scope of this research will be presented. Appendix A and B provide useful information regarding the validation data and the sample images used in the camera calibration process, accordingly.

## CHAPTER 2: LITERATURE REVIEW

In this chapter, early works on partially filled pipe flows are reported and summarized. The investigations in this field can be divided into two groups: i) those that are only related to the culvert and hydraulics; and ii) those that study the culverts in terms of fish passage.

### 2.1 Culvert

The first work in partially-filled pipe flow (P-FPF) is traced back to July 1950 of the St. Antony Falls Hydraulic Laboratory of the University of the Minnesota where friction and pipe loss coefficients for concrete and Corrugated Metal Pipes (CMP) were measured for the first time (Straub & Morris, 1950a; Straub & Morris, 1950b). Replogle and Chow (1966) were among the first pioneers who measured the cross-sectional velocity distribution of a circular culvert. They performed many experiments and provided insight on the circular culvert flow for the first time. Funamizu, Yamashita, and Takakuwa (1991) proposed a new uniform flow formula which had some advantages over the Manning formula by providing a better expression of the flow properties for a circular P-FPF as well as a wider applicable range of pipe roughness. Moreover, they used the Replogle and Chow (1966) experiments to validate their proposed model. Knight and Sterling (2000) measured cross-sectional velocity distribution to account for boundary shear stress in circular pipes running partially full (Knight & Sterling, 2000; Sterling & Knight, 2000). However, they did not provide any model for velocity distribution but rather used their data to calibrate their empirical prismatic channel shear stress equation. The same year, Ead, Rajaratnam, Katopodis, and Ade (2000) measured extensive vertical velocity distribution profiles at the centerline and different streamwise stations along the centerline in circular corrugated pipes,

explaining that the maximum velocity occurs below the free surface (dip phenomenon). Moreover, they devised an empirical equation to predict the position of the dip. They compared their data with the universal log-law and found good agreement in the inner region. Berlamont, Trouw, and Luyckx (2003) and Azevedo, Morales, Franco, Junqueira, and Erthal (2008) modeled the partially filled turbulent pipe flow with the aid of a CFD package, showing that the  $k - \epsilon$  model yields results in agreement with that of the Knight and Sterling (2000). Abbs, Kells, and Katopodis, (2007) measured velocity distributions at several stations along a length of a corrugated steel culvert employing Acoustic Doppler Velocimetry (ADV) and confirmed that approximately one-third of the flow area had a velocity that was less than mean velocity. Magura (2007) also, performed ADV tests on a corrugated structural plate and compared isovels with HEC-RAS simulations (Magura C. R., 2007a; Magura C. R., 2007b). Spiral corrugated pipe velocities were measured by Richmond, Deng, Guensch, Tritico, and Pearson (2007), investigating the centerline velocity profiles and the secondary flow induced by the spiral corrugations. They used ADV for their measurements and investigated the lateral and axial turbulence intensity and its effect in terms of fish migration. Laboratory experiments were conducted on helical and annular corrugated metal pipes to determine the Manning coefficient and its dependency on the flow depth. Tests ranging from 30% to 90% filling ratios (depth to pipe diameter) were conducted, and it was decided that the Manning coefficient for P-FPF is generally higher than that of F-FPF (McEnroe & Malone, 2008). Kehler (2009) performed ADV tests on a CMP to investigate the low velocity regions close to the bed. He confirmed that there is a significant cross-sectional area below average velocity postulating that roughness on the bed (embedment) further increases this area. Also, a technique similar to that of a log-wake law was devised and validated with his experimental data (Kehler, 2009).



Some of the culverts are retrofitted with baffles to dissipate the Turbulent Kinetic Energy (TKE) induced by turbulence. A CMP fitted with sloped and slotted-weir baffles was studied experimentally using ADV. Lateral and vertical velocity distributions and TKE measurements revealed only minor differences in the turbulent heterogeneity between two setups (Morrison, Hotchkiss, Stone, Thurman, & Horner-Devine, 2009).

Recently, Clark and Kehler (2011) and Yoon, Sung, and Lee (2012) shed some more light on the problem. While the former publication provides an empirical equation for the velocity distribution in corrugated culverts at mild slopes, the latter one mostly focuses on the friction coefficient as well as shear stress distribution through fitting Chiu's empirical equation (Chiu, 1989) in a curvilinear coordinate system to the experimental data. Clark and Kehler (2011) extended the law of the wall to the entire cross-section and was left with a singularity in the center.

## 2.2 Fish Passage

Researchers first started to investigate culverts which are being used as fish passage in depth in the 1970s. Most of the fish passage culverts were found to be fish barriers because of either high velocity or turbulence intensity. Many scientists proposed to install baffles simulating natural channel conditions giving the fish enough time to rest while using their burst velocity. Literature is overwhelming with the studies about the baffle design, effect on velocity, flow pattern, and turbulence intensity (Katopodis, Robinson, & Sutherland, 1978; Morrison, Hotchkiss, Stone, Thurman, & Horner-Devine, 2009; Katopodis, Introduction to fishway design, 1992; Schall, Thompson, Zerges, & Kilgore, 2012).

Fish passage design considerations mostly come in the form of state manuals rather than journal publications. Federal Highway Administration (FHWA) jointly with the state of Alaska department

of transportation published guidelines to design culverts according to the weak-swimming fish dating back to 1991 (Behlke, Kane, McLean, & Travis, 1991; Katopodis, 1992). They studied Arctic Grayling fish in detail and recommended that their design criteria work for the Class-I fish so called low performance swimmers.

In 1996, Montana Department of Transportation, Research, Development and Technology transfer program in cooperation with the US FHWA released a fish passage design manual. In this publication, the fish passages in Montana, US were investigated in terms of biological (fish species, size of the fish, jumping ability, and seasonal feeding and spawning migrations) and hydraulic criteria (flow rate, type, roughness, length, and slope of the culvert) influencing fish. Further, they also confirmed that the fish passage design should be based on non-salmonids due to the reason that they are weaker swimmers compared to the salmonids in case both species coexist (Stein & Tillinger, 1996).

Washington Department of Fish and Wildlife released road culvert designs with fish considerations in 1999. Migration barriers were identified whenever culverts experience at least one of the five characteristics: i) drop at outlet, ii) high velocity within barrel, iii) inadequate depth in barrel, iv) high turbulence within culvert, or v) debris accumulation at inlet. They assessed fish passage culverts from hydraulic, design, siting, and maintenance perspectives (Bates, 1999).

In 2002, a new approach was developed for fish passage design considering stream simulation and hydraulic criteria. The stream simulation criterion was defined as designing culverts wider than natural channels whereas hydraulic criterion was defined as designing culverts with minimum depth as well as maximum hydraulic drop. Permissible depths and velocities were found

to be 0.8 to 1 foot and 2.0 to 6.0 feet per second, accordingly (Rowland, Hotchkiss, & Barber, 2002).

Velocity distributions in embedded and non-embedded CMPs were studied by Garner (2011). She compared embedded and equivalent non-embedded culverts, and confirmed that embedded culverts provide more reduced velocity zones for fish, specially for cross-sections one diameter downstream of the inlet. Embedding resulted in no turbulence change or a slight change near the inlet (Garner, 2011).

Recently, FHWA published two comprehensive design manuals, one from Hydraulic Design Series (HDS) and the other one from Hydraulic Engineering Circular (HEC). HDS 5 focuses on general purpose culvert design and provides some suggestions regarding aquatic organisms (Schall, Thompson, Zerges, & Kilgore, 2012). HEC 26 includes to the date information needed to design passages considering aquatic organisms including fish (Kilgore, Bergendahl, & Hotchkiss, 2010). Design relies on HEC-RAS software simulations facilitating design discharge and later verifying bed stability. Issues of construction and post construction were covered thoroughly. As a velocity model, both manuals take advantage of the well-developed Manning approach and, therefore, need information regarding the roughness on the bed.

### 2.3 Experimental Quantitative Visualization

Water movement study and visualization was portrayed by Leonardo Da Vinci in about 1506. Allegedly, he took advantage of grass seeds to visualize the trajectories of a fluid parcel as it moved in a river. Da Vinci's successors, established basic hydraulic laws and improved the existing ones; nevertheless, it was not until the 20<sup>th</sup> century that the advancement in optical physics (i.e., laser optics) as well as electronics (i.e., computers and high-speed cameras) revealed small-scale

processes in fluids involving turbulence with further precision. The start of quantitative visualization can be traced back to 1917 where Naylor and Frazier investigated the history of eddying flow past a model immersed in water by the aid of cinematographic photography (Adrian R. J., 2009). After 1917, scientists developed various techniques to visualize and measure the flow velocity among which Particle Image Velocimetry (PIV) serves as the most popular one. In following paragraphs PIV and its more developed version, Stereoscopic Particle Image Velocimetry (S-PIV) will be investigated.

### *2.3.1 Particle Image Velocimetry (PIV)*

Particle Image Velocimetry (PIV) is a non-intrusive and whole flow field measuring technique for assessment of the mean and instantaneous velocity vectors within a single plane of interest. PIV in its simplest form consists of a double-pulsed laser with a synchronized camera equipped with a Charge-coupled Device (CCD) employed to capture particle displacements in successive video frames (Adrian R. J., 1991; Raffel, Willert, Werely, & Kompenhans, 2007; Adrian & Westerweel, 2011). Subsequently, image-processing algorithms (Keane & Adrian, 1992) would be utilized to arrive at a final velocity distribution with an exceptional spatial resolution. Adoption of a density close to that of a testing medium and an appropriate size of particles are of a great importance since it ensures that seeding particles are faithfully following the flow as well as scattering enough incident laser even in low laser energy (Melling, 1997).

### *2.3.2 Stereoscopic Particle Image Velocimetry (S-PIV)*

Sophisticated real-world problems raised the interest among scholars to direct the studies toward three-dimensional (3D) PIV with an increased temporal and spatial resolution (Adrian R. J., 1991). Reconstructing out-of-plane velocity vector for highly 3D flows and accounting for traditional PIV

perspective errors caused by the imbedded velocity component were major dilemmas that needed to be addressed. Scientists focused on two technical categories: those in which the 3D velocity is calculated from a 3D domain (e.g., Holographic PIV, Tomographic PIV and Scanning PIV); or those which the 3D velocity is reconstructed from 2D domain. Having long calculation time and costly apparatus, the first category techniques were not applied to the practical cases. For the latter one, Stereoscopic Particle Image Velocimetry (S-PIV), dual plane S-PIV and off-axis S-PIV have been successfully developed (Adrian & Westerweel, 2011). In S-PIV, two coupled cameras capture the same plane at the same time but with different off-axis view angles. Both cameras should focus on the same spot in the testing medium and calibrated properly (Bjorkquist, 2002). Velocity components that are obtained from cross-correlated (Keane & Adrian, 1992) dewarped images are sufficient to retrieve the third out-of-plane velocity component (Willert, 1997; Prasad, 2000).

#### 2.3.2.1 Stereovision

Human 3D perception of 2D views (binocular vision) is achieved with the coordinated use of both eyes. From technical point of view, stereovision is the impression of the third spatial dimension (i.e., depth) from two dissimilar views of the same scene. Being inspired by this notion, S-PIV was developed based on two approaches: translational displacement configuration (Figure 2.1) in which the disparity<sup>2</sup> is accomplished by having CCD cameras' optical axes parallel to each other and perpendicular to the object plane (Jacquot & Rastogi, 1981; Arroyo & Greated, 1991; Prasad & Adrian, 1993; Gauthier & Riethmuller, 1988); and angular displacement configuration (Figure 2.2) in which camera lens axis subtends an oblique angle to the laser sheet

---

<sup>2</sup> The difference in image location of an object seen from a right and left camera in S-PIV.

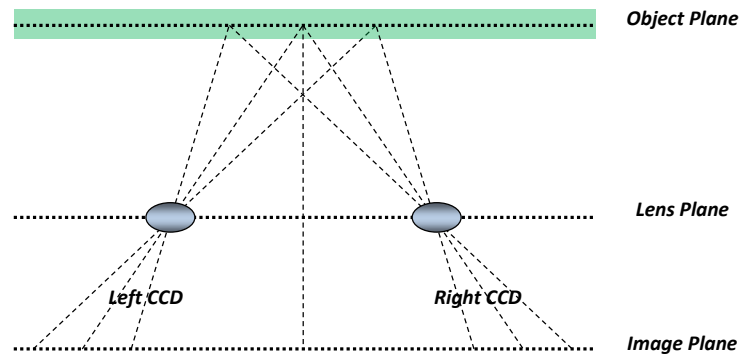


**Figure 2.1 S-PIV Translational Configuration**

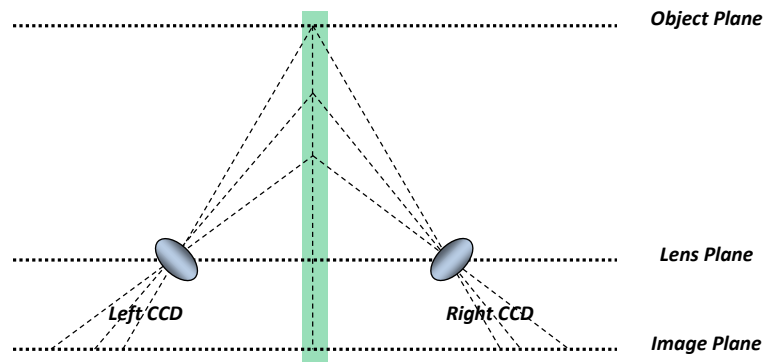


**Figure 2.2 S-PIV Angular Configuration**

(Willert, 1997; Prasad, 2000). Having advantages of convenient mapping, easy to apply and well-focused images, the translational method also benefits from uniform magnification. However, it was pointed out that the reduced overlap field of view is one of the shortcomings of the aforementioned approach (Gauthier & Riethmuller, 1988). The upper bound to the off-axis angle subtended by the center of the lens to the center of the region of interest (owing to the design of the lens) urged scientists to develop an alternative approach. To address the upper bound off-axis angle restriction, in the angular displacement system, the cameras' optical axes are aligned neither parallel with each other nor orthogonal to the object plane (Willert, 1997; Prasad, 2000). This configuration will significantly reduce the out-of-plane velocity component relative error

(Prasad, 2000). However, in the angular configuration, the object plane, lens plane and image plane are not parallel anymore which reduces the sharpness of the particles in the image. Maintaining the object, lens and image plane collinear (Scheimpflug condition) ensures high quality images in sharp focus (Prasad & Jenson, 1995). Alternatively, the depth of the view field could be increased with manipulation in camera magnification, lens f-number and/or laser wavelength (Prasad & Adrian, 1993). Nevertheless, the nominal magnification is not uniform along the view field which may be compensated by computer based sensitivity analysis so called ray-tracing (Zang & Prasad, 1997). In this contribution, the angular system similar to that of the (Willert, 1997) has been employed. Therefore, further elaboration will be made on the angular configuration theory and related concepts, only.

#### 2.3.2.2 Dewarping Images

As was mentioned previously, magnification is not uniform along the image in the angular configuration due to the oblique viewing angle of the lens plane and the object plane. In addition, associating image pixel coordinates with real-world physical coordinates is required in almost all image processing techniques (Willert, 2006). Mathematically speaking, a geometric back projection algorithm, transforming the object plane to the image plane based on geometric optics and with the knowledge of lens focal length, the angle between various planes, the actual position of the lens plane and the nominal magnification factor (magnification along principal optical axis,  $M_o$ ) may be employed to achieve the desired result (Willert, 1997). Therefore, we have

$$X = f(x, y, fl, \varphi, \psi, M_o) \quad Y = f(x, y, fl, \varphi, \psi, M_o) \quad \mathbf{1}$$

where  $X$  and  $Y$  are physical coordinates;  $x$  and  $y$  are the corresponding coordinates of the points in images;  $fl$  is lens focal length;  $\varphi$  is the angle between the image plane and the lens plane and

$\psi$  is the angle between the lens plane and the object plane. However, some of the parameters above are difficult to determine or even with a high accurate measurement this approach does not account for lens imperfections (owing to the lens design) as well as radial distortions (owing to the liquid-air interface). A rather pragmatic approach is to place a planar calibration target with regularly spaced markers (uniform Cartesian grid or separated objects e.g., dots or crosses) at exactly the position of the light sheet (Sollof, Adrian, & Liu, 1997; Willert, 1997; Bjorkquist, 2002). Subsequently, the real-world coordinates of the calibration grid are acquired as input for the calibration algorithm. Moreover, the position of the markers on the images is readily measured using image processing methods in pixels. First order, or in complex distorted geometries, second-order polynomial mapping function coefficients may be evaluated minimizing a non-linear least squares fit to point pairs ( $\emptyset$ ) as following (Ehrenfried, 2002):

$$\emptyset = \sum_{i=1}^N \left[ \left( X_i - \frac{P_x(x_i, y_i)}{Q(x_i, y_i)} \right)^2 + \left( Y_i - \frac{P_y(x_i, y_i)}{Q(x_i, y_i)} \right)^2 \right] \quad 2$$

With

$$Q(x, y) = C_0 + C_1x + C_2y + C_3x^2 + C_4y^2 + C_5xy \quad 3$$

$$P_x(x, y) = C_6 + C_7x + C_8y + C_9x^2 + C_{10}y^2 + C_{11}xy \quad 4$$

$$P_y(x, y) = C_{12} + C_{13}x + C_{14}y + C_{15}x^2 + C_{16}y^2 + C_{17}xy \quad 5$$

where  $N$  is the number of the pair of template points;  $C_0$  through  $C_{17}$  are polynomial coefficients.

$Q$ ,  $P_x$  and  $P_y$  are polynomial functions of a given order.  $x$ ,  $y$  and  $X$ ,  $Y$  are already defined.

### 2.3.2.3 Reconstruction Geometry

Following the approach proposed by (Willert, 1997), when the cameras are placed on either side of the light sheet symmetrically, the images are warped into the light sheet identically. Further, since it is possible to calibrate cameras to capture exactly the same view field, the need for



interpolation to one global coordinate is addressed. The relationship between the true particle displacements and the apparent displacements measured by cameras are readily derived examining Figure 2.2:

$$\begin{aligned}
 dx &= \frac{dx_l \tan \alpha_r - dx_r \tan \alpha_l}{\tan \alpha_r - \tan \alpha_l} & dy &= \frac{dy_l \tan \beta_r - dy_r \tan \beta_l}{\tan \beta_r - \tan \beta_l} \\
 dz &= \frac{dx_l - dx_r}{\tan \alpha_r - \tan \alpha_l} & \text{or} & & dz &= \frac{dy_l - dy_r}{\tan \beta_r - \tan \beta_l}
 \end{aligned} \tag{6}$$

with

$$\begin{aligned}
 \tan \alpha_r &= \frac{x_p - x_r}{z_p - z_r} & \tan \beta_r &= \frac{y_p - y_r}{z_p - z_r} \\
 \tan \alpha_l &= \frac{x_p - x_l}{z_p - z_l} & \text{or} & & \tan \beta_l &= \frac{y_p - y_l}{z_p - z_l}
 \end{aligned} \tag{7}$$

where  $dx_r$ ,  $dy_r$  and  $dx_l$ ,  $dy_l$  are the projected horizontal and vertical displacements of a particle recorded onto the right and left camera, respectively;  $dx$ ,  $dy$  and  $dz$  are the real-world displacement of a particle;  $x_p$ ,  $y_p$  and  $z_p$  are the physical coordinates of an arbitrary particle in the light sheet;  $x_r$ ,  $y_r$  and  $x_l$ ,  $y_l$  are the projected coordinates of the particle p recorded on the right and left camera, accordingly.  $\alpha_r$  and  $\alpha_l$  are the angle enclosed by the viewing ray and the light sheet normal projected onto the  $xz$  plane from right and left camera, respectively.  $\beta_r$  and  $\beta_l$  are the angle enclosed by the viewing ray and the light sheet normal projected onto the  $yz$  plane from right and left camera, respectively.

The method discussed above was proposed for industrial wind tunnel flow applications. As a case study, unsteady flow field of a vortex ring passing through a laser light sheet was successfully measured (Willert, 1997).

The more severe problems arise when the angular setup is employed in the multiphase flows (i.e., flows with liquid-air interface). Due to the difference in the refractive index of the test flow and

air, aberrations at the edges of the liquid-air interface may cause radial distortions. One way to address this issue is to incorporate a triangular thin-walled glass prism filled with test flow, so the lens will continue enjoying orthogonal orientation (Prasad & Jenson, 1995).

## 2.4 Comments and Knowledge Gaps

The majority of the early work depends on the Manning equation which in turn depends on Manning roughness coefficient. This coefficient is affected by many parameters such as the free surface, boundary shape and the flow depth. Therefore, for an accurate culvert design, information regarding roughness is needed to be determined beforehand either through physical or numerical modeling. The literature lacks an accurate velocity distribution and shear stress model for partially filled circular open channel flows, which are common in many man-made crossings. Even if a model exists, it is incapable of retrieving the local velocities due to the averaging nature of these types of models.

Another shortcoming of the available models is that none of them has a closed form solution or solidly based analytical equation. They are based on the mathematical intuition rather than physically based mathematical modeling. Further, the existing models are case-sensitive and most of the time need experimental data to assess the fitting parameters.

## CHAPTER 3: EXPERIMENTAL PROCEDURE

In this chapter, the experimental equipment and their setup as well as the CMP preparation and the bed roughness sieve analysis will be presented. All the activities explained in this Chapter, lasted for two years and were conducted in the FHWA's Turner-Fairbank Highway Research Center.

### 3.1 Experimental Setup

#### 3.1.1 Flume

The experiment was carried out in a rectangular cross-section tilting flume at Turner-Fairbank Highway Research Center located in Mclean, VA, United States (Figure 3.1). The flume was 9 m long, 0.45 m wide (barrel) and 0.28 m deep. A honeycomb was placed in the trumpet-shaped inlet to channelize the water with the purpose of ensuring the homogeneity of the flow.

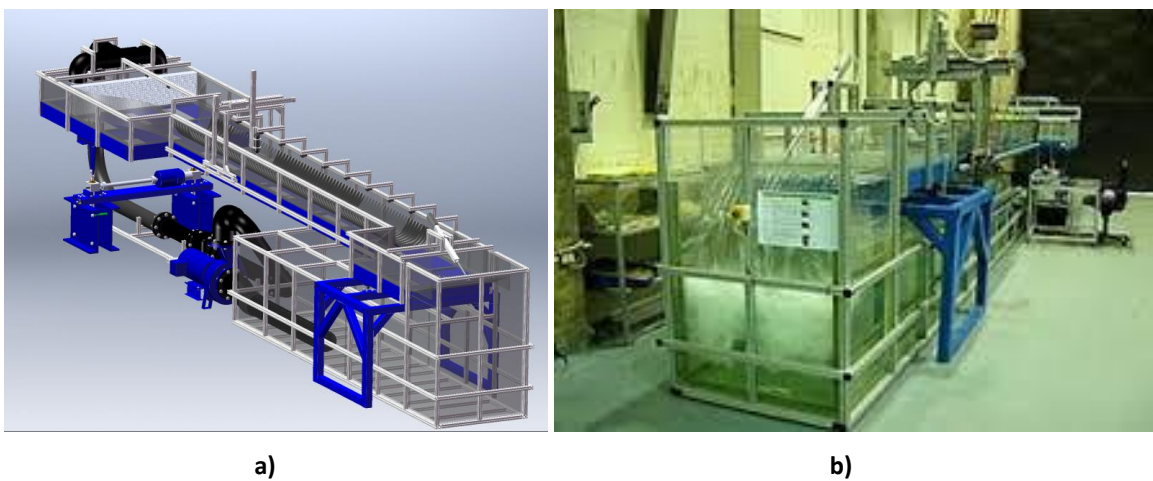


**Figure 3.1 Tilting Flume with the Culvert inside**  
a) Modeled in Solid Works b) Real-World Picture



a)

b)

**Figure 3.2 S-PIV Setup a) Front View b) Side View**

13 ultrasonic sensors (UNDK 30U6103/S14) from Baumer Electronics were utilized to measure water surface profile, simultaneously. Flow condition was controlled both with screw jacks to raise the upstream end of the flume while lowering the downstream end and a bottom-hinged flap gate in the exit section of the flume to reach uniform flow condition under steady state.

Streamwise three component velocity distribution was measured at the midway section between the inlet and outlet for arbitrary discharges according to the test matrix (see Appendix A).

### *3.1.2 Stereoscopic Particle Image Velocimetry (S-PIV) Setup*

A double-pulsed Solo 120 PIV New Wave Research Nd: YAG laser along with a pair of Megaplus ES 1.0 digital cameras from Roper Scientific MASD Inc. were configured in LabView to operate in a synchronized manner (Figure 3.2). The spatial resolution was limited to 960 (H) by 960 (V) pixels which was implemented in the CCD array. The camera was connected through a 68-pin SCSI cable to the frame grabber card and could capture up to 30 images per second. It also featured a built-in electronic shutter with exposure times as short as 127 microseconds for maximum flexibility and performance when imaging fast moving objects. CCD cameras were equipped with two Sigma

zoom lenses with a focal length ranging from 28 mm to 70 mm and an 8-level f-number from 2.8 to 32.

Silver-coated hollow glass spheres (AGSL150-16TRD from the Potters Industries Inc., Carlstadt, NJ) with an average diameter of 69  $\mu\text{m}$ , density of 0.93  $\text{g}/\text{cm}^3$ , and 17.7% weight of silver coated on their surfaces were introduced into the flow.

### 3.1.3 Acoustic Doppler Velocimetry (ADV) Setup

Acoustic Doppler Velocimeter (ADV) is an intrusive remote-sensing device originally developed for inlets and entrances hydrodynamics investigation at the U.S. Army Engineer Waterways Experiment Station (Kraus, Lohrmann, & Cabrera, 1994). The theory is based on the shift in received frequency so-called Doppler effect. The device sends out a beam of acoustic waves at a fixed frequency from a transmitter probe (e.g., 5 to 10 cm). These waves bounce off of moving particulate matter in the water and three acoustic receivers sense the shift in the frequency.

ADV technical details and shortcomings are out of the scope of this contribution, and for more information the reader is referred to (Sontek, 2001; Precht, Janssen, & Huettel, 2006).

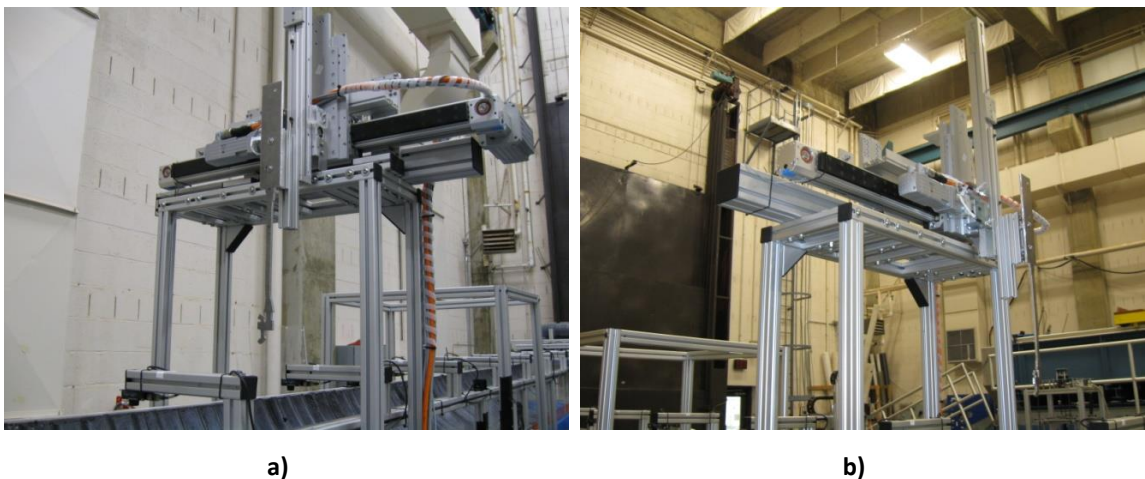


Figure 3.3 ADV Setup a) Front View b) Side View

In this study, a 16 MHz microADV from SonTek was mounted on a robot (Figure 3.3) and controlled with a LabView program to evaluate the accuracy and efficiency of S-PIV results. 1500 sample points were adopted for each velocity measurement to precisely average fluctuating wiggly streamlines in turbulent scale.

### 3.2 Corrugated Metal Pipe (CMP) Specifications

An annular corrugated pipe was obtained from CONTECH Co. with the following technical specifications. Note that  $c/k$  is the cycle pitch to depth ratio which for this case was 3 (Table 3.1 and Figure 3.4). Figure 3.5 depict the different views of the corrugated pipe before any change. According to the factory suggestion, the Manning roughness coefficient for this pipe was  $n = 0.012$ .

#### 3.2.1 CMP Sections

During a culvert service time, due to flooding and other natural events, culverts can become a depository for unwanted materials. To simulate the effect of the bed material on the velocity distribution three test scenarios were devised with various sediment depths ( $h'$ ) of  $0\%D$ ,  $15\%D$ ,

**Table 3.1 Handling Weights for CMP Used in the Experiment (3"x1")**

Weight (Pounds/Linear Foot)			
Inside Diameter of CMP (inches)	CMP Gage	CMP Thickness (inches)	Galvanized and Aluminized <sup>3</sup>
36	16	0.064	33

<sup>3</sup> Weights for TRENCHCOAT® polymer-coated pipe are 1%-4% higher, varying by gage.

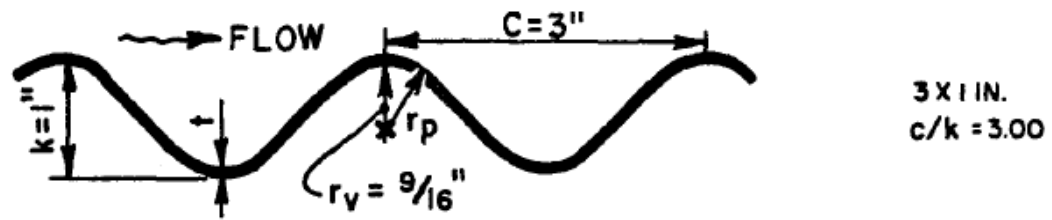


Figure 3.4 Annular CMP Shape (CONTECH Engineered Solutions , 2014)

and  $30\%D$ . Figure 3.6, Figure 3.7 and Figure 3.8 represent the prototype (scaled down) on the left and the symmetrical half of the model on the right. Three flow depths ( $h=3''$ ,  $6''$  and  $9''$ ) were chosen to represent the low flow conditions (see Appendix A and Table A.1).

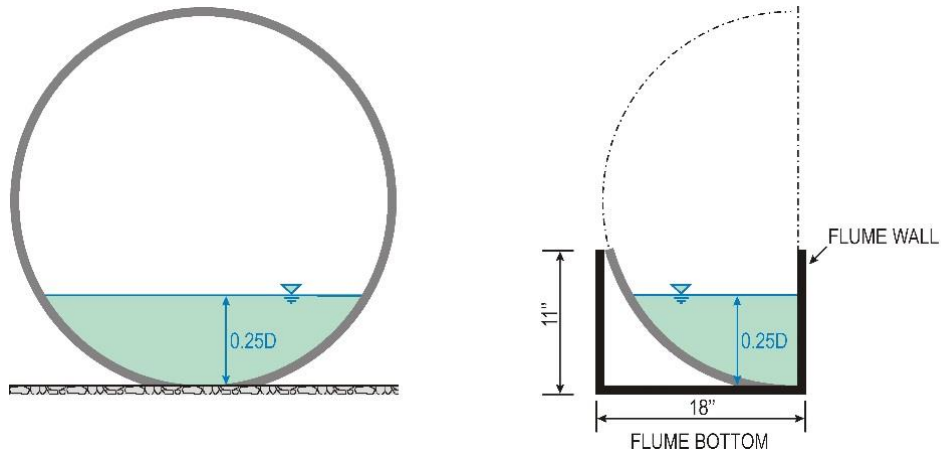
### 3.2.2 CMP Preparation

The real testing starts with preparing the CMP section. For this purpose the original pipe was cut with the help of an Oxygen Acetylene torch. In addition, using an angle grinder the pipe edges that were supposed to lean on the flume wall were made smoother. Pipe surface was coated with a two component special coal tar to eliminate the laser illuminations during S-PIV operation.

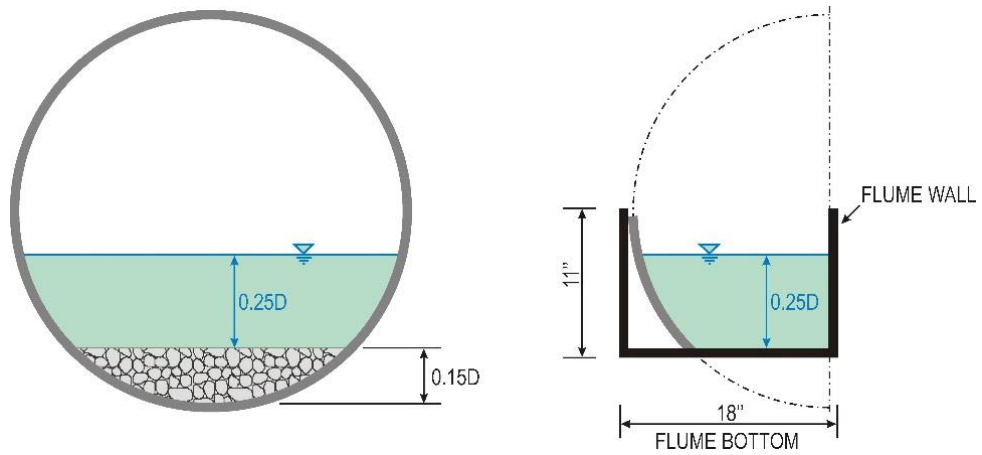


Figure 3.5 CMP a) Lateral Cross-section View b) Isometric View





**Figure 3.6 Bed Elevation at 0% Culvert Diameter and Symmetrical half of the Model**



**Figure 3.7 Bed Elevation at 15% Culvert Diameter and Symmetrical Half of the Model**

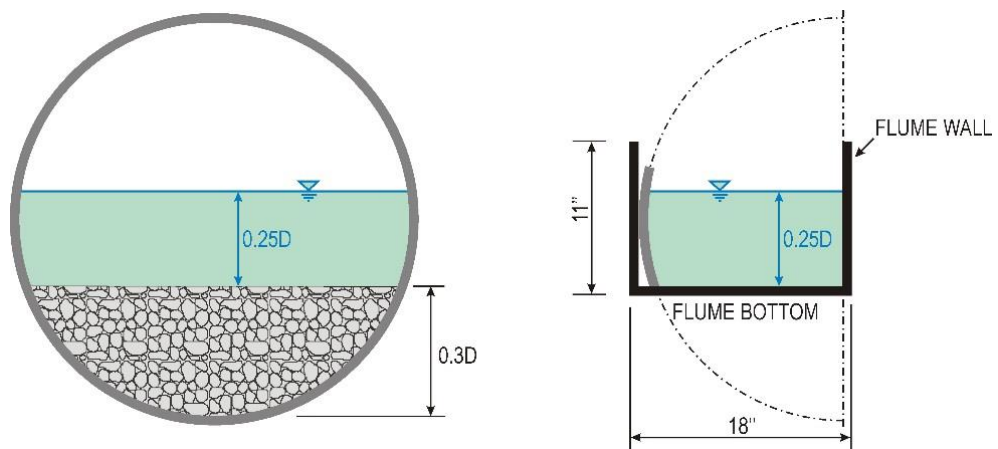


**Figure 3.8 Bed Elevation at 30% Culvert Diameter and Symmetrical Half of the Model**





a)

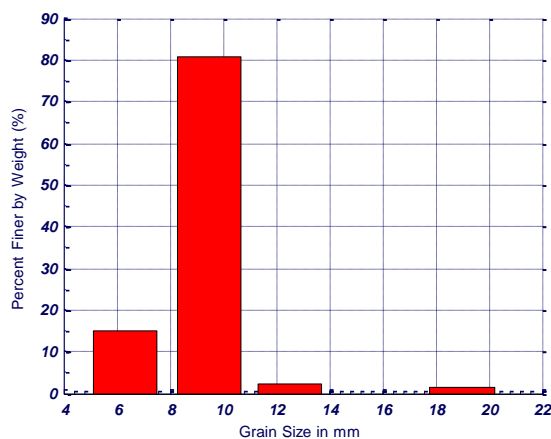
b)

**Figure 3.9 Prepared CMP Section a) Coated with epoxy b) Placed Inside Flume**

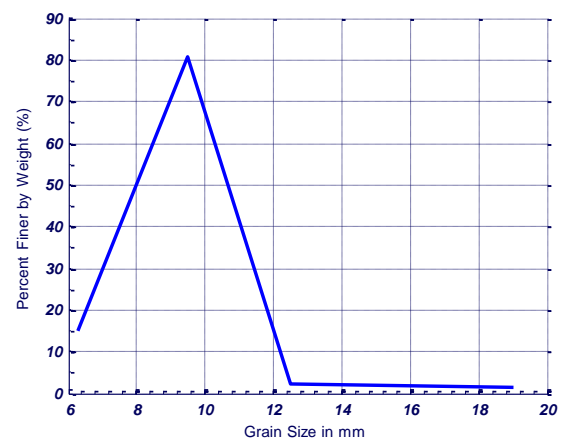
The technical specification of the coating was *C9578402 high performance coal tar epoxy*. This base component needs C9502 504 activator both of which meet C-200 specifications. Figure 3.9 depicts the coated CMP section as well as the CMP placed and sealed inside the flume. The technical specification of the coating was *C9578402 high performance coal tar epoxy*.

### 3.3 Sieve Analysis

Embedded culverts are commonly used to increase the bed roughness which in turn will increase the low velocity region for fish (Garner, 2011). Some experiments included roughness on the bed



a)



b)

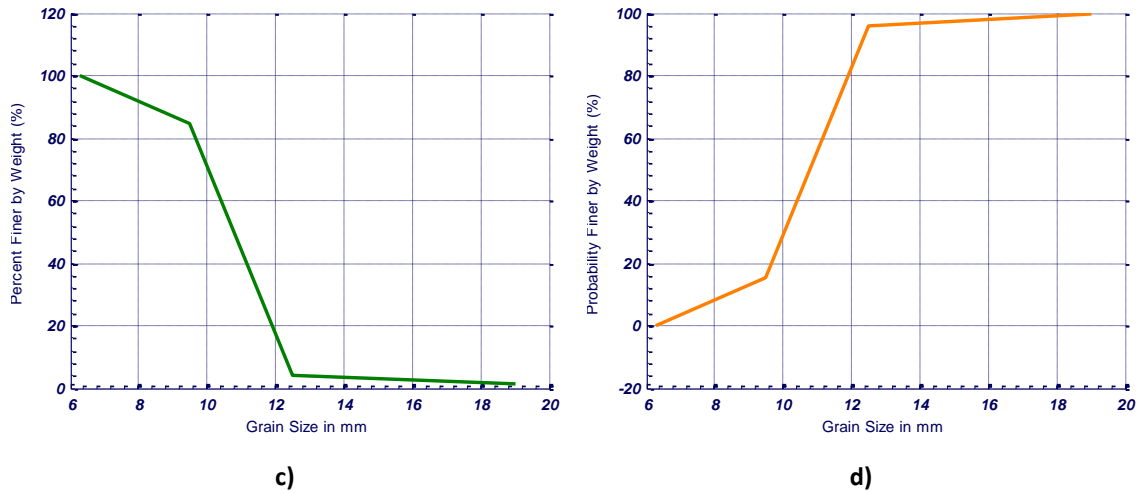


**Figure 3.10 Gravel Properties Used in Roughness Test**

a) Soil Histogram b) Soil Frequency c) Soil Frequency Cumulative d) Soil Cumulative Probability

(see Appendix A). Therefore, gravel with a  $D_{50}$  of at least 10 mm was chosen, and basic soil mechanics tests (sieve analysis) were conducted on it. Note that the soil type used in the

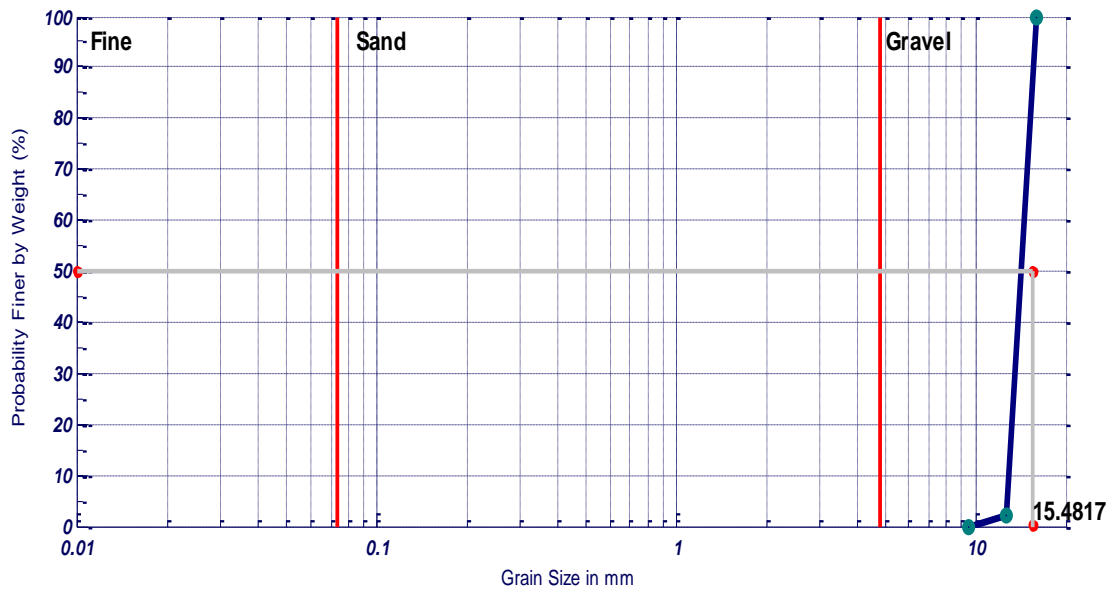


**Figure 3.11 Logarithmic Cumulative Probability**

**Table 3.2 Grain Size for the Proposed Soil**

<b>D<sub>5</sub></b>	<b>D<sub>10</sub></b>	<b>D<sub>16</sub></b>	<b>D<sub>30</sub></b>	<b>D<sub>50</sub></b>	<b>D<sub>60</sub></b>	<b>D<sub>75</sub></b>	<b>D<sub>84</sub></b>	<b>D<sub>95</sub></b>
<b>(mm)</b>	<b>(mm)</b>	<b>(mm)</b>	<b>(mm)</b>	<b>(mm)</b>	<b>(mm)</b>	<b>(mm)</b>	<b>(mm)</b>	<b>(mm)</b>
7.56	8.74	9.55	10.28	10.66	10.78	11.12	11.54	12.40

experiment according to the USCS classification was SP. Figure 3.10 depicts the soil histogram, frequency, cumulative frequency, and cumulative probability curves. Moreover, the cumulative probability curve (Figure 3.10d) shows that the soil completely is in the gravel region. Table 3.2 and Table 3.3 also lists some important information regarding the roughness such as coefficient of uniformity and coefficient of the curvature both of which reveals a uniform but poorly graded soil.

**Table 3.3 Physical Characteristics of the Proposed Soil**

<b>Standard Deviation</b>	<b>Skewness</b>	<b>Kurtosis</b>	<b>Coefficient of uniformity</b>	<b>Coefficient of curvature</b>
7.56	8.74	9.55	10.28	10.66
Very well sorted	Coarse skewed	Very leptokurtic		

## CHAPTER 4: ANALYTICAL SOLUTION TO P-PFF

### 4.1 Newton's Law

Navier and Stokes formulated the governing differential equations of motion for incompressible, Newtonian fluids in the 1840s (Young, Munson, Okiishi, & Huebsch, 2011). Equations (8-10) list the Navier-Stokes (NS) equations in cylindrical coordinates:

$$\begin{aligned}
 r: \quad & \rho \left( \frac{\partial u_r}{\partial t} + u_r \frac{\partial u_r}{\partial r} + \frac{u_\theta}{r} \frac{\partial u_r}{\partial \theta} + u_z \frac{\partial u_r}{\partial z} - \frac{u_\theta^2}{r} \right) \\
 & = -\frac{\partial p}{\partial r} + \mu \left[ \frac{1}{r} \frac{\partial}{\partial r} \left( r \frac{\partial u_r}{\partial r} \right) + \frac{1}{r^2} \frac{\partial^2 u_r}{\partial \theta^2} + \frac{\partial^2 u_r}{\partial z^2} - \frac{u_r}{r^2} - \frac{2}{r^2} \frac{\partial u_\theta}{\partial \theta} \right] + \rho g_r
 \end{aligned} \tag{8}$$

$$\begin{aligned}
 \theta: \quad & \rho \left( \frac{\partial u_\theta}{\partial t} + u_r \frac{\partial u_\theta}{\partial r} + \frac{u_\theta}{r} \frac{\partial u_\theta}{\partial \theta} + u_z \frac{\partial u_\theta}{\partial z} + \frac{u_r u_\theta}{r} \right) \\
 & = -\frac{1}{r} \frac{\partial p}{\partial \theta} + \mu \left[ \frac{1}{r} \frac{\partial}{\partial r} \left( r \frac{\partial u_\theta}{\partial r} \right) + \frac{1}{r^2} \frac{\partial^2 u_\theta}{\partial \theta^2} + \frac{\partial^2 u_\theta}{\partial z^2} - \frac{u_\theta}{r^2} + \frac{2}{r^2} \frac{\partial u_r}{\partial \theta} \right] + \rho g_\theta
 \end{aligned} \tag{9}$$

$$z: \quad \rho \left( \frac{\partial u_z}{\partial t} + u_r \frac{\partial u_z}{\partial r} + \frac{u_\theta}{r} \frac{\partial u_z}{\partial \theta} + u_z \frac{\partial u_z}{\partial z} \right) = -\frac{\partial p}{\partial z} + \mu \left[ \frac{1}{r} \frac{\partial}{\partial r} \left( r \frac{\partial u_z}{\partial r} \right) + \frac{1}{r^2} \frac{\partial^2 u_z}{\partial \theta^2} + \frac{\partial^2 u_z}{\partial z^2} \right] + \rho g_z \tag{10}$$

where  $u_r$ ,  $u_\theta$  and  $u_z$  are instantaneous velocity in  $r$ ,  $\theta$  and  $z$  directions, accordingly;  $g_r$ ,  $g_\theta$  and  $g_z$  are gravitational acceleration, in respective directions;  $\mu$  and  $\rho$  are the dynamic viscosity and density of the fluid; and  $p$  is pressure field.

The NS equations together with the mass conservation law, Eq. 11 govern a full model for motion of fluids. Mathematically speaking, four unknowns ( $u_r$ ,  $u_\theta$ ,  $u_z$ , and  $p$ ) and four equations suggest that the model is well-posed. However, due to the inherent complexity<sup>4</sup>, only some simple laminar cases have been solved and verified with the experimental data so far (Guo & Meroney, 2013).

<sup>4</sup> NS equations are from class of second-order nonlinear elliptic partial differential equations.

$$\frac{\partial \rho}{\partial t} + \frac{1}{r} \frac{\partial}{\partial r} (\rho r u_r) + \frac{1}{r} \frac{\partial}{\partial \theta} (\rho u_\theta) + \frac{\partial}{\partial z} (\rho u_z) = 0 \quad 11$$

## 4.2 Reynolds-Averaged Navier-Stokes (RANS) Equations

NS equations are valid for both laminar and turbulent flow conditions. Experiments on turbulent flow show that velocity of the particles varies with respect to both time and space (Young, Munson, Okiishi, & Huebsch, 2011). Although turbulence is proved to be random, some aspects of it can be investigated through the averaging process like all other random phenomena. Statistical averaging of an arbitrary function related with turbulence ( $f$ ) with respect to time in a time period ( $T$ ) longer than that of a typical fluctuation period (Eq. 12) reveals consistent characteristics (Kim, Moin, & Moser, 1987).

$$\bar{f} = \frac{1}{T} \int_t^{t+T} f(r, \theta, z, t) dt \quad 12$$

Besides, the instantaneous velocity distribution may not be of interest from practical point of view in real-world problems.

RANS equations are a time-averaged form of the NS equations and are the starting point for analytical model development. Based on the Reynolds decomposition concept, velocity and pressure can be decomposed into a mean and a fluctuating component (Bonakdari, Larrarte, Lassabatere, & Joannis, 2008) which are listed through Eqs. 13-16

$$u_r(r, \theta, z, t) = \bar{u}_r(r, \theta, z, t) + u'_r(r, \theta, z, t) \quad 13$$

$$u_\theta(r, \theta, z, t) = \bar{u}_\theta(r, \theta, z, t) + u'_\theta(r, \theta, z, t) \quad 14$$

$$u_z(r, \theta, z, t) = \bar{u}_z(r, \theta, z, t) + u'_z(r, \theta, z, t) \quad 15$$

$$p(r, \theta, z, t) = \bar{p}(r, \theta, z, t) + p'(r, \theta, z, t) \quad 16$$

where  $u'_r$ ,  $u'_\theta$  and  $u'_z$  are fluctuating velocity components;  $\bar{u}_r$ ,  $\bar{u}_\theta$  and  $\bar{u}_z$  are time averaged velocity components;  $p'$  is the fluctuating pressure and  $\bar{p}$  is the time averaged pressure.

Substituting the velocity and pressure from Eqs. (13-16) into Eqs. (8-11) we end up with

$$\begin{aligned} r: \quad & \rho \left( \frac{D\bar{u}_r}{Dt} - \frac{\bar{u}_\theta^2}{r} \right) = -\frac{\partial \bar{p}}{\partial r} + \mu \left( \nabla^2 \bar{u}_r + \frac{\bar{u}_r}{r^2} - \frac{2}{r^2} \frac{\partial \bar{u}_\theta}{\partial \theta} \right) \\ & - \rho \left[ \frac{1}{r} \frac{\partial}{\partial r} (\overline{ru_r'^2}) + \frac{1}{r} \frac{\partial}{\partial \theta} (\overline{u_r' u_\theta'}) + \frac{\partial}{\partial z} (\overline{u_r' u_z'}) - \frac{\overline{u_\theta'^2}}{r} \right] + \rho g_r \end{aligned} \quad 17$$

$$\begin{aligned} \theta: \quad & \rho \left( \frac{D\bar{u}_\theta}{Dt} + \frac{2\bar{u}_r \bar{u}_\theta}{r} \right) = -\frac{1}{r} \frac{\partial \bar{p}}{\partial \theta} + \mu \left( \nabla^2 \bar{u}_\theta - \frac{\bar{u}_\theta}{r^2} + \frac{2}{r^2} \frac{\partial \bar{u}_r}{\partial \theta} \right) \\ & - \rho \left[ \frac{1}{r} \frac{\partial}{\partial \theta} (\overline{u_\theta'^2}) + \frac{\partial}{\partial r} (\overline{u_\theta' u_r'}) + \frac{\partial}{\partial z} (\overline{u_\theta' u_z'}) + \frac{2\overline{u_\theta' u_r'}}{r} \right] + \rho g_\theta \end{aligned} \quad 18$$

$$\begin{aligned} z: \quad & \rho \frac{D\bar{u}_z}{Dt} = -\frac{\partial \bar{p}}{\partial z} + \mu (\nabla^2 \bar{u}_z) \\ & - \rho \left[ \frac{\partial}{\partial z} (\overline{u_z'^2}) + \frac{1}{r} \frac{\partial}{\partial r} (\overline{ru_r' u_z'}) + \frac{1}{r} \frac{\partial}{\partial \theta} (\overline{u_\theta' u_z'}) \right] + \rho g_z \end{aligned} \quad 19$$

$$\frac{\partial \bar{u}_r}{\partial r} + \frac{\bar{u}_r}{r} + \frac{1}{r} \frac{\partial (\bar{u}_\theta)}{\partial \theta} + \frac{\partial (\bar{u}_z)}{\partial z} = 0 \quad 20$$

where operators  $\frac{D}{Dt}$  and  $\nabla^2$  are defined as:

$$\frac{D}{Dt} = \frac{\partial}{\partial t} + u_r \frac{\partial}{\partial r} + \frac{u_\theta}{r} \frac{\partial}{\partial \theta} + u_z \frac{\partial}{\partial z} \quad 21$$

$$\nabla^2 = \frac{\partial^2}{\partial r^2} + \frac{1}{r} \frac{\partial}{\partial r} + \frac{1}{r^2} \frac{\partial^2}{\partial \theta^2} + \frac{\partial^2}{\partial z^2} \quad 22$$

The RANS equations are mathematically analogous with the NS equations except for the turbulence fluctuating terms which are treated as additional shear stresses appearing in only turbulent flow. Therefore, a general stress tensor in turbulent flow motion can be summarized as (Granger, 1995):

$$P_{rr} = -\bar{p} + 2\mu \frac{\partial \bar{u}_r}{\partial r} - \rho \overline{u_r'^2} \quad 23$$

$$P_{\theta\theta} = -\bar{p} + 2\mu \left( \frac{1}{r} \frac{\partial \bar{u}_\theta}{\partial \theta} + \frac{\bar{u}_r}{r} \right) - \rho \overline{u_\theta'^2} \quad 24$$

$$P_{zz} = -\bar{p} + 2\mu \frac{\partial \bar{u}_z}{\partial z} - \rho \overline{u_z'^2} \quad 25$$

$$P_{r\theta} = \mu \left( \frac{\partial \bar{u}_\theta}{\partial r} + \frac{1}{r} \frac{\partial \bar{u}_r}{\partial \theta} - \frac{\bar{u}_\theta}{r} \right) - \rho \overline{u_r' u_\theta'} \quad 26$$

$$P_{zr} = \mu \left( \frac{\partial \bar{u}_r}{\partial z} + \frac{\partial \bar{u}_z}{\partial r} \right) - \rho \overline{u_r' u_z'} \quad 27$$

$$P_{\theta z} = \mu \left( \frac{1}{r} \frac{\partial \bar{u}_z}{\partial \theta} + \frac{\partial \bar{u}_\theta}{\partial z} \right) - \rho \overline{u_\theta' u_z'} \quad 28$$

where  $P_{ij}$  is the stress tensor in  $j$  direction acting on a surface perpendicular to direction  $i$ .

### 4.3 Governing Equations

Figure 4.1 depicts a circular open channel flow with spanwise ( $u_x$ ), vertical velocity ( $u_y$ ), and streamwise ( $u_z$ ) components in  $x$ ,  $y$  and  $z$  directions, respectively. For the sake of geometry, cylindrical coordinates are adopted with  $u_r$ ,  $u_\theta$  and  $u_z$  in  $r$ ,  $\theta$  and  $z$  directions (Figure 4.2) which is related to the Cartesian coordinates through Eqs. 29-33

$$x = r \cos \theta \quad -R < x < R \quad 29$$

$$y = R - r \sin \theta \quad 0 < y < R \quad 30$$

$$r = \sqrt{x^2 + (R - y)^2} \quad 0 < r < R \quad 31$$

$$\theta = \tan^{-1} \left| \frac{R - y}{x} \right| \quad 0 < \theta < 2\pi \quad 32$$

$$\bar{u}_r = \frac{-\bar{u}_y}{\sin \theta} \quad \bar{u}_\theta = \frac{-\bar{u}_x}{\sin \theta} \quad \bar{u}_z(r, \theta) = \bar{u}_z(x, y) \quad 33$$

where  $R$  is the culvert radius.

Mass conservation law for an incompressible steady state flow in cylindrical coordinates reads:

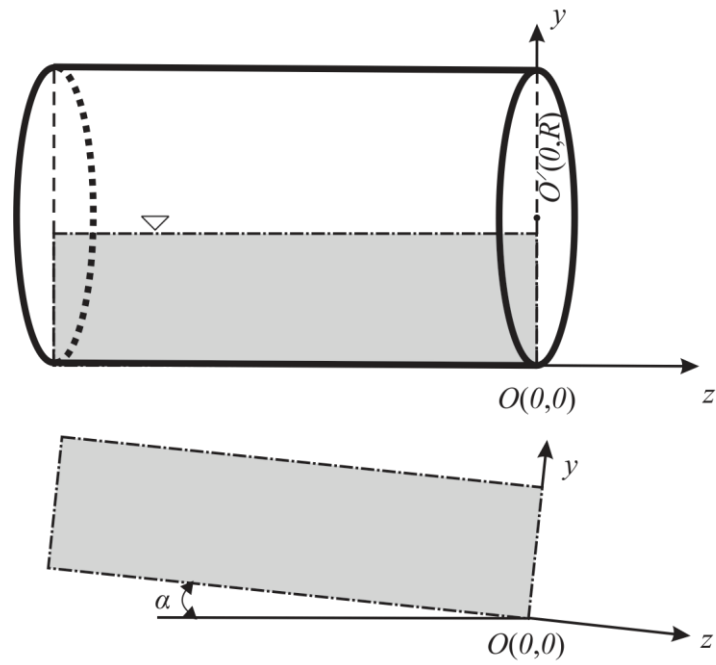


Figure 4.1 Circular Open Channel Flow Longitudinal View

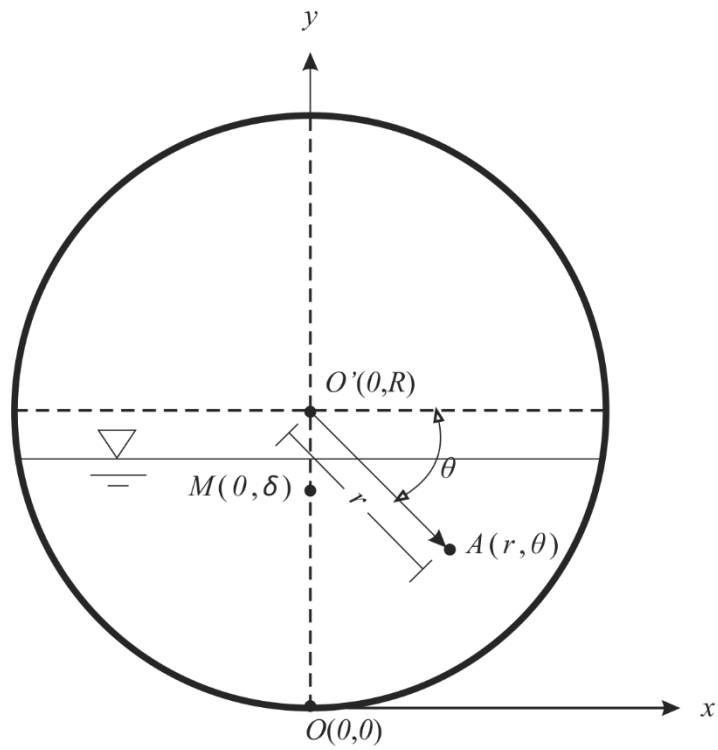


Figure 4.2 Circular Open Channel Flow Cross-Sectional View



$$\frac{\partial \bar{u}_r}{\partial r} + \frac{\bar{u}_r}{r} + \frac{1}{r} \frac{\partial (\bar{u}_\theta)}{\partial \theta} + \frac{\partial (\bar{u}_z)}{\partial z} = 0 \quad 34$$

Assuming a fully-developed and unidirectional flow, it follows that:

$$\frac{\partial (\bar{u}_z)}{\partial z} = 0 \quad 35$$

Equation 35 was already developed through the fully-developed flow assumption which states that the change along the direction of the flow ( $z$ ) is negligible ( $\frac{\partial}{\partial z} = 0$ ). The  $z$  component for the

RANS equation reads:

$$\begin{aligned} \rho \frac{D\bar{u}_z}{Dt} = & -\frac{\partial \bar{p}}{\partial z} + \mu \left( \frac{\partial^2 \bar{u}_z}{\partial r^2} + \frac{1}{r} \frac{\partial \bar{u}_z}{\partial r} + \frac{1}{r^2} \frac{\partial^2 \bar{u}_z}{\partial \theta^2} + \frac{\partial^2 \bar{u}_z}{\partial z^2} \right) \\ & -\rho \left[ \frac{\partial}{\partial z} (\overline{u_z'^2}) + \frac{1}{r} \frac{\partial}{\partial r} (r \overline{u_r' u_z'}) + \frac{1}{r} \frac{\partial}{\partial \theta} (\overline{u_\theta' u_z'}) \right] + \rho g_z \end{aligned} \quad 36$$

According to the experimentally determined velocity counters provided by (Clark & Kehler, 2011; Yoon, Sung, & Lee, 2012; Kehler, 2009), it can be deduced that the gradient in the azimuthal direction ( $\theta$ ) is negligible compared to the radial direction ( $r$ ). It follows that:

$$\frac{1}{r^2} \frac{\partial^2 \bar{u}_z}{\partial \theta^2} \ll \frac{\partial^2 \bar{u}_z}{\partial r^2} \quad 37$$

$$\frac{1}{r} \frac{\partial}{\partial \theta} (\overline{u_\theta' u_z'}) \ll \frac{1}{r} \frac{\partial}{\partial r} (r \overline{u_r' u_z'}) \quad 38$$

The limitation for the above mentioned assumptions is where  $r$  tends to zero, that is the left hand side term in the Eq. 37 and the right hand side term in the Eq. 38 tends to infinity and zero, respectively. It follows that the predicted velocity values close to the center of the pipe will not be reliable. Moreover, assuming a fully-developed uniform and unidirectional flow in the  $z$  direction, Eq. 36 reduces to:

$$\mu \left[ \frac{\partial^2 \bar{u}_z}{\partial r^2} + \frac{1}{r} \frac{\partial \bar{u}_z}{\partial r} \right] - \rho \left[ \frac{1}{r} \frac{\partial}{\partial r} (r \overline{u_r' u_z'}) \right] + \rho g_z = 0 \quad 39$$

The gravity term<sup>5</sup> is adjusted through

$$g_z = g \sin \alpha = gS_0 \quad 40$$

where  $\alpha$  is defined in Figure 4.1. Also,  $S_0$ , channel bottom slope, can be adopted analogous with the Manning model. Equation 39 together with Eq. 40 after simplification result in:

$$r \frac{\partial^2 \bar{u}_z}{\partial r^2} + \frac{\partial \bar{u}_z}{\partial r} - \frac{\rho}{\mu} \left[ \frac{\partial}{\partial r} (r \overline{u'_r u'_z}) \right] + \frac{r \rho g S_0}{\mu} = 0 \quad 41$$

Equation 41 is a non-homogeneous<sup>6</sup> second-order nonlinear partial differential equation, and there is not any unique way to solve this equation. In order to solve Eq. 41, it is integrated between  $r$  and  $\frac{R-h}{\sin \theta}$  with respect to  $r$  where  $h$  is the depth of the fluid.

$$\int_r^{\frac{R-h}{\sin \theta}} r \frac{\partial^2 \bar{u}_z}{\partial r^2} dr + \int_r^{\frac{R-h}{\sin \theta}} \frac{\partial \bar{u}_z}{\partial r} dr - \int_r^{\frac{R-h}{\sin \theta}} \frac{\rho}{\mu} \left[ \frac{\partial}{\partial r} (r \overline{u'_r u'_z}) \right] dr + \int_r^{\frac{R-h}{\sin \theta}} \frac{r \rho g S_0}{\mu} dr = 0 \quad 42$$

With the aid of the method of integration by parts, the first term is split into two terms, and we have:

$$\left( r \frac{\partial \bar{u}_z}{\partial r} \Big|_r^{\frac{R-h}{\sin \theta}} - \int_r^{\frac{R-h}{\sin \theta}} \frac{\partial \bar{u}_z}{\partial r} dr \right) + \int_r^{\frac{R-h}{\sin \theta}} \frac{\partial \bar{u}_z}{\partial r} dr - \left[ \frac{\rho}{\mu} (r \overline{u'_r u'_z}) \right]_r^{\frac{R-h}{\sin \theta}} + \frac{r^2 \rho g S_0}{2\mu} \Big|_r^{\frac{R-h}{\sin \theta}} = 0 \quad 43$$

At the water-air interface, the shear stress is negligible. It implies that  $P_{zr}$  from the stress tensor is negligible at the free surface. Recalling Eq. 27 we have:

$$p_{zr} \Big|_{r=\frac{R-h}{\sin \theta}} = 0 \rightarrow \left[ \mu \left( \frac{\partial \bar{u}_r}{\partial z} + \frac{\partial \bar{u}_z}{\partial r} \right) - \rho (\overline{u'_r u'_z}) \right]_{r=\frac{R-h}{\sin \theta}} = 0 \quad 44$$

<sup>5</sup> Last term on the left hand side of Eq. 39

<sup>6</sup> The right hand side is non-zero and a function of the independent variable  $r$ .

$$\left[ \mu \frac{\partial \bar{u}_z}{\partial r} - \rho \overline{(u'_r u'_z)} \right]_{r=\frac{R-h}{\sin \theta}} = 0 \rightarrow \frac{\partial \bar{u}_z}{\partial r} \Big|_{r=\frac{R-h}{\sin \theta}} = \frac{\rho}{\mu} \overline{(u'_r u'_z)} \Big|_{r=\frac{R-h}{\sin \theta}}$$

where  $r = \frac{R-h}{\sin \theta}$  in the cylindrical coordinate system corresponds to the free surface  $y = h$  in the Cartesian coordinate system.

Substituting Eq. 44 into Eq. 43 we have:

$$\left( r \frac{\partial \bar{u}_z}{\partial r} \Big|_{\frac{R-h}{\sin \theta}} - r \frac{\partial \bar{u}_z}{\partial r} \Big|_r \right) + \left[ -r \frac{\partial \bar{u}_z}{\partial r} \Big|_{\frac{R-h}{\sin \theta}} + r \frac{\rho}{\mu} \overline{(u'_r u'_z)} \Big|_r \right] + \frac{r^2 \rho g S_0}{2\mu} \Big|_r = 0 \quad 45$$

and after simplification we arrive at:

$$-r \frac{\partial \bar{u}_z}{\partial r} + r \frac{\rho}{\mu} \overline{(u'_r u'_z)} + \frac{\rho g S_0}{2\mu} \left[ \left( \frac{R-h}{\sin \theta} \right)^2 - r^2 \right] = 0 \quad 46$$

Boussinesq in 1877 (Nezu & Rodi, 1986) introduced the first hypothesis to model the fluctuating components of the RANS equation as:

$$-\overline{u'_y u'_z} = \nu_t \frac{\partial u_z(x, y)}{\partial y} \quad 47$$

where  $\nu_t$  was named kinematic eddy viscosity. Equation 47 is in Cartesian coordinates and needs to be converted to cylindrical coordinates for our purpose. Using the chain rule we have:

$$\begin{aligned} \frac{\partial}{\partial y} &= \frac{\partial}{\partial r} \frac{\partial r}{\partial y} = \frac{\partial}{\partial r} \left[ \frac{-2(R-y)}{2\sqrt{x^2 + (R-y)^2}} \right] = \frac{\partial}{\partial r} \left( \frac{-r \sin \theta}{r} \right) = -\sin \theta \frac{\partial}{\partial r} \\ \frac{\partial}{\partial y} &= -\sin \theta \frac{\partial}{\partial r} \end{aligned} \quad 48$$

Substituting Eq. 33 and Eq. 48 into Eq. 47 we have:

$$-\overline{u'_y u'_z} = \nu_t \frac{\partial \bar{u}_z(x, y)}{\partial y} \rightarrow \sin \theta \overline{u'_z u'_r} = -\nu_t \sin \theta \frac{\partial \bar{u}_z(r, \theta)}{\partial r}$$

$$-\overline{u'_r u'_z} = -\nu_t \frac{\partial \bar{u}_z(r, \theta)}{\partial r} \quad 49$$

Subsuming Eq. 49 into Eq. 46 we have,

$$\begin{aligned} -r \frac{\partial \bar{u}_z}{\partial r} - r \frac{\nu_t}{\nu} \frac{\partial \bar{u}_z}{\partial r} + \frac{\rho g S_0}{2\mu} \left[ \left( \frac{R-h}{\sin \theta} \right)^2 - r^2 \right] &= 0 \\ \frac{\partial \bar{u}_z}{\partial r} = \left( \frac{1}{r} \right) \left( 1 + \frac{\nu_t}{\nu} \right)^{-1} \frac{\rho g S_0}{2\mu} \left[ \left( \frac{R-h}{\sin \theta} \right)^2 - r^2 \right] & \end{aligned} \quad 50$$

and finally we arrive at:

$$\bar{u}_z(r, \theta) = \int \frac{g S_0}{2r(\nu + \nu_t)} \left[ \left( \frac{R-h}{\sin \theta} \right)^2 - r^2 \right] dr \quad 51$$

#### 4.3.1 Constant Eddy Viscosity Model

It should be noted that the eddy viscosity is not a function of the fluid but is a function of the flow (Granger, 1995). Therefore, it should be a function of both radial and azimuthal coordinates. As an extreme case, Eq. 51 is solved assuming a constant eddy viscosity model. It follows that:

$$\bar{u}_z = \frac{g S_0}{2(\nu + \nu_t)} \left[ \left( \frac{R-h}{\sin \theta} \right)^2 \ln r - \frac{r^2}{2} \right] + C \quad 52$$

where  $C$  is the constant of the integration. According to the no-slip boundary condition,  $\bar{u}_z(r, \theta)$  is equal to zero while  $r$  is equal to the radius of the pipe ( $R$ ). From here:

$$C = -\frac{g S_0}{2(\nu + \nu_t)} \left[ \left( \frac{R-h}{\sin \theta} \right)^2 \ln R - \frac{R^2}{2} \right] \quad 53$$

Equation 52 together with Eq. 53 result in:

$$\bar{u}_z(r, \theta) = \frac{g S_0}{2(\nu + \nu_t)} \left[ \left( \frac{R-h}{\sin \theta} \right)^2 \ln \frac{r}{R} - \frac{r^2 - R^2}{2} \right] \quad 54$$

Assuming a case where there is not any slope in the  $x$  direction, the maximum velocity should be on some point along the centerline (due to symmetry) and below the free surface (due to secondary flow<sup>7</sup>) contrary to the F-FPF where it is on the center of the pipe. Therefore, we have

$$u_{max} = \frac{gS_0}{2(\nu + \nu_t)} \left[ (R - h)^2 \ln \frac{R - \delta}{R} - \frac{(R - \delta)^2 - R^2}{2} \right] \quad 55$$

where  $\delta(0, y)$  is the maximum velocity position as known as the dip position.

The dimensionless form of Eq. 55 is obtained by dividing Eq. 54 by Eq. 55 as

$$\frac{\bar{u}_z(r, \theta)}{u_{max}} = \frac{\left( \frac{R - h}{\sin \theta} \right)^2 \ln \frac{r}{R} - \frac{r^2 - R^2}{2}}{(R - h)^2 \ln \frac{R - \delta}{R} - \frac{(R - \delta)^2 - R^2}{2}} \quad 56$$

#### 4.3.2 Variable Eddy Viscosity Model

Eddy viscosity, in essence, is a function of cross-sectional coordinates and the shear velocity for instance it is recommended for rectangular open channel flows to approximate the eddy viscosity with a parabolic function (Yang, Tan, & Lim, 2004; Nezu & Rodi, 1986; Steffler, Rajaratnam, & Peterson, 1985). So far, there is not any variable eddy viscosity model developed for P-FPF. However, it is possible to use an approximation such as the one that Yang et al. 2004 suggested but the problem with such an approach is the complications later involved in the model integration. Research in this field is still in progress and more data and information is needed to develop an analytical variable eddy viscosity which satisfies all related boundary conditions.

---

<sup>7</sup> A minor flow induced by the wall in the non-primary flow direction (Shiono & Knight, 1991).

#### 4.4 Summary

Equation 54 can be used as the final P-FPF analytical model to arrive at the cross-sectional velocity distribution. Later, in Chapter 5 the model will be validated with the experimental data from various sources. Equation 56 is the dimensionless form of Eq. 54 and removes the need for the eddy viscosity. However, in order to use Eq. 56,  $\delta$  should be calculated through the models which later will be introduced in Chapter 6.

## CHAPTER 5: EMPIRICAL SOLUTION TO P-FPF

### 5.1 Boundary Shear Flows

In any fully-developed<sup>8</sup> boundary shear flow, examining  $\bar{u}_z(0,y)$ <sup>9</sup> reveals four distinct layers regardless of the upstream and downstream boundary conditions (Figure 5.1), that is, the viscous sublayer, buffer layer, log-law layer and the outer layer (Guo, Julien, & Meroney, 2005). The first three regions are categorized as the inner region, while the outer layer alone forms the outer region. In the viscous sublayer, because of the low velocity, flow is treated as laminar flow. The transition from laminar flow to the turbulent flow happens in the buffer layer. In the log-law and the outer layer flow is completely turbulent with an increased wake effect<sup>10</sup> in the outer region (Coles, 1956). These layers are depicted in Figure 5.1 in dimensionless units of length and velocity with  $y^+ = \frac{u^*y}{\nu}$  and  $u^+ = \frac{\bar{u}_z(0,y)}{u^*}$  (Nezu & Rodi, 1986). Assuming a constant turbulent shear stress,  $u^*$  is termed shear velocity which is defined through

$$u^* = \sqrt{-\overline{u'_y u'_z}} = \sqrt{\frac{P'_{yz}}{\rho}} \quad 57$$

---

<sup>8</sup> Fully-developed flow term is used when there is not any change in the velocity profile along the primary flow direction. Mathematically, it is equivalent with  $\frac{\partial \bar{u}_z}{\partial z} = 0$  where  $z$  is the primary direction of the flow.

<sup>9</sup> Terminology is based on chapter 4 according to Figure 4.1 and Figure 4.2.

<sup>10</sup> Deviation from the log-law in the outer layer which resembles the separation of flow around blunt objects.

where  $P'_{yz}$  is the turbulent shear stress tensor in  $z$  direction acting on a surface perpendicular to direction  $y$  (Granger, 1995).

## 5.2 Prandtl's Mixing Length Theory (MLT)

Empirical vertical velocity profile was first developed by the aid of Prandtl's Mixing Length Theory (MLT) for smooth pipe flow. Later, it was slightly altered to also account for the rough turbulent pipe flow. Prandtl introduced mixing length analogues to the concept of mean free path in

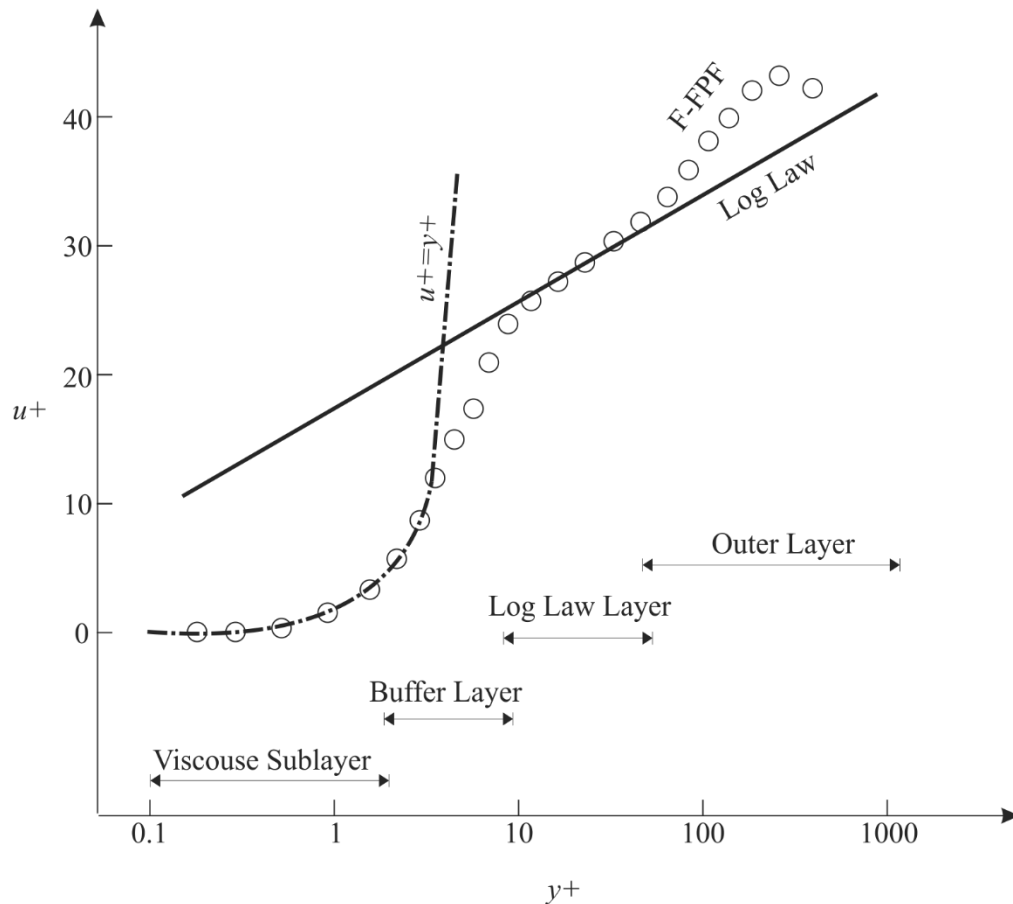


Figure 5.1 Empirical Centerline Velocity Profile in F-FPF



thermodynamics ( $l_m$ ) to model the kinematic eddy viscosity with

$$\nu_t = l_m^2 \left| \frac{\partial \bar{u}_z(0, y)}{\partial y} \right| \quad 58$$

Recalling Boussinesq hypothesis (Eq. 47) and substituting  $\nu_t$  from Eq. 58 results in Eq. 59 (Nikuradse, 1950).

$$-\overline{u'_y u'_z} = l_m^2 \left| \frac{\partial \bar{u}_z(0, y)}{\partial y} \right| \frac{\partial \bar{u}_z(0, y)}{\partial y} \quad 59$$

For boundary shear flows, it is postulated that mixing length could be calculated through Eq. 60 (Escudier & Nicoll, 1966).

$$l_m = \kappa y \quad 60$$

where  $l_m$  is the mixing length and  $\kappa$  is the Von Karman constant found to be 0.41 in pipe flow. Although, later more accurate models<sup>11</sup> were established (Grifoll & Giralt, 2000), Eq. 60 remains handy approximation.

Substituting Eq. 57 and Eq. 60 into Eq. 59 and integrating with respect to  $y$  results in famous log-law, or in other terms the law of the wall (Eq. 61).

$$u^+ = \frac{1}{\kappa} \ln y^+ + A \quad 61$$

Herein,  $A$  is the constant of the integration;  $u^+$  and  $y^+$  are already defined as dimensionless velocity and length, respectively. Following the same procedure, if instead of the Prandtl's eddy viscosity model, Newton's law of viscosity is used i.e.,  $P_{xy} = \mu \frac{\partial \bar{u}_z(0, y)}{\partial y}$ , we will end up with

$$u^+ = y^+ \quad 62$$

---

<sup>11</sup> These models are very complicated and case sensitive.

Initial experimental data validation proved that Eq. 62 held for the viscous sublayer, and Eq. 61 held for the log-law and outer layer (Nezu & Rodi, 1986). However, later it was argued that the model had failed to represent the outer layer accurately but was suggested that it had provided a good approximation for it (Coles, 1956). To resolve the inconsistency of the proposed model and the experimental data in the outer region, Coles (1956) added another term to Eq. 59 naming it the wake function due to the similarities between the outer layer and the Karman vortex street (Eq. 63 and 64).

$$u^+ = \frac{1}{\kappa} \ln y^+ + A + \omega(\xi) \quad 63$$

$$\omega(\xi) = \frac{2\Pi}{\kappa} \sin^2\left(\frac{\pi}{2}\xi\right) \quad 64$$

Here,  $\Pi$  is a fitting parameter known as Coles' wake coefficient and  $\xi = \frac{y}{h}$  (Coles, 1956; Nezu & Rodi, 1986). Equation 63 is called the log-wake (LW) law and has long been in use as a model to predict the velocity in pipe flow, open channel flow and zero pressure gradient flat plates (Guo, Julien, & Meroney, 2005).

### 5.3 Modified log-wake (MLW) law for a turbulent F-PPF

Recent developments in experimental techniques such as Laser Doppler Anemometry (LDA), Acoustic Doppler Velocimetry (ADV) and Particle Image Velocimetry (PIV) have improved the quality of the data acquired in hydraulic labs, enabling scientists to further examine the developed theories. Guo and Julien (2003) proposed Eq. 65 for smooth turbulent pipe flow and Guo (2014) proposed Eq. 66 for rough turbulent pipe flow.

$$\frac{\bar{u}_z(0, y)}{u^*} = \underbrace{\frac{1}{\kappa} \ln \frac{yu^*}{\nu}}_{\text{Log Law}} + A + \underbrace{2 \sin^2\left(\frac{\pi\xi}{2}\right)}_{\text{LW Law}} - \frac{1}{3\kappa} \xi^3 \quad 65$$

MLW Law

$$\frac{\bar{u}_z(0, y)}{u^*} = \underbrace{\frac{1}{\kappa} \ln \frac{y}{y_0}}_{\text{Log Law}} + \underbrace{\frac{2\Pi}{\kappa} \sin^2 \left( \frac{\pi y}{2\delta} \right)}_{\text{LW Law}} - \frac{1}{3\kappa} \left( \frac{y}{\delta} \right)^3 \quad 66$$

MLW Law

Herein,  $y_0$  is the bed roughness height;  $\delta$  is the position of the maximum velocity (known as the dip position) or in mathematical terms we have:

$$\frac{\bar{u}_{max}}{u^*} = \frac{1}{\kappa} \ln \frac{\delta}{y_0} + \frac{2\Pi}{\kappa} - \frac{1}{3\kappa} \quad 67$$

Equations 65 and 66 were termed modified log-wake (MLW) law because of the added terms to the original LW law. Sometime, it is convenient to use the defect<sup>12</sup> form of Eq. 65 and Eq. 66 as:

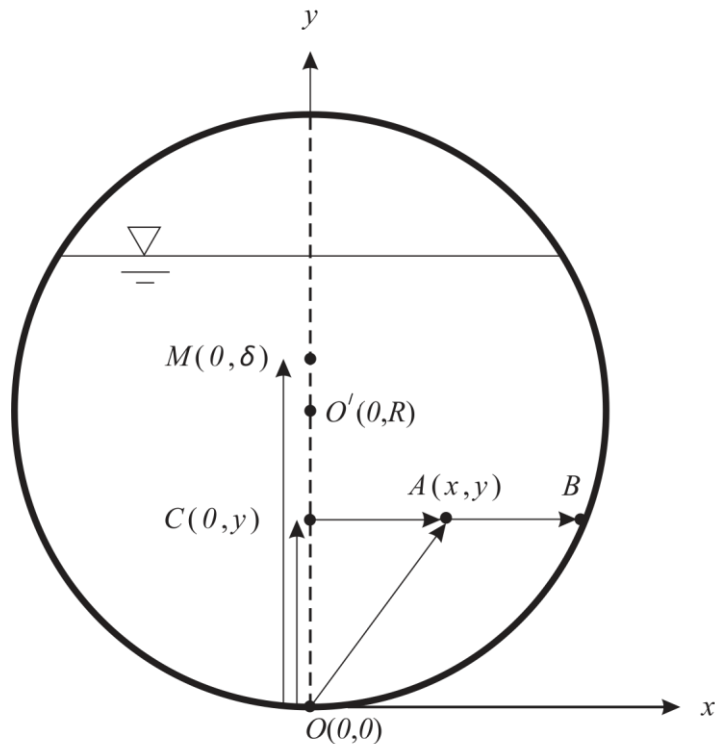


**Figure 5.2 Circular Open Channel Flow Cross-sectional View in Vector Notation**

<sup>12</sup> Removing  $y_0$  in log-wake law with the help of maximum velocity.

$$\frac{\bar{u}_{max} - \bar{u}_z(0, y)}{u^*} = -\frac{1}{\kappa} \left( \ln \xi + \frac{1 - \xi^3}{3} \right) + 2 \cos^2 \left( \frac{\pi \xi}{2} \right) \quad 68$$

$$\frac{\bar{u}_{max} - \bar{u}_z(0, y)}{u^*} = -\frac{1}{\kappa} \left\{ \ln \frac{y}{\delta} - \left[ 1 - \frac{1}{3} \left( \frac{y}{\delta} \right)^3 \right] \right\} + \frac{2\pi}{\kappa} \cos^2 \left( \frac{\pi y}{2\delta} \right) \quad 69$$

## 5.4 Governing Equations

### 5.4.1 Centerline Velocity Distribution

Figure 5.2 depicts a cross-sectional view of a P-FPF with radius  $R$  and flow depth  $h$ . Studying the benchmark culvert velocity distribution data (Clark & Kehler, 2011; Yoon, Sung, & Lee, 2012; Replogle & Chow, 1966; Ead, Rajaratnam, Katopodis, & Ade, 2000; House, Pyles, & White, 2005) qualitatively, it is hypothesized that the solution to the P-FPF should follow that of the F-FPF with

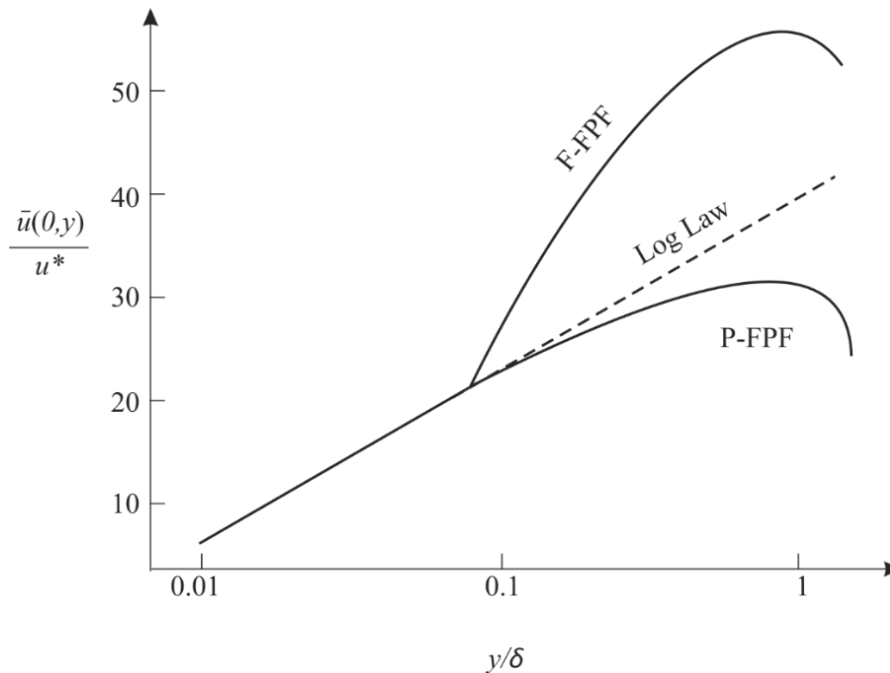


Figure 5.3 Comparison of F-FPF with P-FPF

the exclusion of the wake function. This assumption is due to the monotonic deduction in velocity near the water surface because of the existence of the free surface unlike in F-FPF (Figure 5.3). Therefore, the centerline velocity profile is hypothesized to follow Eq. 70 analogous with Eq. 66 where the pipe wall satisfies Eq. 71 (Figure 5.2).

$$\frac{\bar{u}_z(0, y)}{u^*} = \frac{1}{\kappa} \ln \frac{|\overrightarrow{OC}|}{y_0} - \frac{1}{3\kappa} \left( \frac{|\overrightarrow{OC}|}{|\overrightarrow{OM}|} \right)^3 \quad 70$$

$$x^2 + (y - R)^2 = R^2 \quad 71$$

Herein,  $|\cdot|$  is the norm operator which is given by

$$|\overrightarrow{OC}| = \sqrt{(x_c - x_o)^2 + (y_c - y_o)^2} \quad 72$$

where  $O(0,0)$  is the Cartesian Coordinates origin and  $C(0, y)$  is an arbitrary point on the pipe centerline (Figure 5.2).

Velocity defect form of Eq. 70 follows

$$\frac{u_{max} - \bar{u}_z(0, y)}{u^*} = -\frac{1}{\kappa} \left\{ \ln \frac{|\overrightarrow{OC}|}{|\overrightarrow{OM}|} - \left[ 1 - \frac{1}{3} \left( \frac{|\overrightarrow{OC}|}{|\overrightarrow{OM}|} \right)^3 \right] \right\} \quad 73$$

#### 5.4.2 Cross-Sectional Velocity Distribution Model

The vertical velocity distribution (law of the wall) can be developed for any point in the cross-section regardless of the position of the point which is proved by the earlier studies (Guo, 2014) and also can be validated via the experimental velocity data. In the previous section, the model was developed for point  $C$  with respect to point  $O(0,0)$ . Now, Eq. 70 can be rewritten for an arbitrary point  $A(x, y)$  with respect to point  $B(x_B, y_B)$  through

$$\frac{\bar{u}_z(x, y)}{u^*} = \frac{1}{\kappa} \ln \frac{|\overrightarrow{AB}|}{y_0} - \frac{1}{3\kappa} \left( \frac{|\overrightarrow{AB}|}{|\overrightarrow{CB}|} \right)^3 \quad 74$$

where

$$|\vec{AB}| = \sqrt{(x_B - x_A)^2 + (y_B - y_A)^2} \quad 75$$

and

$$|\vec{CB}| = \sqrt{(x_B - x_C)^2 + (y_B - y_C)^2} \quad 76$$

Substituting Eq. 75 and 76 into Eq. 74 results in:

$$\frac{\bar{u}_z(x, y)}{u^*} = \frac{1}{\kappa} \ln \frac{\sqrt{(x_B - x_A)^2 + (y_B - y_A)^2}}{y_0} - \frac{1}{3\kappa} \left( \frac{\sqrt{(x_B - x_A)^2 + (y_B - y_A)^2}}{\sqrt{(x_B - x_C)^2 + (y_B - y_C)^2}} \right)^3 \quad 77$$

Since point  $B$  is on the boundary,  $x_B$  can be solved in terms of  $y$  with the aid of Eq. 71 as:

$$x_B = \sqrt{y(2R - y)} \quad y_B = y \quad 78$$

Inserting Eq. 78 into Eq. 77 after simplification results in

$$\frac{\bar{u}_z(x, y)}{u^*} = \frac{1}{\kappa} \ln \frac{\sqrt{y(2R - y)} - x}{y_0} - \frac{1}{3\kappa} \left( \frac{\sqrt{y(2R - y)} - x}{\sqrt{y(2R - y)}} \right)^3 \quad 79$$

For point  $C(0, y)$ , Eq. 79 can be rewritten as

$$\frac{\bar{u}_z(0, y)}{u^*} = \frac{1}{\kappa} \ln \frac{\sqrt{y(2R - y)}}{y_0} - \frac{1}{3\kappa} \quad 80$$

Subtracting Eq. 79 from Eq. 80 finally we arrive at

$$\frac{\bar{u}_z(0, y) - \bar{u}_z(x, y)}{u^*} = -\frac{1}{\kappa} \ln \left[ 1 - \frac{x}{\sqrt{y(2R - y)}} \right] + \frac{1}{3\kappa} \left[ \left( 1 - \frac{x}{\sqrt{y(2R - y)}} \right)^3 - 1 \right] \quad 81$$

or instead of Eq. 80, the defect form of

$$\frac{u_{max} - \bar{u}_z(0, y)}{u^*} = -\frac{1}{2\kappa} \ln \frac{y(2R - y)}{\delta(2R - \delta)} \quad 82$$

may be used to replace  $y_0$  with  $\delta$  and  $u_{max}$ . Later in chapter 6 the benefit of such a change of variable will be discussed.

## CHAPTER 6: MODEL VERIFICATION AND DISCUSSION

### 6.1 Analytical Solution of P-FPF

#### 6.1.1 General Remarks

The cross-sectional velocity distribution (Eq. 54) is valid for fully-developed, uniform, steady state and unidirectional flow. Equation 54 satisfies the no-slip i.e.,  $\bar{u}_z(R, \theta) = 0$  as well as the axisymmetric<sup>13</sup> flow boundary condition i.e.,  $\bar{u}_z(r, \theta) = \bar{u}_z(r, \pi - \theta)$ . It also satisfies the zero shear stress of the air-water interface ( $\left. \frac{\partial \bar{u}_z}{\partial r} \right|_{r=\frac{R-h}{\sin \theta}} = 0$ ) that in physical terms means no momentum transfer at the water surface in vertical direction. It has a singularity for  $\theta = 0$  and/or  $\theta = \pi$  when half of the pipe is filled (i.e.,  $h \rightarrow R$ ). The singularity can be removed with the elimination of the logarithmic term that will lead us to the classic quadratic model of Eq. 83 for a half-filled pipe flow

$$\bar{u}_z(r, \theta) = \frac{gS_0}{2(\nu + \nu_t)} \left[ \ln \frac{r}{R} - \frac{r^2 - R^2}{2} \right] \quad 83$$

and in dimensionless form:

$$\frac{\bar{u}_z(r, \theta)}{u_{max}} = \frac{2 \ln \frac{r}{R} - r^2 + R^2}{R^2 - (R - \delta)^2} \quad 84$$

In fish passage design, almost always submerged flow condition is avoided ( $h < R$ ) that is the reason why Eq. 54 was governed for the bottom symmetrical half of the pipe. In order to make it applicable for the top symmetrical half, Eq. 30 should be replaced with Eq. 85 as:

---

<sup>13</sup> Symmetric about the y axis.



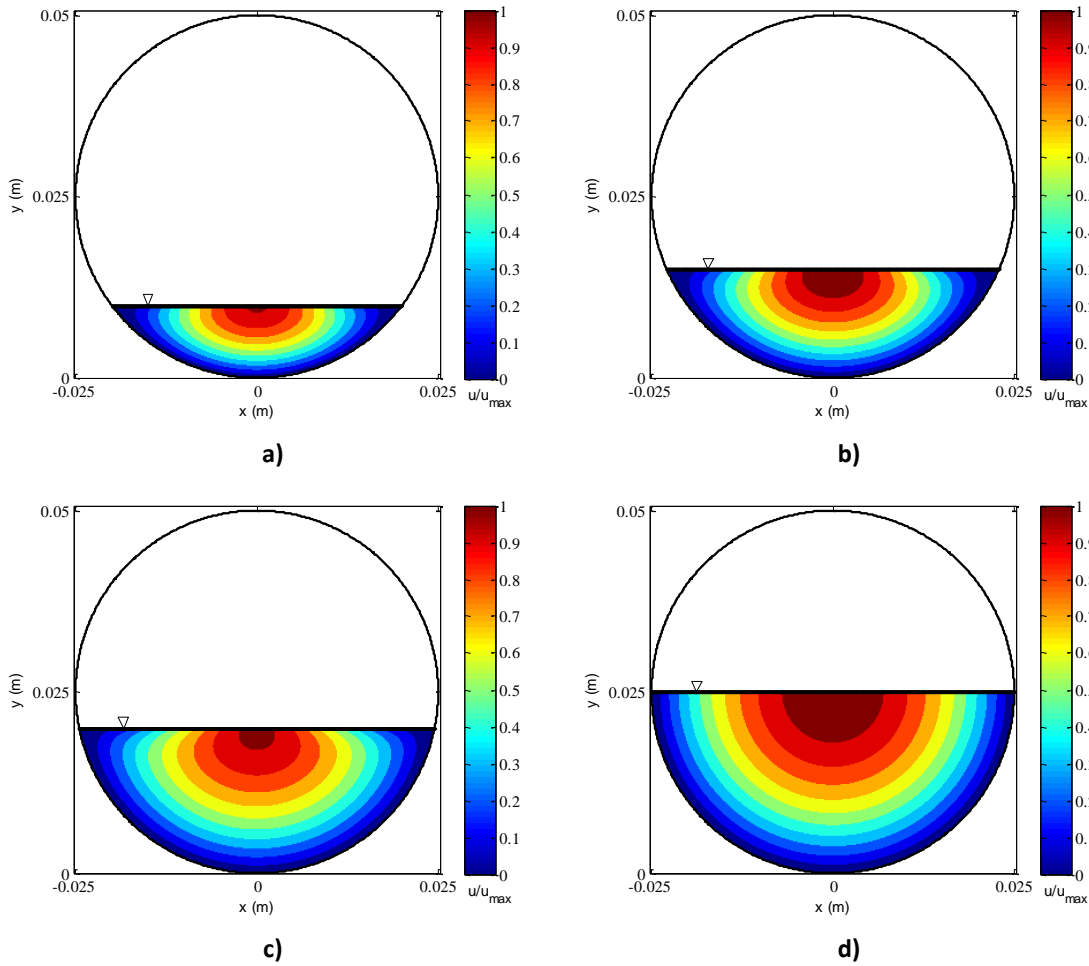


**Figure 6.1 Cross-sectional Velocity Distribution Generated with Eq. 56**

**a)  $h/D=20\%$  b)  $h/D=30\%$  c)  $h/D=40\%$  d)  $h/D=50\%$**

$$y = R + r \sin \theta \quad R < y < 2R$$

85

To further investigate the characteristics of the P-FPF analytical solution, some sample plots were generated using Eq. 56 with the filling ratio ( $h/D$ ) of 20, 30, 40 and 50% (Figure 6.1a-d). With a rise in water level, the maximum velocity position (dip position) moves from  $\delta$  to  $h$  free surface (Figure 6.1a-d) probably due to the increase in the width to depth ratio ( $b/D$ ), where  $b$  is the free surface width. This P-FPF behavior is similar to the case of a wide rectangular open channel flow,

that is, when  $b/h \rightarrow \infty$ , the induced secondary flows are negligible, as a result the dip position will be at the free surface (Bonakdari, Larrarte, Lassabatere, & Joannis, 2008).

### 6.1.2 Cross-sectional Velocity Distribution

To verify the model, a total of six scenarios with the filling ratios of 30%, 40%, and 50% from Yoon et al. (2012) as well as the filling ratios of 44%, 34%, and 50% from Clark and Kehler (2011) were compared with the predicted velocity distribution (Figure 6.2a-f). Note that the right side of Figure 6.2a-b and Figure 6.2d-e were plotted with Eq. 56 while Figure 6.2c and Figure 6.2f were reproduced with Eq. 84. Qualitatively speaking, the velocity distribution agrees well with the experimental results (the right side of each figure is the model prediction and the left side is the corresponding experimental simulation). From a quantitative point of view, it looks like the overall velocity gradients in the model are higher than those of the experimental results. That is, the velocity in the experimental data moving from the zero velocity boundary toward the free surface grows really fast in the viscous layer (20% of the depth) and then stays close to the maximum velocity for the remainder (80% of the depth). Moreover, since there is no turbulence stress effect in the viscous layer, the assumption of a constant eddy viscosity model introduces errors in this region; therefore, this model is not recommended to be used for the viscous region (20% of the depth).

Another concern with the proposed model is the predicted position of the maximum velocity. According to the benchmark experimental results, in a turbulent pipe flow, because of the wall effect and secondary flows, the maximum velocity is usually below the free surface (known as the dip phenomenon). Equation 54 was able to retrieve the position of the dip fairly well with a maximum 21% relative error for the Yoon et al. (2012) data. To improve this further, models that

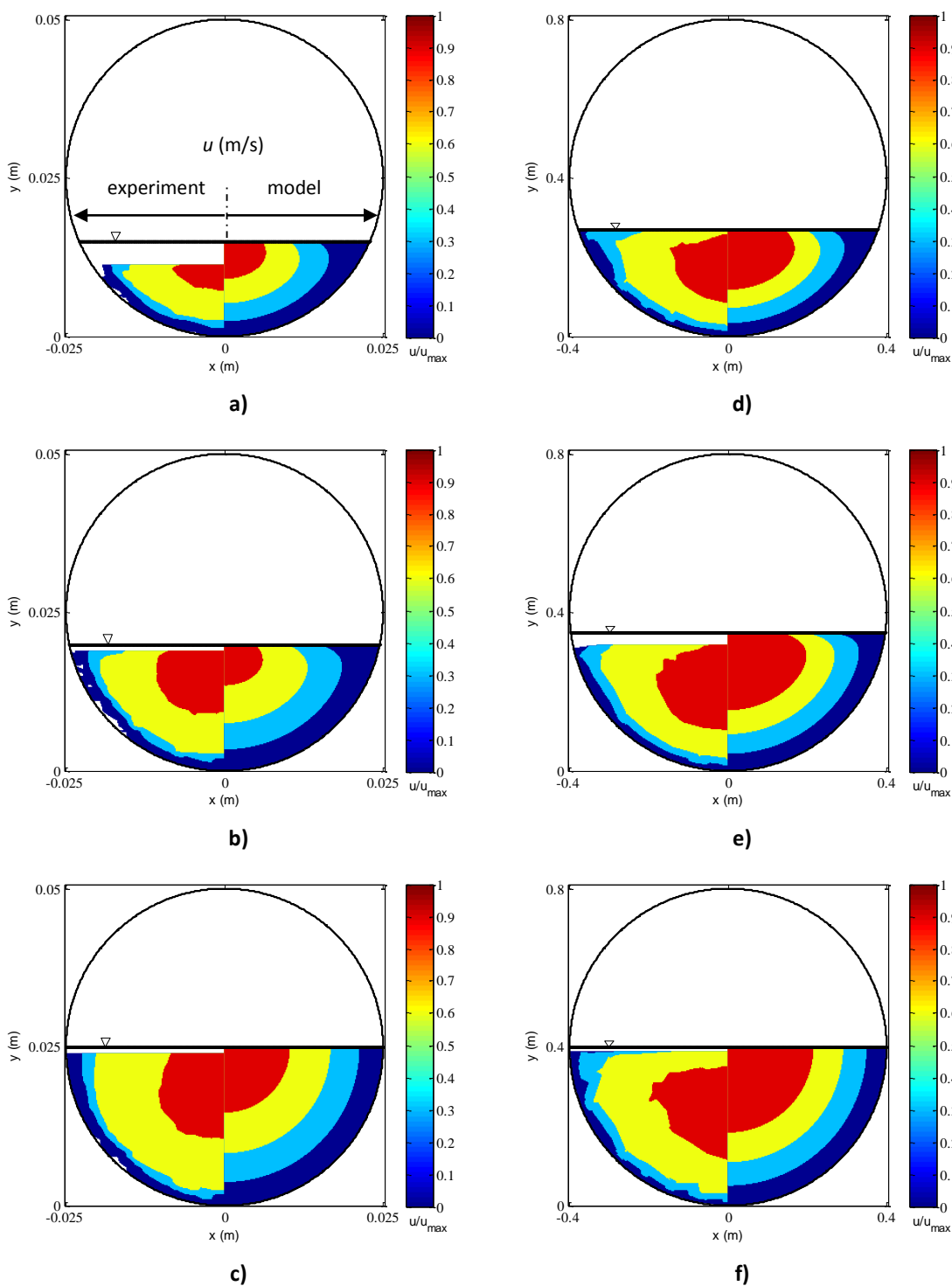


**Figure 6.2 Experimental (left half of cross-section) and Predicted Analytical (right half of cross-section)**

**Cross-sectional Velocity Distribution**

**a) Yoon et al. (2012) Test 1 b) Test 2 c) Test 3**

**d) Clark and Kehler (2011) Test 4 e) Test 2 f) Test 5**

are variable with the aspect ratio of the cross-section (free surface width to the water depth) should be adopted for the eddy viscosity (Bonakdari, Larrarte, Lassabatere, & Joannis, 2008).

Investigation of Figure 6.1 in detail indicates that the isovels start to bend close to the water surface to model the dip phenomenon below the free surface. The shape is completely in agreement with the Yoon et al. (2012) data (Figure 6.2a-c) but diverges from Clark and Kehler (2011) data (Figure 6.2d-f). This discrepancy between the two data sets is believed to be due to the roughness. While Yoon et al. (2012) used a smooth plastic pipe, Clark and Kehler (2011) took advantage of a corrugated metal pipe. Therefore, it is suggested that the analytical model (Eq. 54) is better for the design of smooth culverts rather than rough culverts.

## 6.2 Empirical Solution of P-FPF

### 6.2.1 General Remarks

Centerline velocity (Eq. 80) is embedded inside the developed empirical model of Eq. 81. It is necessary that before investigating the proposed model, the characteristics of the centerline velocity be studied since the accuracy of the centerline velocity has a direct impact on the overall

**Table 6.1 Fitted and Calculated Shear Velocity Comparison**

Data	Test	$u_{fit}^*$ (m/s)	$u^*$ (m/s)	Relative Error	Data	Test	$u_{fit}^*$ (m/s)	$u^*$ (m/s)	Relative Error
Clark and Kehler (2011)	1	0.039	0.037	1%	Yoon et al. (2012)	1	0.022	0.019	1%
	2	0.063	0.061	1%		2	0.033	0.022	2%
	3	0.064	0.075	5%		3	0.027	0.025	1%
	4	0.091	0.085	2%		4	0.030	0.028	1%
	5	0.079	0.0103	30%		5	0.028	0.030	1%
				6		0.026	0.032	2%	

velocity distribution. Equation 80 includes two unknown parameters of  $u^*$  and  $y_0$ , or in defect form, three unknowns of  $u^*$ ,  $\delta$  and  $u_{max}$ . Using the available data sets,  $(u_{fit}^*, y_0)$  and  $(u_{fit}^*, \delta, u_{max})$  were calculated through a non-linear curve-fitting process programmed in MATLAB R2014a. The aim of the non-linear curve-fitting process is to determine the aforementioned unknown parameters in a way that they minimize the residuals of the experimental data from the proposed empirical model.  $y_0$  is the hypothetical zero velocity depth which is related to the bed roughness. Developing a relationship between  $y_0$  and relative roughness of  $\epsilon/D$  as Nikuradse (1950) and Moody (1944) did for the F-FPF needs more data. Since the scope of this material is predictive velocity in culverts rather than investigation of the acquired experimental data, it was decided to analyze  $(u_{fit}^*, \delta, u_{max})$ .

Table 6.1 compares the shear velocity from non-linear curve-fitting and the shear velocity evaluated via (Nezu, 2005) where all the variables are defined in chapter 4. The relative error between the fitted and calculated shear velocity is fairly negligible except for the Clark and Kehler (2011) test 5 where it exceeds an acceptable limit. This is attributed to the difficulties of measuring the flume channel bed slope ( $S_0$ ) because of its small value (-4 order of magnitude).

$$u^* = \sqrt{ghS_0} \quad 86$$

### 6.2.2 Velocity Dip Model

Figure 6.3 plots the dimensionless dip position versus the filling ratio. It should be noted that the Yoon et al. (2012) test 1 with a filling ratio of 30% is omitted from the fitting process as well as from Figure 6.3 because the velocity profile close to the free surface was not measured, and as a result the dip position is not accurate. The reason for not measuring the free surface in case 1 was

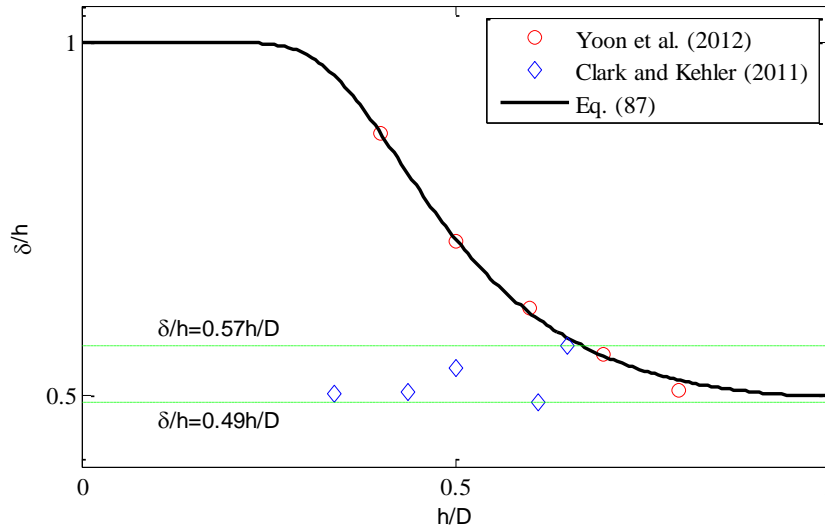


Figure 6.3 Velocity Dip Position Model for Smooth and Rough Pipes

reported as laser illuminations close to the free surface and low flow depth. Velocity dip position for smooth pipes is hypothesized to follow

$$\frac{\delta}{h} = \left\{ 1 + \exp \left[ -\frac{2^n}{\lambda} \left( \frac{D}{h} - 1 \right)^{\frac{n}{2}} \right] \right\}^{-1} \tag{87}$$

where  $\lambda \cong 11$  and  $n \cong 3.4$  are fitting parameters (Guo, 2014). On the other hand, for a rough

Table 6.2 Measure of the Goodness of Empirical Centerline Velocity Model (Eq. 70)

Data	Test	Relative		Data	Test	Relative	
		$R^2$	Error			$R^2$	Error
Clark and Kehler (2011)	1	0.99	1.99%	Yoon et al. (2012)	1	1.00	0.44%
	2	0.99	2.30%		2	0.96	2.73%
	3	0.98	2.15%		3	0.99	0.82%
	4	0.98	2.75%		4	0.99	1.07%
	5	0.99	1.11%		5	0.98	1.11%
					6	0.98	0.99%

pipe the dip position is about half of the flow depth confirmed and recommended by various sources (Clark & Kehler, 2011; Sterling & Knight, 2000). This shows that the dip position for a smooth P-FPF has a rather similar characteristics with that of the rectangular open channel flow unlike to a rough P-FPF (Guo, 2014).

### *6.2.3 Centerline Velocity Distribution*

Figure 6.4a-b and Figure 6.5a-b compare the centerline velocity model of Eq. 70 with Yoon et al. (2012) and Clark and Kehler (2011) data, respectively. The superimposed traditional log law (Eq. 61) on the diagram reveals that the model represents the log law region similar to the conventional open channel flow. The monotonic deduction near the free surface is seen and represented well by the cubic term of Eq. 70. The model is in excellent agreement with the experimental data with the minimum determination coefficient of 0.96 and maximum relative error of 2.75% (Table 6.2).

Figure 6.4a demonstrates a viscous sublayer and a buffer layer for the smooth P-FPF whereas these disappear in the rough P-FPF (Figure 6.5a) because of the roughness effect and increased near-bed turbulence. It is worth mentioning that the viscous layer data were used neither in fitting process nor in determination coefficient and relative error assessment of Table 6.2. Moreover, the viscous layer in Figure 6.4a is diminished with the increase of the flow depth.

### *6.2.4 Cross-sectional Velocity Distribution*

Figure 6.6a-f and Figure 6.7a-e depict the comparison between the predicted model (right) and the corresponding experimental data (left). As mentioned earlier, the goodness of the centerline velocity model has direct impact on the goodness of the cross-sectional velocity model. This is

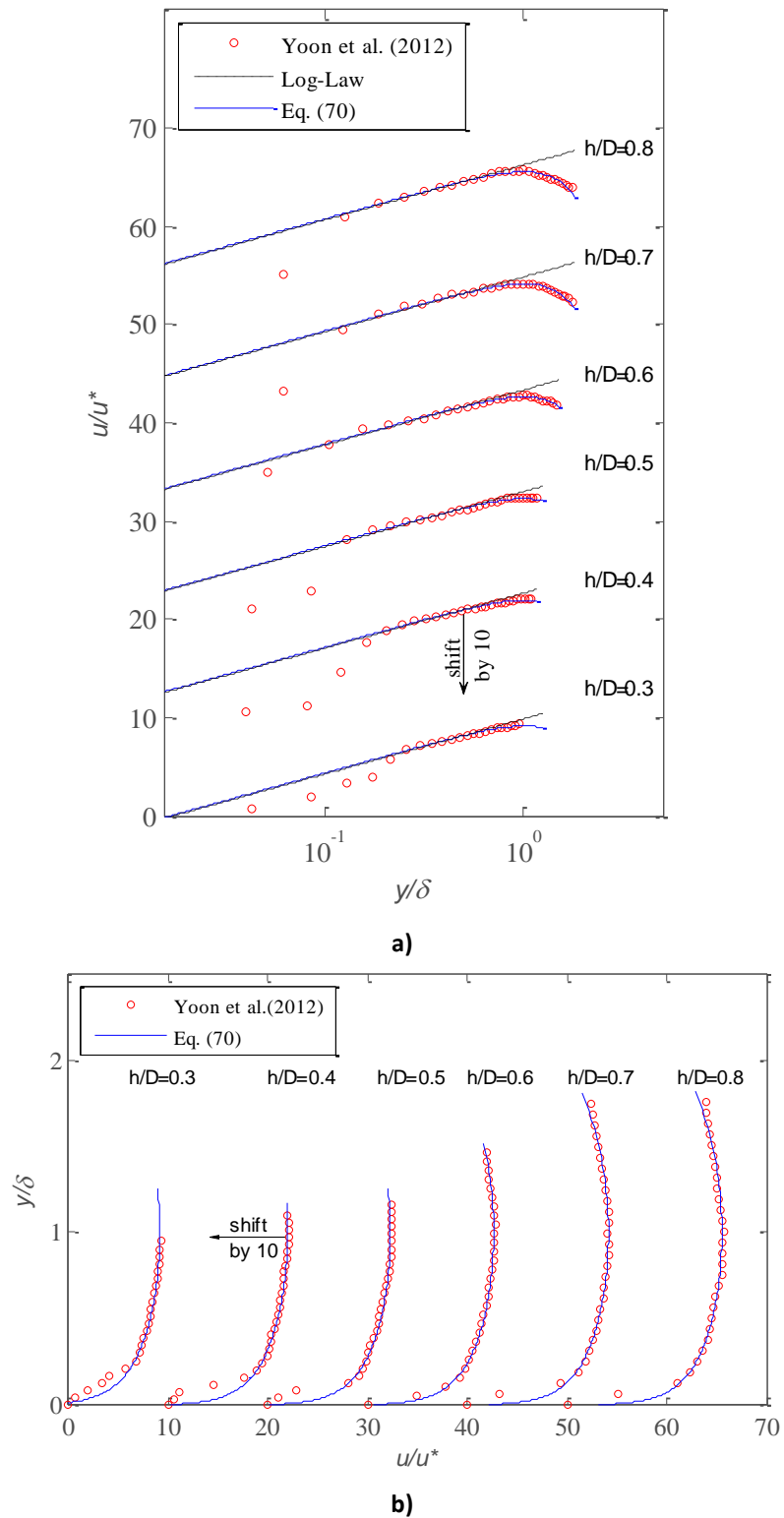


Figure 6.4 Comparison of Eq. 70 with Yoon et al. (2012) Centerline Velocity Profile

a) Logarithmic b) Ordinate



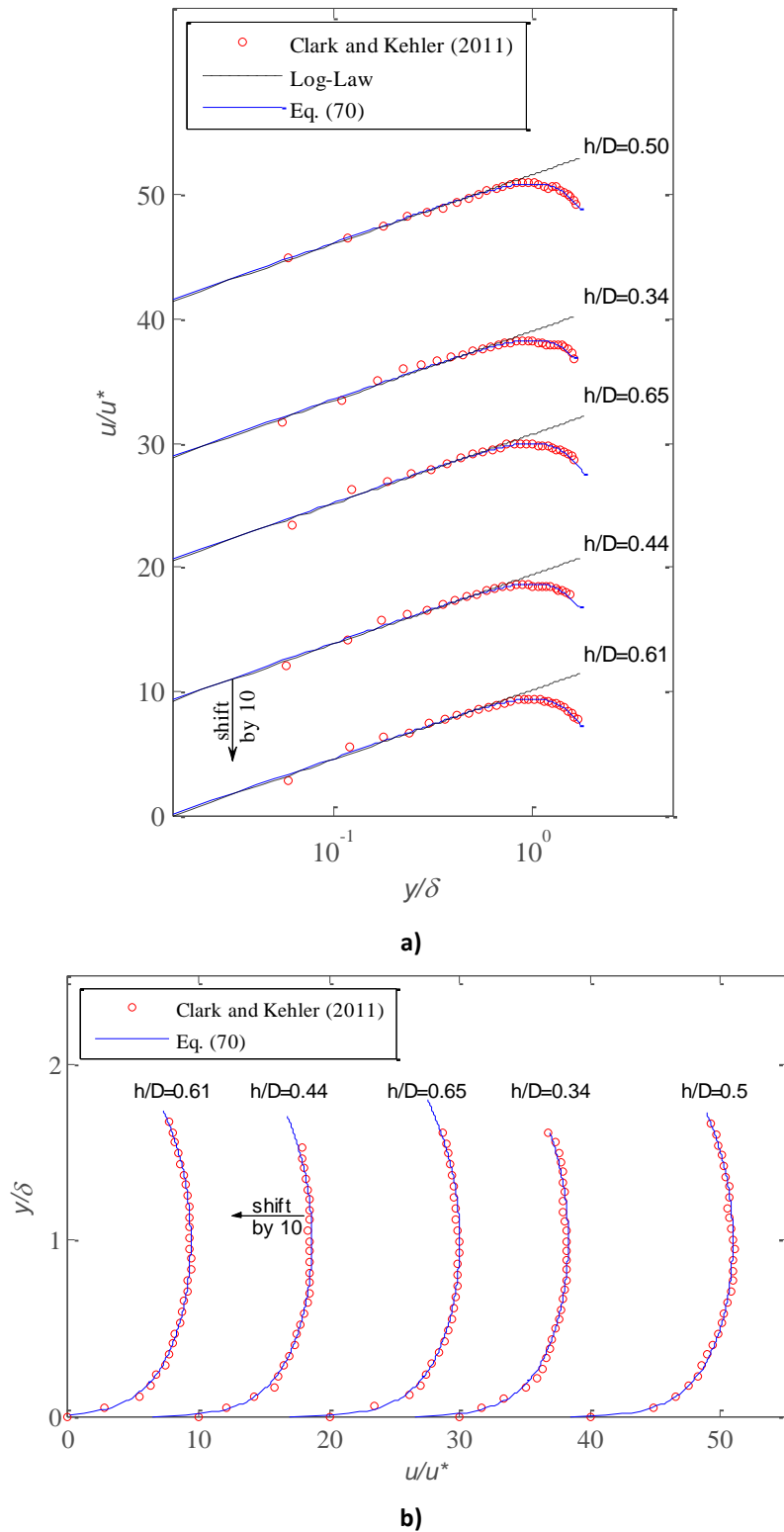


Figure 6.5 Comparison of Eq. 70 with Clark and Kehler (2011) Centerline Velocity Profile

a) Logarithmic b) Ordinate

**Table 6.3 Measured Experimental and Fitted Maximum Velocity Comparison**

Data	Test	$u_{\max}^*$ (m/s)	$u_{\max}^{**}$ (m/s)	Relative Error	Data	Test	$u_{\max}$ (m/s)	$u_{\max}$ (m/s)	Relative Error
Clark and Kehler (2011)	1	0.36	0.36	0.60%	Yoon et al. (2012)	1	0.24	0.24	0.91%
	2	0.54	0.55	1.44%		2	0.32	0.32	1.27%
	3	0.64	0.64	0.58%		3	0.36	0.36	0.22%
	4	0.75	0.76	1.44%		4	0.39	0.38	2.55%
	5	0.87	0.86	1.15%		5	0.41	0.40	2.26%
				6		0.41	0.40	2.84%	

\* Measured experimental maximum velocity extracted from data.

\*\* Fitted maximum velocity.

well visualized in Figure 6.6a-c where due to the limitations of the model in modeling the viscose layer (Figure 6.4a), the velocity magnitude close to the bed is slightly overestimated. In addition, since the viscose layer disappears with the increase of the flow depth, the overall performance of the model is improved (Figure 6.6d-f).

The maximum relative error between the maximum cross-sectional velocities measured in the experiment with the fitted maximum velocity is 2.84% (Table 6.3). Ideally, the maximum velocity should appear on the culvert centerline because of the symmetrical geometry, but this is not the case in practical applications. In practice, it is very difficult to install the culvert with no slope in the transverse direction. Plus, if the culvert is helically corrugated, the maximum velocity will be shifted away from the centerline as a result of the induced flow from the corrugation. The proposed model is applicable even when we are dealing with non-axisymmetric cases.

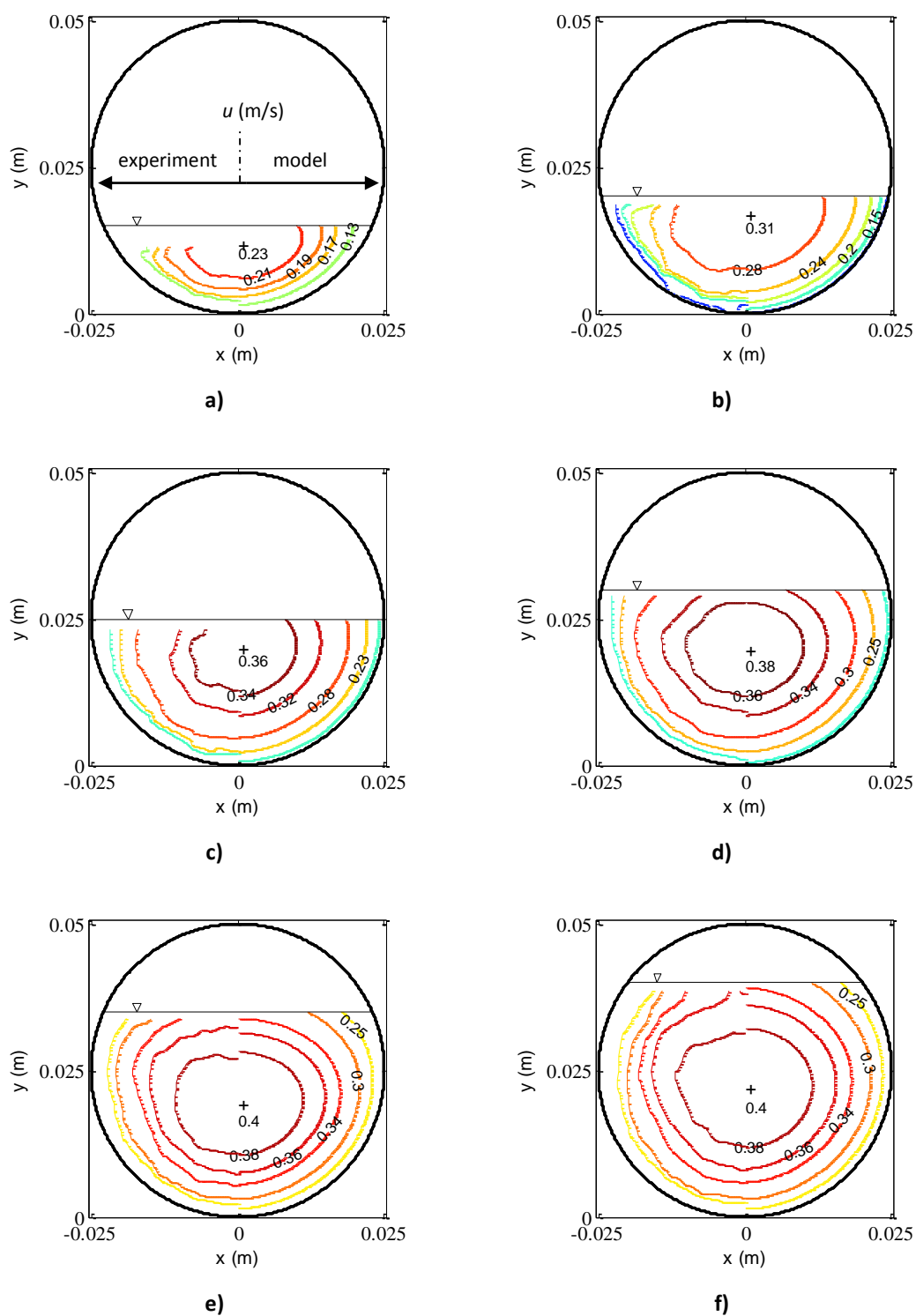


**Figure 6.6 Experimental (left half of cross-section) and Predicted Empirical (right half of cross-section) Cross-sectional Velocity Isovels**

a) Yoon et al. (2012) Test 1 b) Test 2 c) Test 3 d) Test 4 e) Test 5 f) Test 6

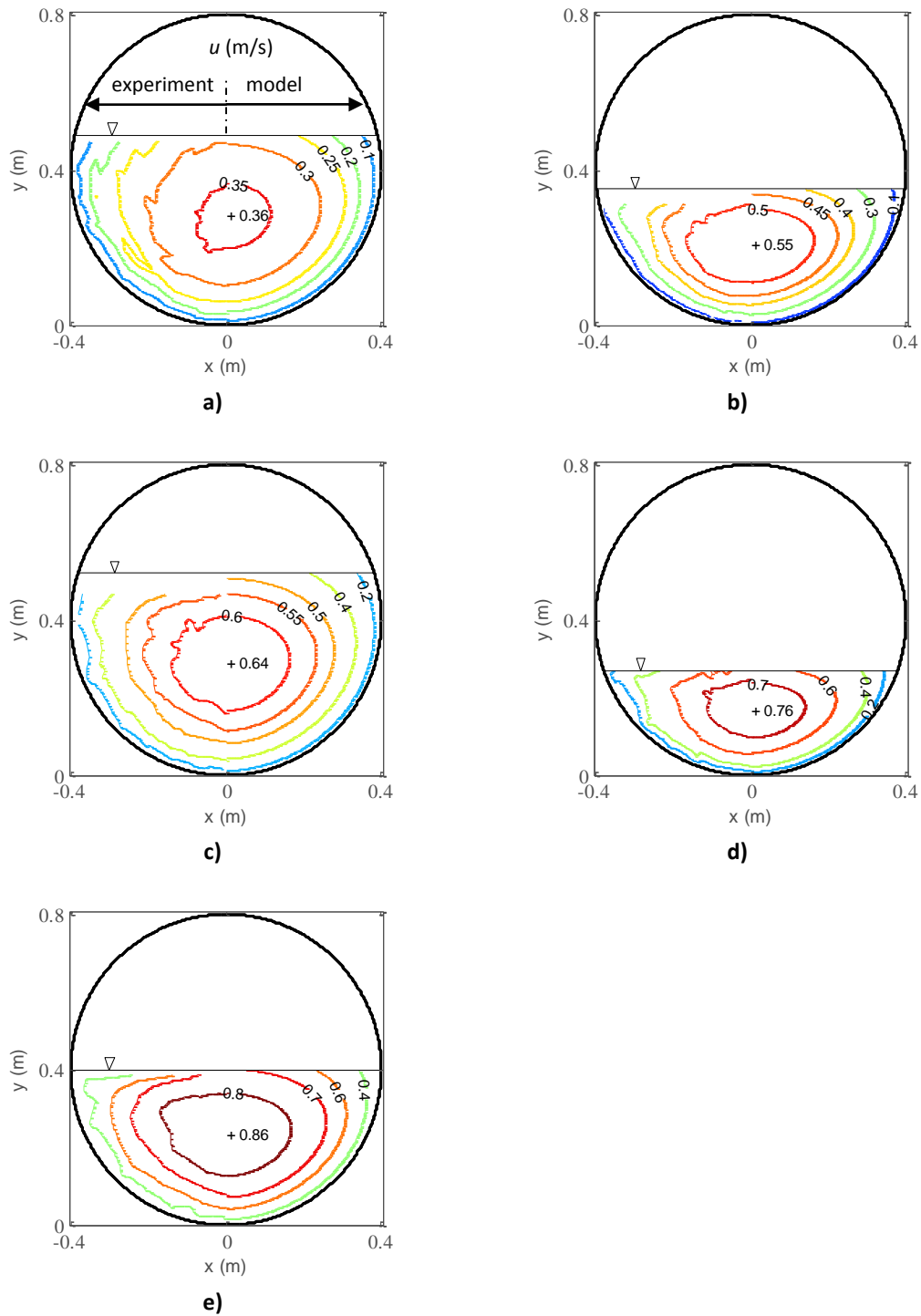


**Figure 6.7 Experimental (left half of cross-section) and Predicted Emperical (right half of cross-section)**

**Cross-sectional Velocity Isovels**

**a) Clark and Kehler (2011) Test 1 b) Test 2 c) Test 3 d) Test 4 e) Test 5**

### 6.2.5 Roughness Effect

The empirical model of Eq. 81 is used to simulate the velocity contours for the embedded culverts e.g., culverts with flat beds. This feature of the model is of a great importance not only in embedded fish passage and culvert design but also in reassessment of old culverts. After severe weather conditions such as flooding, the serviceability of the culverts should be investigated. The general desire for culvert restoration (an expensive and time consuming operation) is to prevent mass fish deaths specially in spawning season. What can be done in the meantime is to reassess the clogged culvert with the proposed empirical model taking into account the present obstacles to see if the culvert is still able to maintain its initial performance.

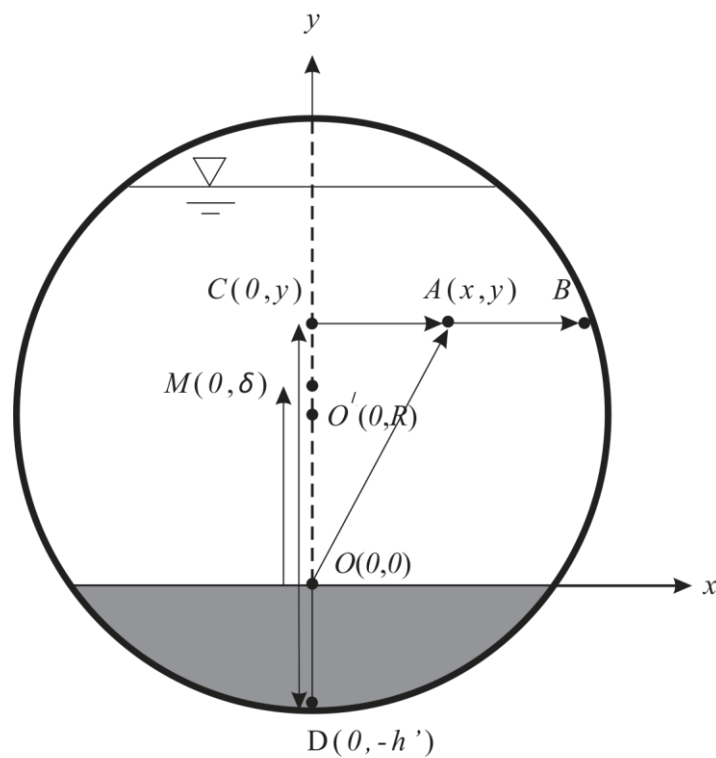


**Figure 6.8 Circular Open Channel Flow Cross-sectional View with Roughness**

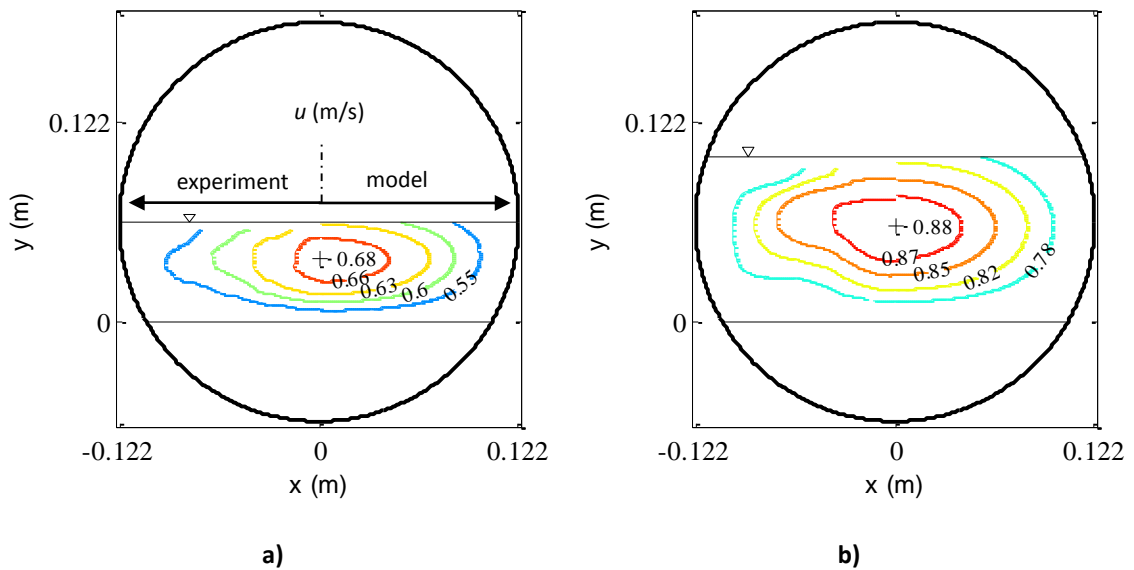


**Figure 6.9 Experimental (left half of cross-section) and Predicted Empirical (right half of cross-section)**

**Cross-sectional Velocity Isovles**

**Knight and Sterling (2000) a) Test 1 b) Test 2**

In order to utilize Eq. 81 for this purpose, a change in the origin of the Cartesian coordinate system is required (Figure 6.8) and that is to shift the origin along the pipe centerline by roughness depth ( $h'$ ). All other variables such as  $h, \delta, O'$  and so on should be adjusted according to the new coordinate system.

Figure 6.9a-b compares the experimental data (Knight & Sterling, 2000; Sterling & Knight, 2000) and the empirical model of Eq. 81. Visual inspection reveals that the velocity contours in the cases with roughness are more flat and resemble the traditional rectangular open channel flow case. To predict the dip position, this case should be treated as a rough P-FPF in which the dip is proved to be halfway between the bed and the free surface.

## CHAPTER 7: APPLICATIONS OF P-FPF IN DESIGN

This chapter discusses applications of the introduced P-FPF models in design. Simplified, yet practical and systematic procedures will be offered for sewer and fish passage design and may be utilized by consulting firms, state agencies, and/or academic institutes. Sewer design is not as sensitive as fish passage design, and therefore, only the easy to use the analytical model will be considered. On the other hand, in fish passage design, local velocities play an important role on fish biology, and care must be taken in design. Hence, two methods, namely a simplified and a comprehensive method will be presented. Wherever the mathematical manipulation of the models is complicated, numerical integration with the help of MatLab 2014 *integral2.m* or Maple 16 *evalf* algorithms will be utilized to advance the calculation. In this chapter, some values will be presented in the U.S. Customary system of units because they are extracted from U.S. design manuals.

### 7.1 Sewer Design

In hydraulics of sewers, it is important to calculate the basic hydraulic parameters of the P-FPF to develop a design curve known as a stage-discharge diagram. Non-dimensionalized wetted area, wetted perimeter, and hydraulic radius are calculated with the aid of trigonometry as

$$\frac{A_w}{A_{w50}} = 1 - \frac{2\theta_1}{\pi} - \frac{\sin 2\theta_1}{\pi} \quad 88$$

$$\frac{P_w}{P_{w50}} = \left(1 - \frac{2\theta_1}{\pi}\right) \quad 89$$

, and

$$\frac{R_h}{R_{h50}} = 1 - \frac{\sin 2\theta_1}{\pi - 2\theta_1} \quad 90$$

where subscript 50 denotes a filling ratio of 0.5;  $\theta_1$  is the free surface angle in radians defined as

$$\theta_1 = \arcsin \frac{R - h}{R} \quad 91$$

Flow rate is calculated through the integration of the velocity distribution over the wetted cross-section as

$$\frac{Q}{Q_{50}} = \frac{2 \int_{\theta_1}^{\frac{\pi}{2}} \int_{\frac{R-h}{\sin \theta}}^R u_z(r, \theta) dr d\theta}{2 \int_0^{\frac{\pi}{2}} \int_0^R u_z(r, \theta) dr d\theta} \quad 92$$

Here, the analytical velocity model of Eq. 54 is used.  $r$  and  $\theta$  are defined according to Figure 4.2.

Dimensionless average velocity is obtained with a similar procedure through

$$\frac{U}{U_{50}} = \frac{2 \int_{\theta_1}^{\frac{\pi}{2}} \int_{\frac{R-h}{\sin \theta}}^R u_z(r, \theta) dr d\theta}{2 \left(1 - \frac{2\theta_1}{\pi} - \frac{\sin 2\theta_1}{\pi}\right) \int_0^{\frac{\pi}{2}} \int_0^R u_z(r, \theta) dr d\theta} \quad 93$$

Equation 92 and 93 are solved using Maple 16, and the results are presented on Figure 7.1 along with plots of Eqs. 88-90. Figure 7.1 is important because it gives all the essential parameters with respect to each other.

## 7.2 Fish Passage Design

### 7.2.1 Simplified Method

Fish passage (Figure 7.2a) design is similar to the sewer design with some special considerations. Fish are sensitive to the flow velocity, flow turbulence intensity, flow depth, and culvert inlet/outlet hydraulic condition (Figure 7.2b). Satisfying only hydraulic constraints in fish passage



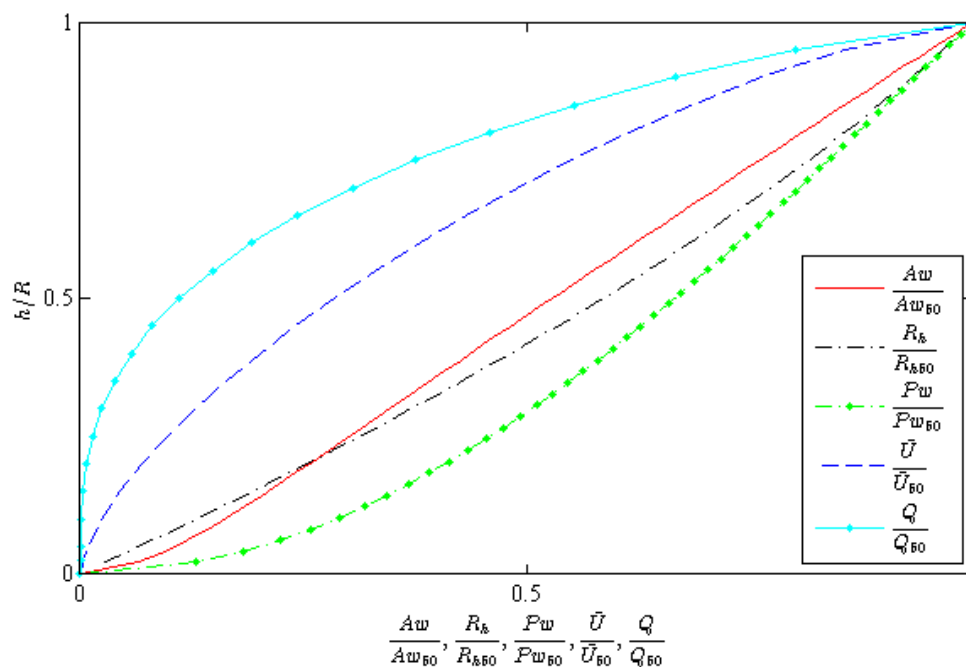


**Figure 7.1 P-FPF Hydraulic Elements**

design or in other words treating fish passage as a normal culvert may result in fish migration blockage. Investigations should be carried out on the territory where the fish passage will be located, on types of the fish, average fish swimming capability, average river/creek discharge and other biological and hydraulic elements. The most important biological parameter is the fish design velocity ( $U_d$ ) defined as the velocity at which fish can swim for a long period of time without exhaustion. All this information is readily available if we have identified the fish species

**Table 7.1 State of Maryland General Design Requirements for Fish Passage (Zhai, 2012)**

Fish Specie	Flow Velocity (ft/s)	Minimum Flow Depth (in)
Non-trout	1.5	4-6
Trout	3	12



**Figure 7.2 Fish Passage**

**a) Near Crooked Lake (photo courtesy of NRCS) b) Migrating Salmon through culvert on Meadow Creek in Matanuska-Susitna Valley (photo courtesy of U.S. Fish and Wildlife Service)**

which reside in the territory of interest. For example, the design manual of Maryland, assumes up to 1 foot per second fish design velocity for non-trout and up to 3 feet per second for trout streams (Table 7.1). The California Department of Fish and Game assumes up to 1 foot per second for juvenile Salmonid streams (Table 7.2).

**Table 7.2 State of California General Design Requirements for Fish Passage (Bates, 2002)**

	<b>Flow Velocity (ft/s)</b>	<b>Minimum Flow Depth (ft)</b>
Adult Anadromous Salmonids	2-6	1.00
Adult Non-Anadromous Salmonids	2-4	0.67
Juvenile Salmonids	1	0.50
Native Non-Salmonids	Specific Data Needed See (Bates, 2002)	
Non-Native Species		

The next step is to prepare a local depth-averaged velocity (Zhai, 2012) for arbitrary filling ratios recommended not to exceed 60% according to different state agency regulations. The filling ratio is the designer's decision and should be chosen according to yearly rainfall-runoff, design discharge, and fish height (defined later). Nevertheless, filling ratios from 30 to 60% for a culvert of at least 3 feet diameter are desirable (Kilgore, Bergendahl, & Hotchkiss, 2010).

Figure 7.3 depicts depth-averaged velocity for an arbitrary culvert of diameter 2.62 feet with filling ratios of 34, 44, and 50% and a fish design velocity of 1 foot per second. Comparing the cases with filling ratios of 34 and 44% reveals that, for the same design discharge, with the increase of the filling ratio the depth-averaged velocity shows reduction in the center of the culvert, and almost no change close to the sides (Figure 7.3). These suggest that if specific design discharges are to be reached, one of the ways to reduce the velocity to the fish swimming velocity level is to raise the flow depth.

The next step is to plot a vertical line which corresponds to  $u/U_d = 1$ , and that is the boundary fish can swim with its regular speed without utilizing the burst velocity. This is termed as the maximum velocity boundary and is plotted with a dashed line on Figure 7.4. Left and right bank flow depth are shallower compared to the center of the culvert. A sufficient flow depth is needed for fish to swim and survive. The horizontal coordinate which corresponds to the minimum depth needed for fish to traverse the passage safely is calculated through

$$\frac{x_d}{D} = \frac{\sqrt{(h - h_d)(2R - h + h_d)}}{D} \quad 94$$

where  $h_d$  is fish height (Figure 7.5) and  $x_d$  serves as the minimum depth boundary.

It should be noted that often the minimum flow depth for fish passage design is larger than that

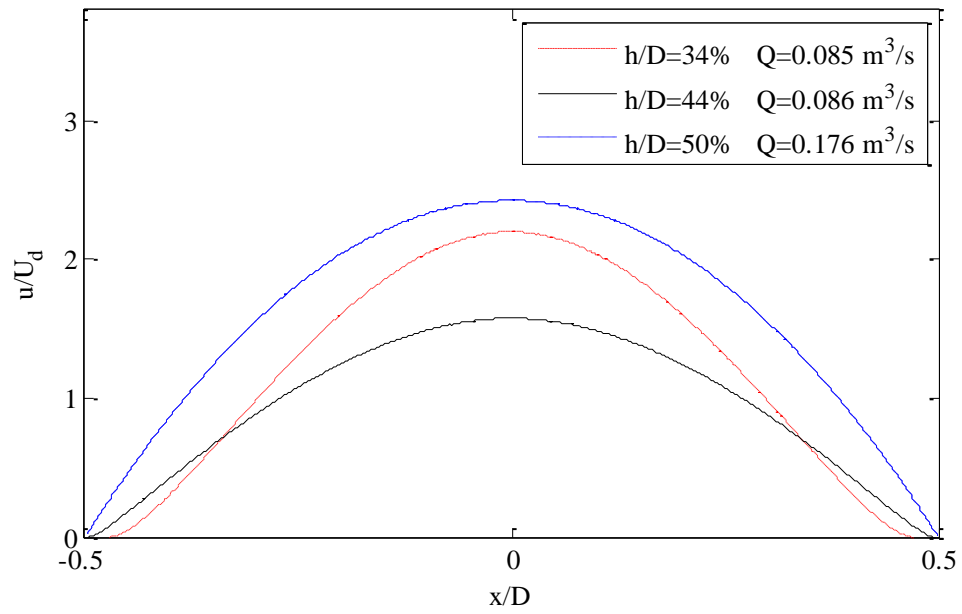


Figure 7.3 Depth-Averaged Velocity for Different Flow Depths

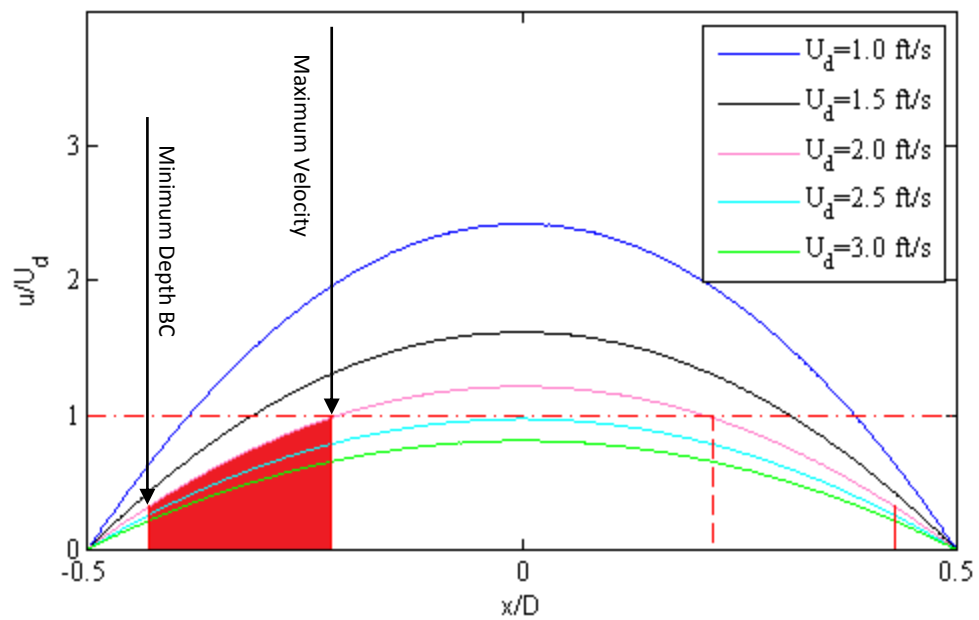
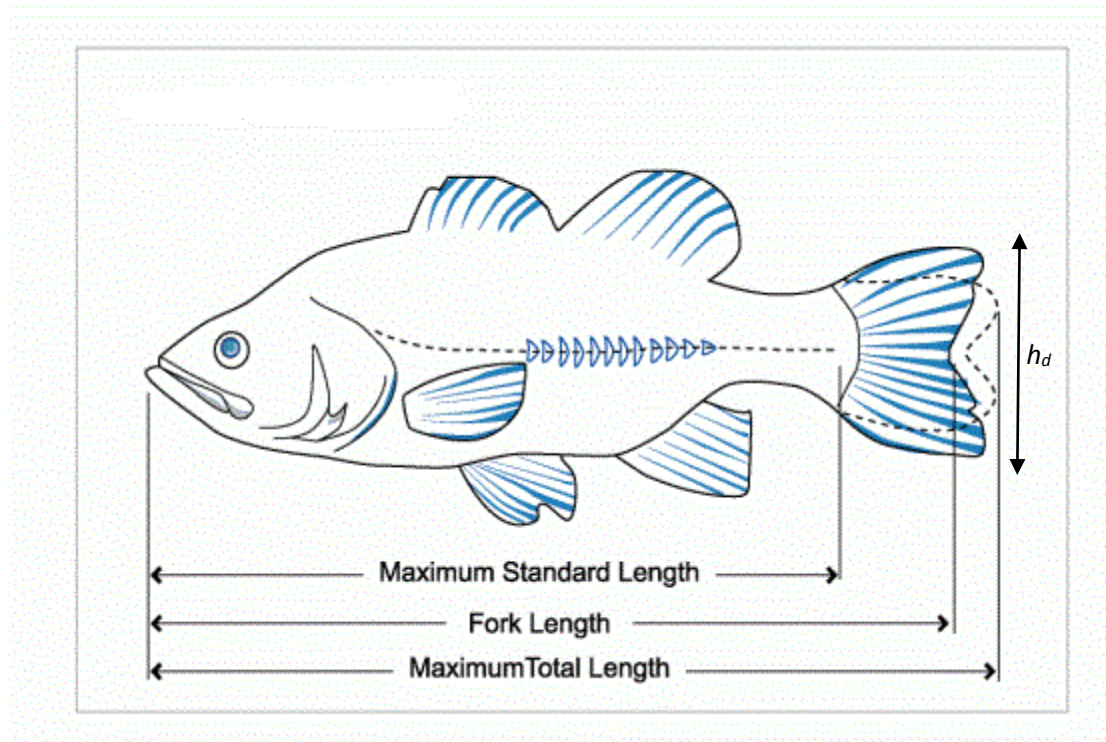


Figure 7.4 Design Curve for Fish Passage with Different Fish Design Velocity



**Figure 7.5 Fish Sizing (courtesy of Australian Government Department of the Environmental)**

of the fish height due to safety. The minimum width is plotted with a solid line on Figure 7.4 which represents a lower limit of the area fish will use to pass. Finally, the area encompassed by two red lines and the dimensionless depth-averaged velocity curve on both sides of the culvert is the fish utilized area to pass the culvert. An optimal design is a design with minimum culvert cross-section accommodating the design discharge while supplying the fish enough low velocity region to complete its migration successfully. As an example, Figure 7.4 shows a hypothetical design curve for a stream with adult non-Anadromous Salmonids with fish design velocity of 2 feet per second and minimum 0.67 feet of height for a culvert of 2.62 feet in diameter and design discharge of 0.176 cubic meter per second. Further, the filling ratio is chosen to be 50% for this case.

Some design curves i.e.,  $U_d = 2.5$  and  $3$  ft/s on Figure 7.4 are below the line of  $u/U_d = 1$ . This means if the fish passage was to be designed for a fish design velocity of 2.5-3 feet per second or larger, the whole wetted cross-section of the culvert could be used by fish to pass.

### 7.2.2 Comprehensive Method

Considering the empirical approach discussed in this study, a robust and powerful fish passage design method is offered in this section. The empirical Eq. 81 is denoted as

$$\frac{\bar{u}_z(0, y) - \bar{u}_z(x, y)}{u^*} = -\frac{1}{\kappa} \ln \left[ 1 - \frac{x}{\sqrt{y(2R - y)}} \right] + \frac{1}{3\kappa} \left[ \left( 1 - \frac{x}{\sqrt{y(2R - y)}} \right)^3 - 1 \right] \quad 95$$

where

$$\frac{\bar{u}_z(0, y)}{u^*} = \frac{1}{\kappa} \ln \frac{\sqrt{y(2R - y)}}{y_0} - \frac{1}{3\kappa} \quad 96$$

Equation 95 and 96 come with two unknown variables of  $u^*$  and  $y_0$ . According to chapter 6 model verification,  $u^*$  can be calculated via (Nezu, 2005)

$$u^* = \sqrt{ghS_0} \quad 97$$

with maximum 5% of error. Moreover,  $y_0$  can be calculated by

$$y_0 = \frac{\nu}{9u^*} + \frac{k_s}{30} \left[ 1 - \exp \left( -\frac{k_s u^*}{26\nu} \right) \right] \quad 98$$

(Guo & Julien, 2007) where  $k_s$  is the uniform sand-grain roughness pattern. For other roughness patterns,  $k_s$  is calculated using Manning coefficient with

$$n \cong 0.0342k_s^{1/6} \quad 99$$

(Chow, 1959).

### 7.2.2.1 Step-by-Step Design Procedure

The following procedure is recommended for fish passage design:

1. The territory of interest for fish passage design should be investigated for hydrologic ( $Q$ ), geographic ( $S_0$ ), and biological ( $U_d$ ) information.
2. The designer should assume an initial culvert size ( $D$ ), filling ratio ( $h/D$ ), and roughness height ( $h_d$ ) based on his/her own experience and available products in the market.
3. Shear velocity is calculated using Eq. 97, and subsequently velocity distribution will be calculated using Eq. 95 and 96.
4. The fish design velocity ( $U_d$ ) is superimposed on the velocity contours.
5. Choose appropriate minimum fish height from design manuals according to the fish species living in the river.
6. Check the velocity distribution contours for fish utilized trajectory which are contours with velocity smaller than fish design velocity. If there are not sufficient low velocity regions, repeat the procedure from step 2 changing pipe diameter, filling ratio or roughness height.

## CHAPTER 8: CONCLUSIONS

### 8.1 Summary and Conclusions

The S-PIV method was explained in detail along with the writer's experimental results. The RANS equations were solved to arrive at an analytical approximation of a partially-filled pipe flow in both smooth and corrugated pipes. An empirical model based on the modified log-wake law was presented based on the previous knowledge of the rectangular open channel flow. The analytical and the empirical models were evaluated using data from various sources (Clark & Kehler, 2011; Yoon, Sung, & Lee, 2012; Mohebbi, Zhai, & Kerenyi, 2010; Replogle & Chow, 1966). Step-by-step sewer and fish passage design methods were presented in terms of depth-averaged velocity and local velocities adjusted for fish swimming capability.

Following conclusions can be drawn:

- The S-PIV method is proved to be one of the powerful methods which resulted in a whole flow field velocity distribution, a significant improvement over previous work. The only drawback is the huge amount of time and energy used to calibrate the cameras and the laser. Also, working with the laser and CCD cameras needs extra care due to their huge cost and taking safety precautions.
- It was found that the eddy viscosity is a function of the geometry as well as the flow condition. The use of a constant eddy viscosity model provided a close approximation of the measured velocity distribution in the cross-section. Although, acceptable agreement was achieved, the model is recommended to be used in the case of a rough surface such



as CMPs rather than smooth pipe. Fortunately, smooth pipes are seldom used as culverts or fish passages.

- The empirical model showed a nearly perfect agreement with the experimental data provided that the shear velocity is adjusted with the log-law region data. Subsequently, it was shown that the shear velocity, roughness length and dip position could be calculated successfully with the proposed models, giving the empirical approach the ability of the velocity prediction without any need for fitting parameters.
- It is recommended to use the analytical model for design of the non-fish passage structures such as sewers and road crossings because the proposed model is simple and straight forward, and the slight inconsistencies with the experimental data close to the bed could be ignored. However, for fish passage design, the empirical model together with the dip, shear velocity, and roughness models showed to be used to adjust the cross-section according to the organism's biological characteristics.

## 8.2 Future Work

Arising from this work, several lines of research should be followed in the future, which either will improve this work or lead to new findings, and they are discussed below:

- Due to the complications involved in the integration of the analytical model, eddy viscosity was assumed to be constant. Previous measurements of the eddy viscosity in open channel flow propose a parabolic distribution of the eddy viscosity (Nezu & Rodi, 1986; Steffler, Rajaratnam, & Peterson, 1985; Yang, Tan, & Lim, 2004) for the center line velocity. Adopting a previously developed or developing a new eddy viscosity model may improve the quality of the proposed analytical model especially close to the wall.

- Preliminary tests on the empirical approach showed that this model may be used for other conic sections such as parabola, hyperbola, and ellipse. Unfortunately, there is not any benchmark data related to any conic sections except circle, and that is why they were not given further considerations in this research. PIV or ADV experiments should be conducted on other conic sections to verify the proposed empirical models. Especially, these tests should be conducted on parabola which is a close approximation of a trapezoidal channel after sediment deposition and/or on ellipse which is the deformed shape of a circular channel under soil pressure.
- The design method discussed needs three types of data namely hydrologic, geologic, and biological data. Hydrologic and geologic data should be collected locally or Geographic Information System (GIS) may be used. For the biological data, there are design manuals customized for each state in the US. A comprehensive encyclopedia of biological information related to all fish species could be a good addition to this research.

## REFERENCES

- Abbs, T. J., Kells, J. A., & Katopodis, C. (2007). A model study of the hydraulics related to fish passage through backwatered culverts. *18th Canadian Hydrotechnical Conference Challenges for Water Resources Engineering in a Changing World*. Winnipeg, Manitoba, August 22-24: Canadian Society of Civil Engineers.
- Adrian, R. J. (1991). Particle-imaging techniques for experimental fluid mechanics. *Annual Review of Fluid Mechanics*, 23, 261-304.
- Adrian, R. J. (2009). *Bibliography of particle image velocimetry using imaging methods: 1917 to 1995*. TAM Report 817: University of Illinois.
- Adrian, R. J., & Westerweel, J. (2011). *Particle Image Velocimetry*. New York: Cambridge University Press.
- Arroyo, M. P., & Greated, C. A. (1991). Stereoscopic particle image velocimetry. *Measurement Science and Technology*, 2(12), 1181-1186.
- Azevedo, H. S., Morales, R. E., Franco, A. T., Junqueira, S. L., & Erthal, R. H. (2008). Numerical simulation of turbulent flow in corrugated pipes. *12th Brazilian Congress of Thermal Engineering and Sciences*. Belo Horizonte, MG, Brazil, November 10-14 : Proceedings of ENCIT.
- Bates, K. (1999). *A design manual for fish passage at road crossings*. Olympia, WA: Washington Department of Fish and Wildlife.

- Bates, K. (2002). *Culvert criteria for fish passage*. Department of Fish and Game. State of California Resources Agency.
- Behlke, C. E., Kane, D. L., McLean, R. F., & Travis, M. D. (1991). *Fundamentals of culvert design for fish passage of weak-swimming fish*. Fairbanks, AK: U.S. Department of Transportation and Public Facilities .
- Berlamont, J. E., Trouw, K., & Luyckx, G. (2003). Shear stress distribution in partially filled pipes. *Journal of Hydraulic Engineering*, 129(9), 697-705.
- Bjorkquist, D. C. (2002). Stereoscopic PIV calibration verification. *Proceedings of the 11th international symposium on application of laser techniques to fluid mechanics*. Lisbon, Portugal, July 2002.
- Bonakdari, H., Larrarte, F., Lassabatere, L., & Joannis, C. (2008). Turbulent velocity profile in fully-developed open channel. *Environmental Fluid Mechanics* , 8(1), 1-17.
- Chiu, C.-L. (1989). Velocity distribution in open channel flows. *Journal of Hydraulic Engineering*, 115(5), 576-594.
- Chow, V. T. (1959). *Open-channel Hydraulics*. New York: McGraw-Hill.
- Clark, S. P., & Kehler, N. (2011). Turbulent flow characteristics in circular corrugated culverts at mild slopes. *Journal of Hydraulic Research*, 49(5), 676-684.
- Coles, D. (1956). The law of the wake in the turbulent boundary layer. *Journal of Fluid Mechanics*, 1(2), 191-226.

- CONTECH Engineered Solutions . (2014, 4 23). Retrieved from <http://www.conteches.com/>
- Ead, S. A., Rajaratnam, N., Katopodis, C., & Ade, F. (2000). Turbulent open-channel flow in circular corrugated culverts. *Journal of Hydraulic Engineering*, 126(10), 750-757.
- Ehrenfried, K. (2002). Processing calibration-grid images using the Hough transformation. *Measurement Science and Technology*, 13(7), 975–983.
- Escudier , M. P., & Nicoll , W. B. (1966). The entrainment function in turbulent boundary-layer and wall-jet calculations. *Journal of Fluid Mechanics*, 25(2), 337-366.
- Funamizu, N., Yamashita, S., & Takakuwa, T. (1991). A uniform flow formula for the partially full flow in a circular pipe. *Bulletin of Faculty of the Engineering Hokkaido University*, 155, 1-9.
- Gardner, A. (2006). *Fish passage through road culverts*. Department of Biological and Agricultural Engineering. (Master Thesis) North Carolina State University.
- Garner, M. E. (2011). *A model study of the hydraulics related to fish passage through embedded culverts*. Saskatoon, Saskatchewan: M.Sc. Thesis, University of Saskatchewan.
- Gauthier, V., & Riethmuller, M. L. (1988). Application of PIDV to complex flows: measurement of the third component. *VKI Lectures Series on Particle Image Displacement Velocimetry*. Brussels.
- Granger, R. A. (1995). *Fluid Mechanics*. Mineola, New York : Dover Publications.

- Grifoll, J., & Giralt, F. (2000). The near wall mixing length formulation revisited. *International Journal of Heat and Mass Transfer*, 43(19), 3743-3746.
- Guo, J. (2014). Modified log-wake-law for smooth rectangular open channel flow. *Journal of Hydraulic Research*, 52(1), 121-128.
- Guo, J., & Julien, P. Y. (2003). Modified log-wake law for turbulent flow in smooth pipes. *Journal of Hydraulic Research*, 41(5), 493-501.
- Guo, J., & Julien, P. Y. (2007). Buffer law and transitional roughness effect in turbulent open-channel flows. *IAHR 5th International Symposium on Environmental Hydraulics*. Tempe, Arizona.
- Guo, J., & Meroney, R. N. (2013). Theoretical solution for laminar flow in partially-filled Pipes. *Journal of Hydraulic Research*, 51(4), 408-416.
- Guo, J., Julien, P. Y., & Meroney, R. N. (2005). Modified log-wake law for zero-pressure-gradient turbulent boundary layers. *Journal of Hydraulic Research*, 43(4), 421-430.
- Hotchkiss, R. H., & Frei, C. M. (2007). *Design for fish passage at roadway-stream crossings: Synthesis report*. Federal Highway Administration.
- House, M. R., Pyles, M. R., & White, D. (2005). Velocity distribution in streambed simulation culverts used for fish passage. *Journal of American Water Resource Association*, 41(1), 209-217.
- Jacquot, P., & Rastogi, P. K. (1981). Influence of out-of-plane deformation and its elimination in white-light speckle photography. *Opt. Lasers Eng*, 2(1), 33-55.

- Katopodis, C. (1992). *Introduction to fishway design*. Central and Arctic Region, Department of Fisheries and Oceans. Winnipeg, Manitoba: Freshwater Institute.
- Katopodis, C., Robinson, P. R., & Sutherland, B. G. (1978). *A study of model and prototype culvert baffling for fish passage*. Dept. of Fisheries and Environment. Winnipeg, Canada: Western Reg., Fisheries and Marine Service.
- Keane, R. D., & Adrian, R. J. (1992). Theory of cross-correlation analysis of PIV images. *Applied Scientific Research*, 49(3), 191-215.
- Kehler, N. J. (2009). *Hydraulic characteristics of fully developed flow in circular culverts*. Winnipeg, Manitoba: M.Sc. Thesis, University of Manitoba.
- Kilgore, R. T., Bergendahl, B. S., & Hotchkiss, R. H. (2010). *Culvert design for aquatic organism passage Hydraulic Engineering Circular Number 26*. Federal Highway Administration.
- Kim, J., Moin, P., & Moser, R. (1987). Turbulence statistics in fully developed channel flow at low Reynolds number. *Journal of Fluid Mechanics*, 177, 133-166.
- Knight, D. W., & Sterling, M. (2000). Boundary shear in circular pipes running partially full. *Journal of Hydraulic Engineering*, 126(4), 263-275.
- Kraus, N. C., Lohrmann, A., & Cabrera, R. (1994). New acoustic meter for measuring 3D laboratory flows. *Journal of Hydraulic Engineering*, 120(3), 406-412.
- LabView. (2013, August 6). Retrieved April 25, 2014, from <http://www.ni.com/labview/>

- Magura, C. R. (2007a). Velocity structure in an embedded corrugated steel pipe model. *Challenges for Water Resources Engineering in a Changing World* (pp. 22-24). Winnipeg, Manitoba: 18th Canadian Hydrotechnical Conference.
- Magura, C. R. (2007b). *Hydraulic characteristics of embedded circular culverts*. Winnipeg, Manitoba: M.Sc. Thesis University of Manitoba.
- MatLab. (2014, March 6). Retrieved April 25, 2014, from <http://www.mathworks.com/>
- McEnroe, B. M., & Malone, T. R. (2008). *Hydraulic resistance of small-diameter hellically corrugated metal pipes*. Lawrence, KS: Kansas Department of Trasportation.
- Melling, A. (1997). Tracer particles and seeding for particle image. *Measurement Science and Technology*, 8(12), 1406-1416.
- Mohebbi, A., Zhai, Y., & Kerenyi, K. (2010). *Fish passage in large culverts with low flows*. McLean, VA: Federal Highway Administration.
- Moody, L. F. (1944). Friction factors for pipe flow. *Transactions of the ASME*, 66(8), 671-684.
- Morrison, R. R., Hotchkiss, R. H., Stone, M., Thurman, D., & Horner-Devine, A. R. (2009). Turbulence characteristics of flow in a spiral corrugated culvert fitted with baffles and implications for fish passage. *Ecological Engineering*, 35(3), 381-392.
- Nezu, I. (2005). Open-channel flow turbulence and Its research prospect in the 21st century. *Journal of Hydraulic Engineering*, 131(4), 229-246.



- Nezu, I., & Rodi, W. (1986). Open-channel flow measurements with a laser doppler anemometer. *Journal of Hydraulic Engineering* , 112(5), 335-355.
- Nikuradse, J. (1950). *Laws of flow in rough pipes*. Washington: NACA.
- Norman, J. M., Houghtalen, R. J., & Johnston, W. J. (2001). *Hydraulic design of highway culverts*. Federal Highway Administration.
- Pipingdesign*. (2014, April 25). Retrieved from Pipingdesign:  
<http://www.pipingdesign.nl/mbo%20piping/pagina3-1-2-1.htm>
- Prasad, A. K. (2000). Stereoscopic particle image velocimetry. *Experiments in Fluids* , 29(2), 103-116.
- Prasad, A. K., & Adrian, R. J. (1993). Stereoscopic particle image velocimetry applied to the liquid flows. *Experiments in Fluids* , 15(1), 49-60.
- Prasad, A. K., & Jenson, K. (1995). Scheimpflug stereocamera for particle image velocimetry in liquid flows. *Applied Optics*, 34(30), 7092-7099.
- Precht, E., Janssen, F., & Huettel, M. (2006). Nearbottom performance of the Acoustic Doppler Velocimeter (ADV) – a comparative study. *Aquatic Ecology*, 40(33), 481-492.
- Raffel, M., Willert, C., Wereley, S., & Kompenhans, J. (2007). *Particle Image Velocimetry; A Practical Guide (Experimental Fluid Mechanics)*. New York: Springer-Verlag.
- Replogle, J. A., & Chow, V. T. (1966). Tractive-force distribution in open channels. *Journal of Hydraulic Devison*, 92(2), 169-191.

- Reynolds, O. (1883). An Experimental Investigation of the Circumstances Which Determine Whether the Motion of Water Shall be Direct or Sinous, and of the Law of Resistance in Parallel Channels. *Proceedings of the Royal Society of London (1854-1905)*, 35, 84-99.
- Richmond, M. C., Deng, Z., Guensch, G. R., Tritico, H., & Pearson, W. H. (2007). Mean flow and turbulence characteristics of a full-scale spiral corrugated culvert with implications for fish passage. *Ecological Engineering*, 30(4), 333-340.
- Rowland, E. R., Hotchkiss, R. H., & Barber, M. E. (2002). *Modeling hydrology for design of fish passage*. Pullman, WA: Washington State Transportation Center (TRAC).
- Schall, J. D., Thompson, P. L., Zerges, S. M., & Kilgore, R. T. (2012). *Hydraulic Design of Highway Culverts Hydraulic Design Series Number 5*. Federal Highway Administration.
- Shiono, K., & Knight, D. W. (1991). Turbulent open-channel flows with variable depth across the channel. *Journal of Fluid Mechanics*, 222, 617-646.
- Sollof, S. M., Adrian, R. J., & Liu, Z.-C. (1997). Distortion compensation for generalized stereoscopic particle image velocimetry. *Measurement Science and Technology*, 8(12), 1441-1454.
- Sontek. (2001). SonTek ADVField Acoustic Doppler Velocimeter: technical documentation. San Diego, CA: SonTek/YSI, Inc.
- Steffler, P. M., Rajaratnam, N., & Peterson, A. W. (1985). LDA measurements in open channel. *Journal of Hydraulic Engineering*, 111(1), 119-130.

- Stein, O. R., & Tillinger, T. N. (1996). *Fish passage through culverts in Montana: A preliminary investigation*. Bozeman, Montana: Montana Department of the Transportation.
- Sterling, M., & Knight, D. W. (2000). Resistance and boundary shear in circular conduits with flat beds running part full. *Proc. Instn Civ. Engrs Water & Mar. Engng*, (pp. 229-240).
- Straub, L., & Morris, H. (1950a). *Hydraulic data comparison of concrete and corrugated metal culvert pipes*. Department of Civil Engineering. Minneapolis, Minnesota: University of Minnesota Centennial.
- Straub, L., & Morris, H. (1950b). *Hydraulic tests on corrugated metal culvert pipes*. Department of Civil Engineering. Minneapolis: University of Minnesota Centennial.
- Sutera, S. P., & Skalak, R. (1993). The history of Poiseuille's law. *Annual Review of Fluid Mechanics*, 25, 1-20.
- Tuncok, I. K., & Mays, L. W. (1999). Hydraulic Design of Culverts and Highway Structures. In L. W. Mays, *Hydraulic Design Handbook*. McGraw-Hill Professional.
- Willert, C. (1997). Stereoscopic digital particle image velocimetry for applications in wind tunnel flows. *Measurement Science and Technology*, 8(12), 1465-1479.
- Willert, C. (2006). Assessment of the camera models for use in planar velocimetry calibration. *Experiments in Fluids*, 41(1), 135-143.
- Yang, S., Tan, S., & Lim, S. (2004). Velocity distribution and dip-phenomenon in smooth uniform open channel flows. *Journal of Hydraulic Engineering*, 130(12), 1179-1186.

- Yoon, J.-I., Sung, J., & Lee, M. H. (2012). Velocity profiles and friction coefficients in circular open channels. *Journal of Hydraulic Research*, 50(3), 1-8.
- Young, D. F., Munson, B. R., Okiishi, T. H., & Huebsch, W. W. (2011). *A Brief Introduction To Fluid Mechanics* (5th ed.). New York: John Wiley & Sons, Inc.
- Zang, W., & Prasad, A. K. (1997). Performance evaluation of a Scheimpflug stereocamera for particle image velocimetry. *Appl Opt*, 36(33), 8738-8744.
- Zhai, Y. (2012). *CFD modeling of fish passage in large culverts and assistance for culvert design with fish passage*. Department of Civil Engineering. Lincoln, NE: University of Nebraska-Lincoln.

## APPENDIX A: DATA

Experimental data used for the model verification as well as the method for their acquisition are discussed in Appendix A.1 through A.4. Moreover, they are followed by test matrices which list some of their important hydraulic parameters namely the channel bed slope ( $S_0$ ), bed roughness height ( $h'$ ), flow depth ( $h$ ), cross-sectional average velocity ( $\bar{U}$ ), maximum cross-sectional velocity ( $U_{max}$ ), Froude number ( $Fr$ ), and Reynolds number ( $Re$ ). Froude and Reynolds numbers were calculated according to

$$Fr = \frac{\bar{U}}{\sqrt{g \frac{A_w}{b}}} \quad 100$$

and

$$Re = \frac{4\bar{U}R_h}{\nu} \quad 101$$

respectively. Herein,  $A_w$  and  $R_h$  are wetted area and hydraulic radius, accordingly.

### A.1 Mohebbi et al. (2010) Data

#### A.1.1 Experimental Method

Mohebbi et al. (2010) performed S-PIV and ADV tests on a 0.9144 m diameter CMP comprising different slopes, flow rates, flow depths, and roughness heights (Mohebbi, Zhai, & Kerényi, 2010). The purpose of ADV tests were just to validate the S-PIV data and, therefore, their discussion is out of the scope of this research (the reader is referred to (Zhai, 2012) for further information regarding ADV data plots and discussion). Table A.1 lists the important hydraulic characteristics of their tests. These data originally were used to calibrate the CFD model and were expected to

**Table A.1 Laboratory Test Matrix (Mohebbi, Zhai, & Kerenyi, 2010)**

Test	$S_o$ (-)	$h'$ (m)	$h$ (m)	$\bar{U}$ (m/s)	$U_{max}$ (m/s)	$Fr$ (-)	$Re$ (-)
1_1	0.00401	0.000	0.114	0.216	0.440	0.247	4.57E+04
1_2	0.00209	0.000	0.152	0.216	0.417	0.213	5.75E+04
1_3	0.00122	0.000	0.228	0.216	0.356	0.172	7.79E+04
1.4	0.01745	0.000	0.114	0.335	0.622	0.383	7.09E+04
1_5	0.00436	0.000	0.152	0.335	0.633	0.330	8.92E+04
1_6	0.00209	0.000	0.228	0.335	0.555	0.266	1.21E+05
2_1	0.00122	0.137	0.114	0.216	0.350	0.214	6.27E+04
2_2	0.00122	0.137	0.152	0.216	0.367	0.186	7.58E+04
2_3	0.00122	0.137	0.228	0.216	0.342	0.153	9.64E+04
2.4	0.00192	0.137	0.114	0.335	0.524	0.332	9.73E+04
2_5	0.00157	0.137	0.152	0.335	0.510	0.289	1.18E+05
2_6	0.00157	0.137	0.228	0.335	0.492	0.237	1.50E+05
3_1	0.00157	0.274	0.114	0.216	0.371	0.207	6.59E+04
3_2	0.00157	0.274	0.152	0.216	0.354	0.180	7.94E+04
3_3	0.00140	0.274	0.228	0.216	0.316	0.146	9.96E+04
3.4	0.00279	0.274	0.114	0.335	0.583	0.322	1.02E+05
3_5	0.00157	0.274	0.152	0.335	0.534	0.279	1.23E+05
3_6	0.00227	0.274	0.228	0.335	0.485	0.293	1.02E+05

be used to validate the analytical and empirical mathematical models. However, because of the flume wall effect on the velocity pattern, it was decided to use other alternatives. Nevertheless, they remain as benchmark data for future CFD model calibrations, roughness effect studies, and qualitative investigations of the flow pattern in CMPs. The flow condition was subcritical with

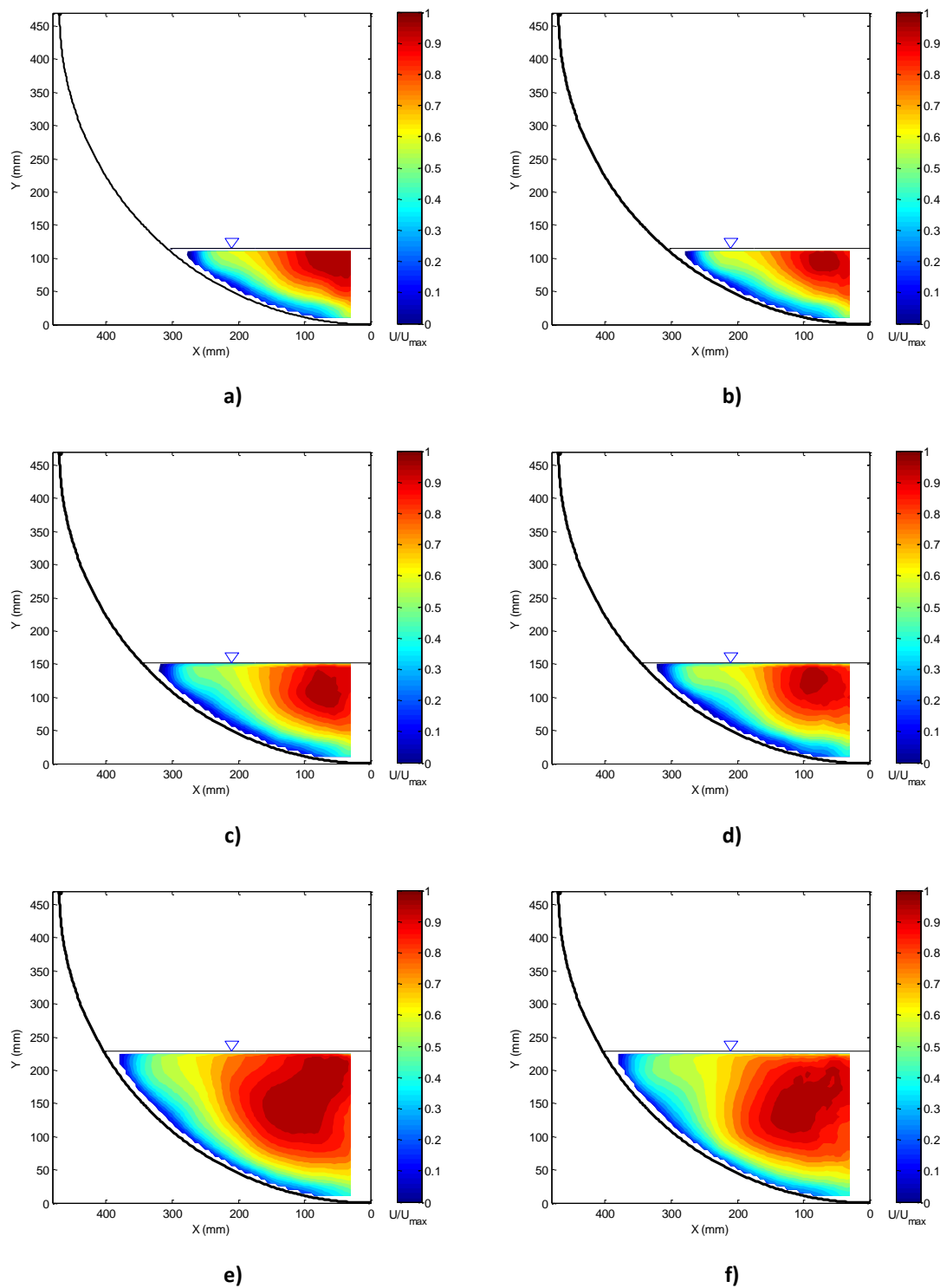


Figure A.1 Cross-sectional Velocity Distribution (Mohebbi, Zhai, & Kerenyi, 2010)

a) Test 1\_1 b) Test 1\_4 c) Test 1\_2 d) Test 1\_5 e) Test 1\_3 f) Test 1\_6

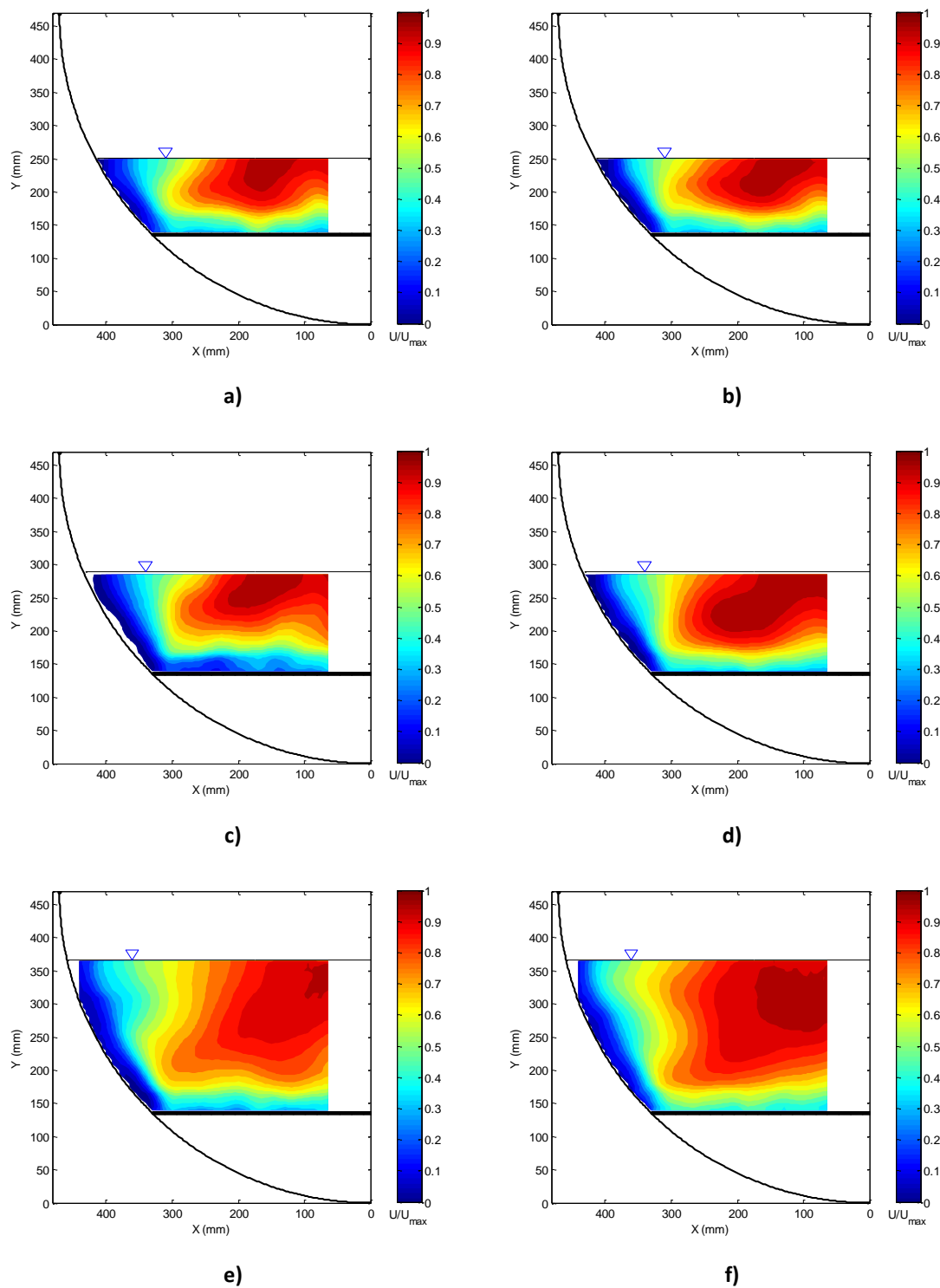


Figure A.2 Cross-sectional Velocity Distribution (Mohebbi, Zhai, & Kerenyi, 2010)

a) Test 2\_1 b) Test 2\_4 c) Test 2\_2 d) Test 2\_5 e) Test 2\_3 f) Test 2\_6



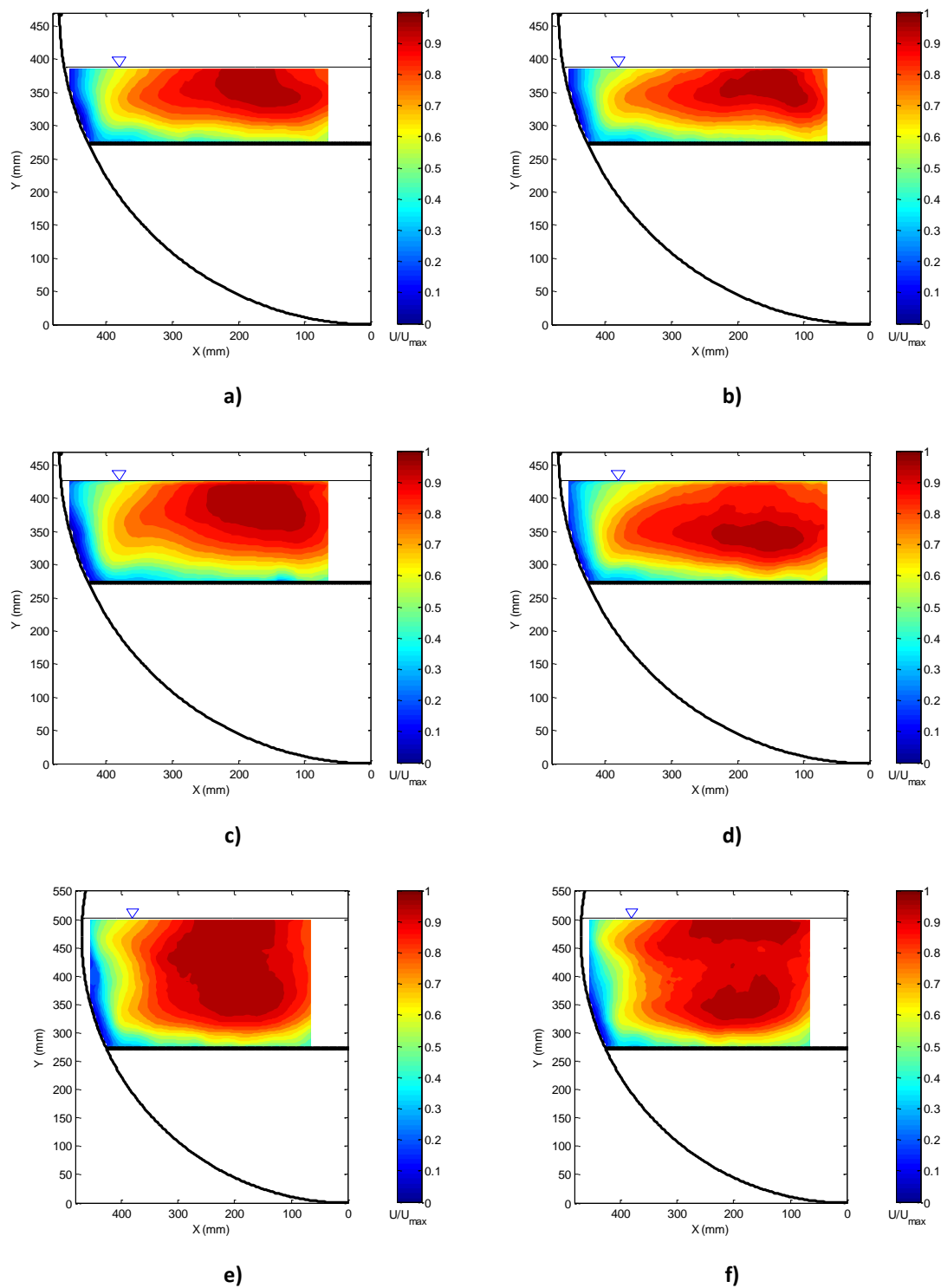


Figure A.3 Cross-sectional Velocity Distribution (Mohebbi, Zhai, & Kerenyi, 2010)

a) Test 3\_1 b) Test 3\_4 c) Test 3\_2 d) Test 3\_5 e) Test 3\_3 f) Test 3\_6

**Table A.2 Laboratory Test Matrix (Clark & Kehler, 2011)**

Test	$S_o$ (-)	$h'$ (m)	$h$ (m)	$\bar{U}$ (m/s)	$U_{max}$ (m/s)	$Fr$ (-)	$Re$ (-)
1	0.00028	0	0.49	0.265	0.362	0.13	2.38E+05
2	0.00110	0	0.35	0.402	0.550	0.25	2.95E+05
3	0.00110	0	0.52	0.506	0.643	0.24	4.68E+05
4	0.00270	0	0.27	0.557	0.760	0.40	3.39E+05
5	0.00270	0	0.40	0.693	0.861	0.32	5.57E+05

Froude number ranging from 0.146 to 0.383 and fully turbulent with Reynolds number ranging from 4.57E+04 to 1.50E+05 for all the experiments.

### A.1.2 Velocity Contour Plots

Figure A.1a-f, Figure A.2a-f, and Figure A.3 plot Mohebbi et al. (2010) data in terms of dimensionless velocity of  $u_z(x, y)/U_{max}$  according to the test matrix (Table A.1). The camera was not able to capture the area close to the pipe centerline (50 mm from right) because of the blockage from the flume supports. Therefore, those areas were left blank in the figures.

## A.2 Clark and Kehler (2011) Data

### A.2.1 Experimental Method

Clark and Kehler (2011) performed Acoustic Doppler Velocimetry (ADV) tests on a 0.8 m diameter CMP comprising different slopes, flow rates, flow depths, and no roughness on the bed (Clark & Kehler, 2011). Table A.2 lists the important hydraulic characteristics of their tests. They resolved the ADV near-bed shortcomings by using different types of ADV probes including face up, down, and side looking and later combined their data to have a whole flow velocity field. The flow

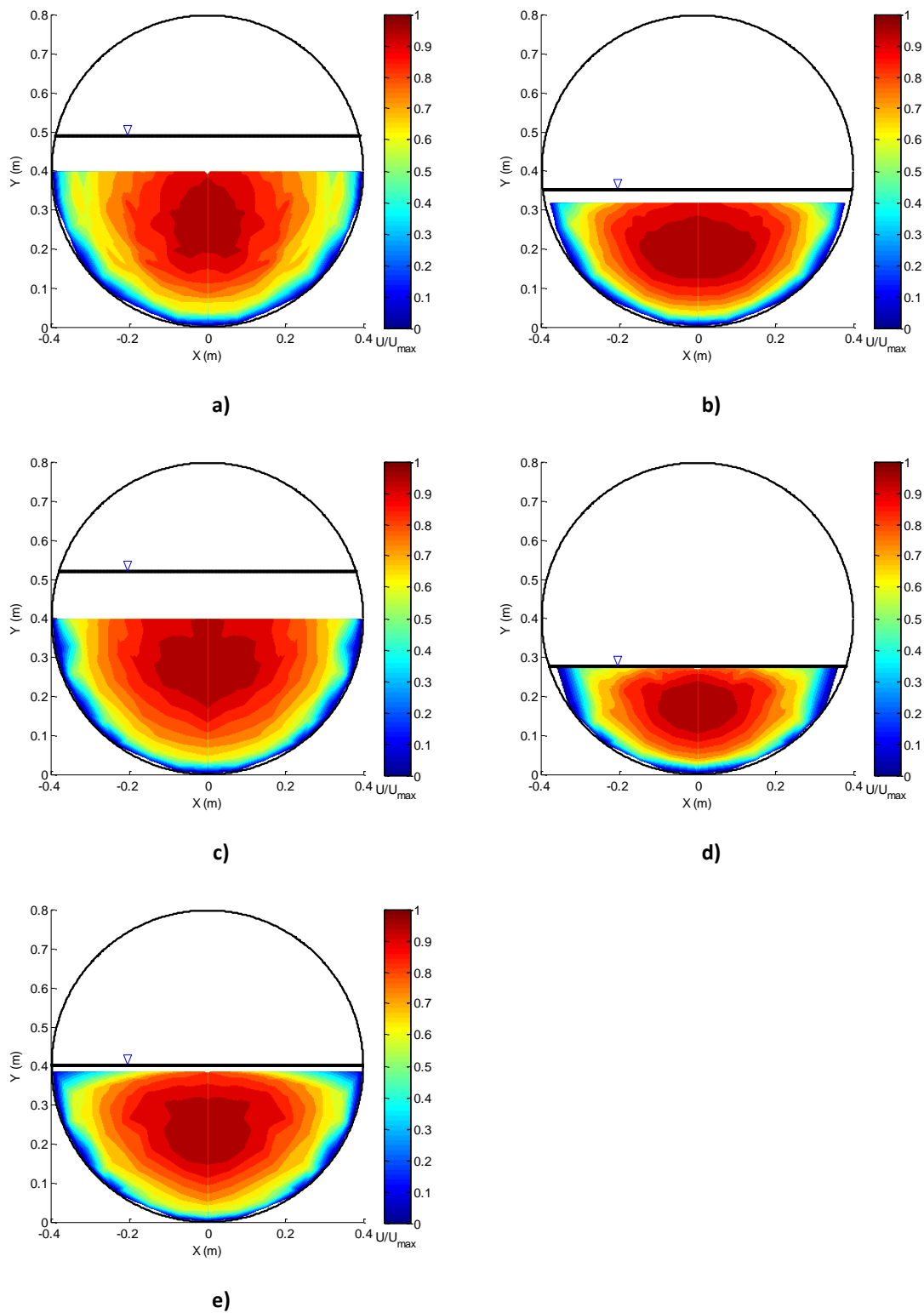


Figure A.4 Cross-sectional Velocity Distribution (Clark & Kehler, 2011)

a) Test 1 b) Test 2 c) Test 3 d) Test 4 e) Test 5

**Table A.3 Laboratory Test Matrix (Yoon, Sung, & Lee, 2012)**

Test	$S_o$ (-)	$h'$ (m)	$h$ (m)	$\bar{U}$ (m/s)	$U_{max}$ (m/s)	$Fr$ (-)	$Re$ (-)
1	0.00258	0	0.015	0.152	0.235	0.467	5.69E+03
2	0.00258	0	0.020	0.208	0.313	0.543	9.76E+03
3	0.00258	0	0.025	0.247	0.357	0.563	1.35E+04
4	0.00258	0	0.030	0.264	0.378	0.532	1.60E+04
5	0.00258	0	0.035	0.282	0.402	0.503	1.83E+04
6	0.00258	0	0.040	0.284	0.400	0.442	1.89E+04

condition was subcritical with Froude number ranging from 0.13 to 0.40 and fully turbulent with Reynolds number ranging from 2.38E+05 to 5.57E+05 for all the experiments.

### A.2.2 Velocity Contour Plots

Figure A.4a-e plot Clark and Kehler (2011) data in terms of dimensionless velocity of  $u_z(x, y)/U_{max}$  according to the test matrix (Table A.2). In some cases, they were not able to capture isovels close to the water surface due to the fluctuations at the free surface.

## A.3 Yoon et al. (2012) Data

### A.3.1 Experimental Method

Yoon et al. (2012) performed S-PIV tests on a 0.05 m diameter smooth plastic pipe with different slopes, flow rates, and flow depths (Yoon, Sung, & Lee, 2012). Table A.3 lists the important hydraulic characteristics of their tests. The flow condition was subcritical with Froude number ranging from 0.442 to 0.563 and transient to fully turbulent with Reynolds number ranging from 5.69E+03 to 1.89E+04 for all the experiments (Table A.3). Yoon et al. (2012) data were found to

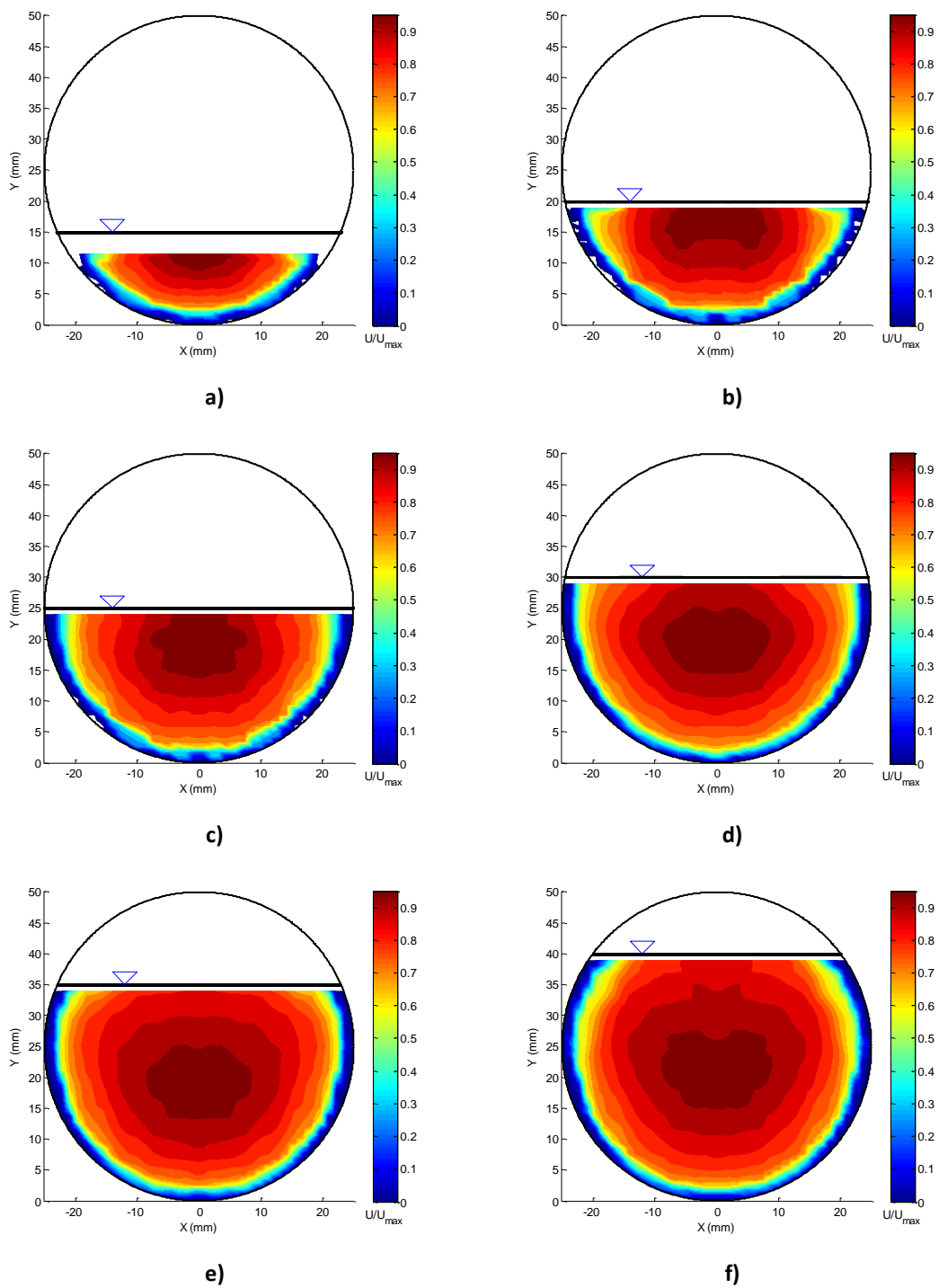


Figure A.5 Cross-sectional Velocity Distribution (Yoon, Sung, & Lee, 2012)

a) Test 1 b) Test 2 c) Test 3 d) Test 4 e) Test 5 f) Test 6

be the most comprehensive data for a smooth P-FPF with filling ratios ranging from 30% to 80%. However, the low Reynolds number in the first two experiments suggests that these data cannot be treated as a fully turbulent flow. Further, since the test pipe is small in diameter (only 50 mm), the data may not be a good representative of a real-world culvert of at least a foot of length.

Figure A.5a-f plot Yoon et al. (2012) data in terms of dimensionless velocity of  $u_z(x, y)/U_{max}$  according to the test matrix (Table A.3). Except the first test that they were not able to measure the free surface velocity due to the laser illuminations and low flow depth, the rest of the data were in a good shape.

## A.4 Knight and Sterling (2000) Data

### A.4.1 Experimental Method

Knight and Sterling (2000) and Sterling and Knight (2000) performed velocimetry tests with the aid of a pitot-static tube connected to an air-water manometer on a 0.244 m diameter smooth clear acrylic pipe comprising of different slopes, flow rates, flow depths, and roughness heights (Knight & Sterling, 2000; Sterling & Knight, 2000). Table A.4 lists the important hydraulic characteristics of their tests. The flow condition was both subcritical and supercritical with Froude number ranging from 0.375 to 1.960 and fully turbulent with Reynolds number ranging from  $4.06E+04$  to  $134.2E+04$  for all the experiments (Table A.4).

### A.4.1 Velocity Contour Plots

Figure A.6a-c plot Knight and Sterling (2000) data in terms of dimensionless velocity of  $u_z(x, y)/U_{max}$  according to the test matrix (Table A.4). The data were acquired through

**Table A.4 Laboratory Test Matrix (Knight & Sterling, 2000; Sterling & Knight, 2000)**

Test	$S_o$ (-)	$h'$ (m)	$h$ (m)	$\bar{U}$ (m/s)	$U_{max}$ (m/s)	$Fr$ (-)	$Re$ (-)
1_1	0.00100	0.000	0.0813	0.394	-	0.516	6.49E+04
1_2	0.00100	0.000	0.1235	0.493	0.669	0.505	11.0E+04
1_3	0.00100	0.000	0.1626	0.524	-	0.441	13.5E+04
1_4	0.00100	0.000	0.2015	0.554	-	0.375	15.0E+04
2_1	0.00196	0.061	0.0203	0.294	-	0.671	1.91E+04
2_2	0.00196	0.061	0.0361	0.403	-	0.696	4.23E+04
2_3	0.00196	0.061	0.0608	0.565	0.677	0.748	8.75E+04
2_4	0.00196	0.061	0.1015	0.688	0.884	0.680	14.5E+04
2_5	0.00196	0.061	0.1232	0.769	-	0.663	18.5E+04
2_6	0.00196	0.061	0.1330	0.775	-	0.626	18.9E+04
2_7	0.00862	0.061	0.0203	0.750	-	1.710	4.90E+04
2_8	0.00862	0.061	0.0608	1.283	-	1.700	19.9E+04
2_9	0.00862	0.061	0.1015	1.625	-	1.590	34.2E+04
3_1	0.00200	0.081	0.0407	0.449	-	0.718	5.50E+04
3_2	0.00200	0.081	0.0815	0.625	-	0.685	11.4E+04
3_3	0.00200	0.081	0.1020	0.707	-	0.670	15.1E+04
3_4	0.00200	0.081	0.1142	0.833	-	0.721	18.4E+04
3_5	0.00900	0.081	0.0407	1.229	-	1.960	15.0E+04
4_1	0.00900	0.122	0.0395	0.886	-	1.400	9.41E+04
4_2	0.00900	0.122	0.0600	1.143	-	1.420	15.7E+04
4_3	0.00900	0.122	0.0722	1.214	-	1.330	18.2E+04
5_1	0.00880	0.162	0.0210	0.666	-	1.440	4.06E+04
5_2	0.00880	0.162	0.0332	0.691	-	1.150	5.86E+04

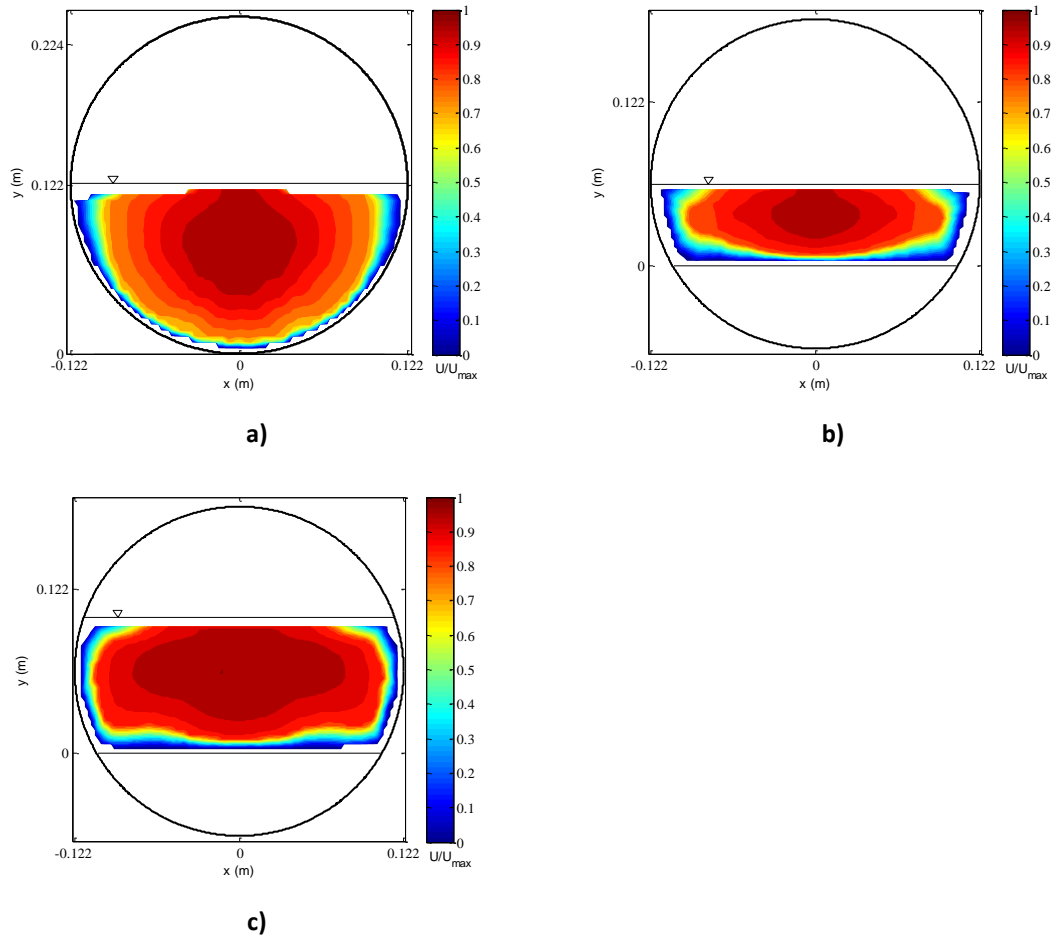


**Figure A.6 Cross-sectional Velocity Distribution (Knight & Sterling, 2000; Sterling & Knight, 2000)**

**a) Test 1\_2 b) Test 2\_3 c) Test 2\_4**

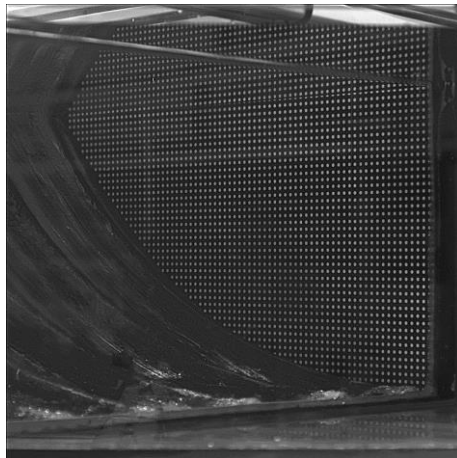
digitization of the plotted cross-sectional velocity distribution (test 1\_2, test 2\_3 and test 2\_4) and as a result, they have a lower resolution compared to the recent data. Nevertheless, being the only dataset with roughness being present on the bed, they play a major role in the empirical model validation.



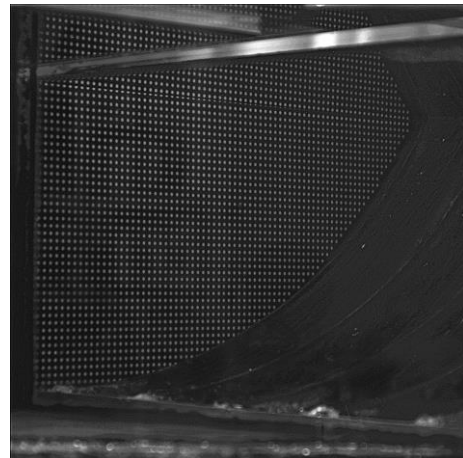
## APPENDIX B: S-PIV IMAGES

### B.1 Camera Calibration Images

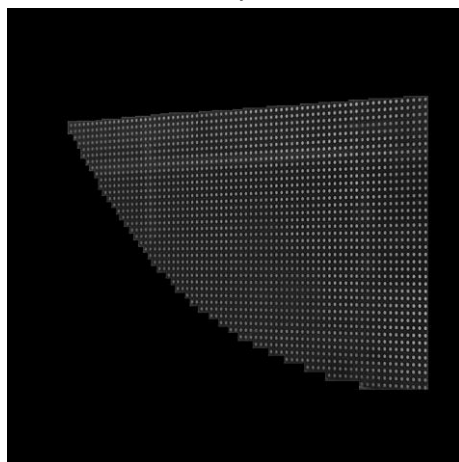
Figure B.7 depicts the images taken and processed in the camera calibration procedure. Figure B.7a is the image taken with the CCD camera without any change. Figure B.7b is the same image after masking everything except the calibration grid. This process is time consuming and should be done manually. Figure B.7c is the output of the image processing software and by the end of this step the dots on the calibration grid are defined digitally. Figure B.7d is the final



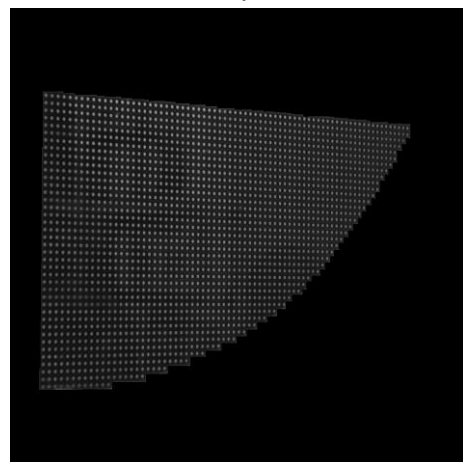
a)



e)



b)



f)

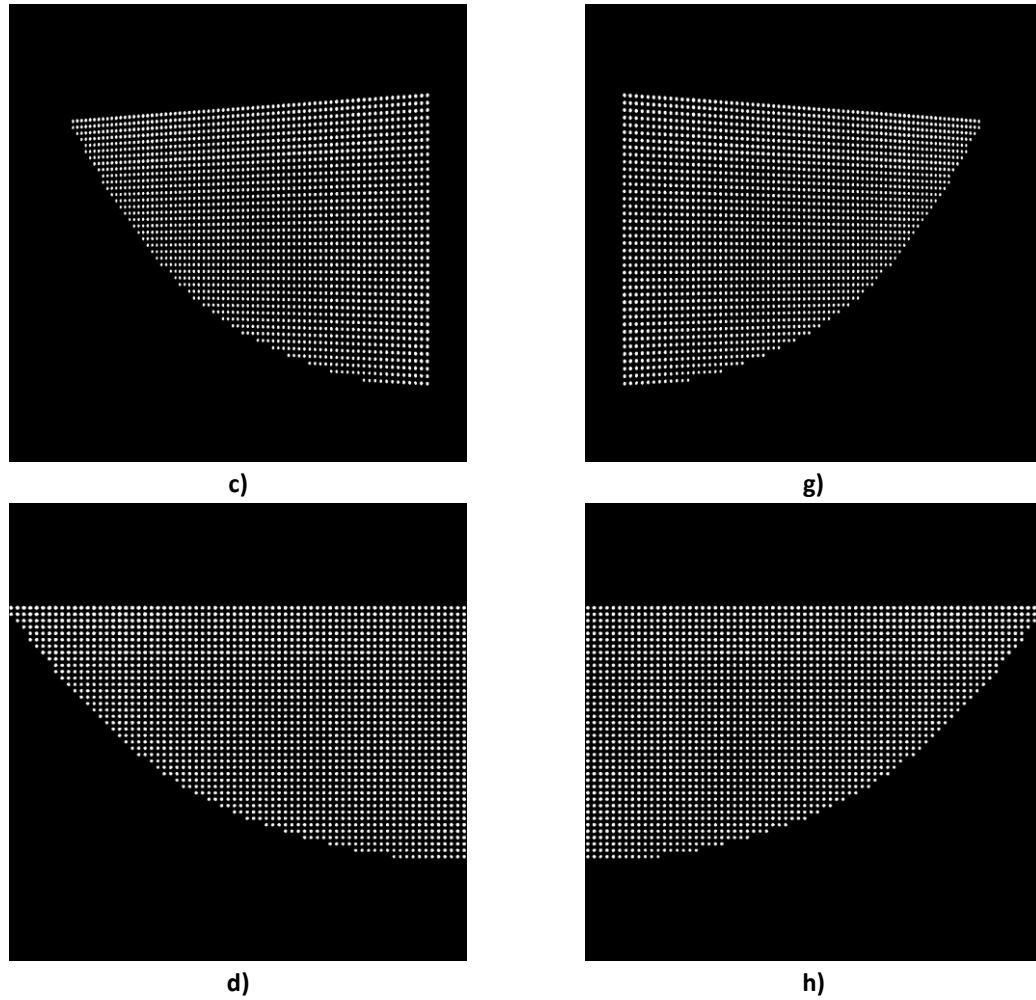


**Figure B.7 Camera Calibration Images**

**Camera Calibration Left View Image a) Normal b) Masked c) Processed d) Dewarped**

**Camera Calibration Right View Image e) Normal f) Masked g) Processed h) Dewarped**

dewarped image used in all the calculations. Figure B.7e-h are the counterparts of the Figure B.7a-d captured from the right camera.